Fall 2017

Diffusion Modeling of Impurities Through the Molybdenum Back Contact of CIGS Solar Cells

Chinedum John Akwari
Old Dominion University

DIFFUSION MODELING OF IMPURITIES THROUGH THE MOLYBDENUM

BACK CONTACT OF CIGS SOLAR CELLS

by

Chinedum John Akwari
B.S. May 2016, Old Dominion University

A Thesis Submitted to the Faculty of
Old Dominion University in Partial Fulfillment of the
Requirements for the Degree of

MASTER OF SCIENCE

ELECTRICAL AND COMPUTER ENGINEERING

OLD DOMINION UNIVERSITY
December 2017

Approved by:

Sylvain Marsillac (Director)

Orlando Ayala (Member)

Chung Hao Chen (Member)

ABSTRACT

DIFFUSION MODELING OF IMPURITIES THROUGH THE MOLYBDENUM BACK
CONTACT OF CIGS SOLAR CELLS

Chinedum John Akwari
Old Dominion University, 2017
Director: Dr. Sylvain Marsillac

CIGS is a major technology in photovoltaics and depends heavily, as any other PV technology, on the capacity to achieve the highest efficiency possible to compete on the market. Alkaline elements, notably sodium and potassium, play a key role in this matter as they enhance the open circuit voltage and the fill factor of the CIGS solar cells. However, this effect exists only for very specific concentration of sodium and potassium. These impurities typically diffuse through the soda-lime glass substrate.

Via modeling of the SIMS data, we try to understand and predict the diffusion mechanisms of these impurities from the glass through the molybdenum into the CIGS absorber layer. We therefore try to understand the appropriate modeling parameters that could include: grains and grain boundaries size and geometry, diffusivity in the grain and the GBs, variation of these parameters as a function of deposition process parameters such as power, pressure, Tss, and post-deposition temperature treatment. Mathematical modeling is done using MS Excel and COMSOL Multiphysics.

ACKNOWLEDGMENTS

I would like to thank my research advisor, Dr. Sylvain Marsillac, for his support and guidance during my research work and entire graduate study. Thank you for being a great advisor; I have a learned and grown a lot both as a student and as a person during my time as a graduate student.

I would like to thank Dr. Orlando Ayala and Dr. Chung Hao Chen for serving on my thesis committee. A special thanks to Dr. Ayala for the time we spent exploring and working through COMSOL. I gained a lot of knowledge and problem-solving skills during our meetings.

A special thanks to all my research group member's Grace Rajan, Shankar Karki and Ben Belfore for the assistance and encouragement they have offered me throughout my thesis work.

TABLE OF CONTENTS

LIST OF FIGURES

LIST OF TABLES

Table   Page

CHAPTER 1

1. INTRODUCTION

1.1 BACKGROUND

Power consumption around the world has been steadily increasing each year; in 2010, the average power consumed around the world was about 17.5 TW (1 TW = 10^{12} W)[1] . Most of this consumed power is generated through the combustion of fossil fuels. It is widely known and accepted that the combustion of fossil fuels is harmful to the environment and the global climate in general because release of CO_2 has adversely changed the composition of the atmosphere[2]. There is also the anticipated problem that these fuels could run out sooner rather than later given the present rate of consumption. Thus, it is imperative that we utilize and further develop other energy sources - preferably clean and renewable ones and none are cleaner or more renewable than solar energy.

The estimated amount of energy that can be harnessed from other renewable energy sources such as biomass, geothermal, wind and hydroelectric is said to be less than 10 TW[2]. Solar energy is by far the most abundant renewable energy source available to us, providing about 86,000 TW of energy[1], but we can only harvest a small portion of this solar power. It had been estimated that only about 600 TW of solar energy can be harnessed[2], but recent estimates show that it is possible to obtain between 400 and 8800 TW of energy depending on certain limitations such as topography, system design and land use[1]. Solar energy can be harnessed in different ways: converting sunlight into electricity using photovoltaic cells, converting sunlight into thermal energy (solar thermal energy), and converting sunlight into chemicals (solar fuels) [2]. Photovoltaic cells are perhaps the most common and well-known method of harvesting solar energy. These devices have long been fabricated using silicon and have dominated the market, but

cost of production is still too high[3]. Currently, thin film solar cells composed of CdTe or Cu(In,Ga)Se$_2$ are being increasingly fabricated and researched due to their lower cost of production and relatively high conversion efficiencies.

1.2 SOLAR CELL BACKGROUND

A solar cell is an electronic device that directly converts sunlight into electricity by photovoltaic effect, which involves generating current and voltage. The basic steps common to all solar cells involve: a) absorption of incident photon with an energy equal to or greater than the band gap to create electron-hole pairs (an electron in the valence band is excited into the conduction band, thus leaving behind a 'hole' in the valence band), (b) separation of the electron-hole pairs into carriers (electrons and holes) and (c) the collection of the light generated carriers to generate current.

As stated above, an electron-hole pair will be created if the energy of the incident photon is enough to overcome the band gap of the semiconductor materials used in fabricating the cell. However, the electron and hole can only exist separately for a short amount of time known as the carrier lifetime before they recombine. Thus, to prevent this recombination, which would result in no current/power generation, the electron-hole pairs are separated by the electric field that exists at the p-n junction and subsequently collected at the electrodes of an external circuit connected to the solar cell.

A solar cell can be modeled as a current source in parallel with a diode; the cell behaves like a diode when there is no light incident on it, but as the intensity of the light increases, the cell starts to generate current. The J-V (current density versus voltage) curve of a solar cell involves the superposition of the J-V curve of the solar cell in the dark with the light generated current. The diode equation under illumination is given as follows:

$$J = J_0 \left(e^{\frac{qV}{AkT}} - 1 \right) - J_{ph}$$

where J is the current density, J_0 is the saturation current density of the diode, V is the applied

voltage, J_{ph} is the light generated current density, q is the elementary charge (1.6x10^-

19 Coulombs), k is the Boltzmann constant (1.38x10^-23 J/K), T is the temperature in Kelvin

and A is the ideality factor.
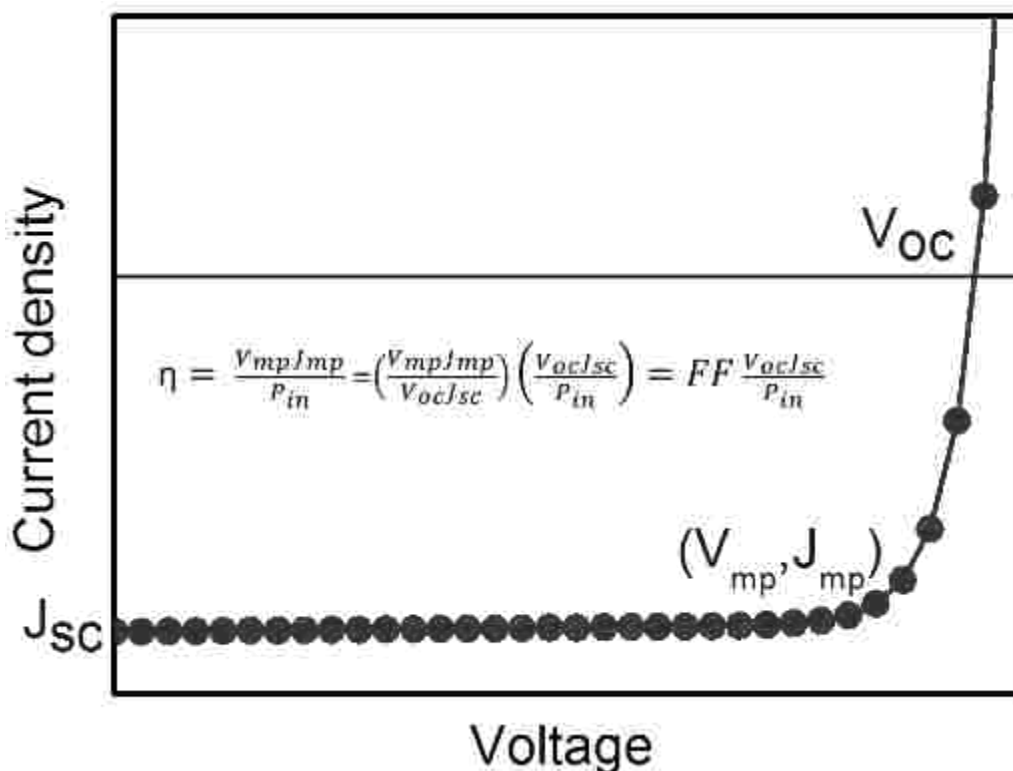
Figure 1.1 J-V characteristics of a solar cell under illumination.

The incident light shifts the J-V curve of the cell in the dark (diode J-V curve) into the fourth

quadrant where power can then be extracted from the diode (Figure 1.1). The main solar cell

performance parameters can be extracted from the J-V curve shown in Figure 1.1. These

parameters include: open-circuit voltage (V_{oc}), short-circuit current density (J_{sc}), fill factor (FF),

the maximum power (P_{max}) and the current density and voltage at P_{max}, which are J_{mp} and V_{mp} respectively.

1.2.1. Open-circuit Voltage

The open-circuit voltage, V_{oc}, is the maximum voltage that can be obtained from the cell that occurs when no current flows through it. The open-circuit voltage relates to the amount of forward bias applied to the cell at which the dark current compensates for the light-generated current produced by the cell. The V_{oc} can be calculated with the following equation, which assumes a zero net current:

$$V_{OC} = \frac{AkT}{q} \ln\left(\frac{J_{ph}}{J_o} + 1\right)$$

where J_0 is the saturation current density, J_{ph} is the light generated current density, q is the elementary charge, k is the Boltzmann constant, T is the temperature in Kelvin and A is the ideality factor.

1.2.2. Short-circuit Current Density

The short-circuit current density, J_{SC}, is the maximum current density generated by the cell at zero voltage. The J_{SC} is the largest current that can be drawn from the cell and it depends on several factors such as: the area of the solar cell, the number of photons incident on the cell, the spectrum of the incident light (the spectrum is almost always standardized to the AM1.5G spectrum), the absorption and reflection coefficients of each layer of the cell and ultimately, the amount of light-generated carriers that can be collected which depends primarily on the minority carrier lifetime and surface passivation. Assuming a perfectly passivated surface and uniform generation, the J_{SC} can be approximated using the following equation:

$$J_{SC} = qG(L_N + L_P)$$

where G is the generation rate, L_P is the hole diffusion length and L_N is the electron diffusion length. The diffusion length is the average length a carrier moves between generation and recombination.

1.2.3. Fill Factor

The fill factor, FF, is the ratio of the maximum power produced by the solar cell to the product of V_{OC} and J_{SC}.

$$FF = \frac{J_{mp}V_{mp}}{J_{sc}V_{oc}}$$

The fill factor, graphically, is the area of the largest rectangle that will fit in the JV curve. In practice, the fill factor is always less than unity because it is affected by parasitic resistive losses.

1.2.4. Power Conversion Efficiency

The solar cell efficiency, η, is the parameter most commonly used to compare the performance of one solar cell to another. It is defined as the ratio of output energy from the solar cell to the input energy from the sun. The input power for efficiency calculations is 1 kW/m^2 or 100 mW/cm^2. The efficiency of a cell is given by the following equation:

$$\eta = \frac{P_{max}}{P_{in}} = \frac{J_{mp}V_{mp}}{P_{in}} = \frac{V_{oc}J_{sc}\,FF}{P_{in}}$$

Solar cell efficiency depends on the temperature of the cell in addition to the spectrum and intensity of the incident light; thus,, when comparing one cell to another, extra caution must be taken to ensure that all conditions are controlled and kept uniform.

As mentioned earlier, the AM1.5G (Air Mass 1.5 and G stands for global where both direct and indirect illumination are taken into consideration) is the most popular standard used to

measure and compare the performance of photovoltaic cells in regard to the spectrum of the incident light. Air mass is defined as the path length which light takes through the atmosphere when the sun is directly overhead. It describes the reduction in the intensity of the light due to absorption by dust and air as it passes through the atmosphere. The Air Mass is defined using the following equation:

$$AM = \frac{1}{Cos\theta}$$

where θ is the angle of the path sunlight travels with respect to the vertical.

The standard spectrum outside of the Earth's atmosphere is known as the AM0 because the incident sunlight does not pass through the atmosphere at any point. The AM0 is used to predict the performance of solar cells used in outer space applications.

1.3   OVERVIEW OF PROGRESS IN PHOTOVOLTAIC (PV) TECHNOLOGY

In 1839, Edmund Becquerel discovered the photovoltaic effect when he observed that the action of light on a silver coated platinum electrode immersed in electrolyte produced an electric current. In 1873, Willoughby Smith discovered the photoconductivity of selenium. Four years later, in 1877, William Adams and Richard Day discovered that selenium produces electricity when exposed to light, but the photovoltaic cell produced using selenium was unable to convert solar power into electricity. In 1888, Charles Frits fabricated the first large area solar cell using a selenium layer in between gold and another metal with the device efficiency being less than 1% [4]. In 1954, Gerald Pearson, Calvin Fuller and Daryl Chapin developed the first modern silicon solar cell at Bell Laboratories with an efficiency of about 6%, capable of converting sunlight into electricity to run some everyday electrical equipment. Since then, many attempts have been made to find low cost, high-efficiency cells and this has led to several milestones. In 1980, the first thin-

film cell using copper sulfide/cadmium sulfide was developed at the University of Delaware with an efficiency of over 10%. In 1994, The National Renewable Energy Laboratory (NREL) developed a solar cell made from gallium indium phosphide and gallium arsenide which became the first solar cell to exceed 30% conversion efficiency [4].

Research for feasible solar cell materials has gone beyond the inorganic area. Organic polymers have attracted significant interest, despite their low conversion efficiency (Figure 1.2).
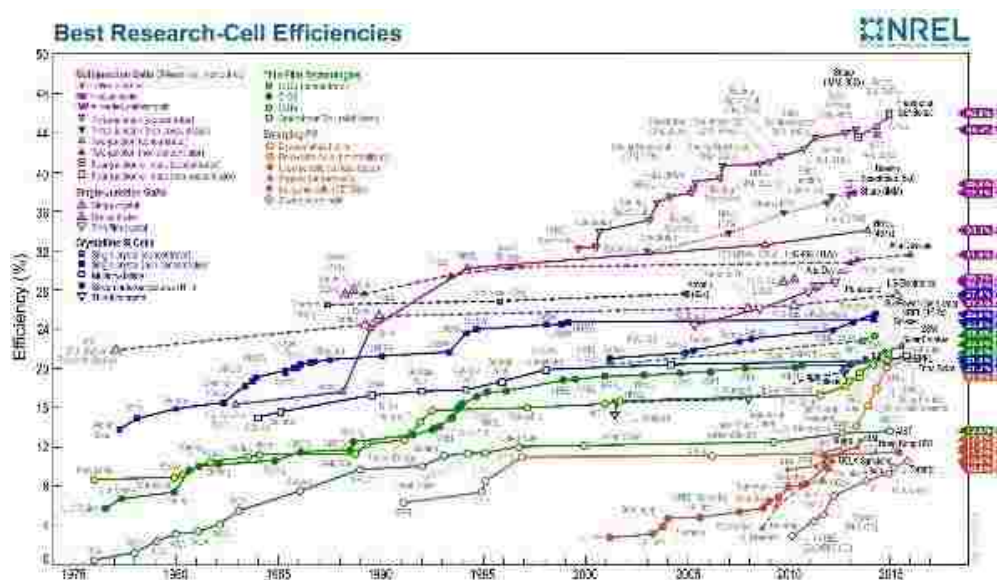
Figure 1.1 Maximum solar cells efficiency as a function of years [www.nrel.gov]

1.4 CIGS SOLAR CELL BASICS

1.4.1. Introduction

Cu(In,Ga)Se$_2$ solar cells are efficient, low-cost thin film solar cells ideal for cost-effective power generation. They are very stable and have displayed very high efficiencies at both the cell and module levels. They are also very suitable for space applications because they can be made flexible and lightweight and they have demonstrated resistance to high radiation.

The basic configuration of the solar cell includes a soda lime glass substrate, a sputtered Molybdenum (Mo) layer as the back contact, the pn junction is formed by depositing a p-type CIGS layer (typically by co-evaporation) and an n-type Cadmium Sulfide (CdS) layer by chemical bath deposition. The penultimate layer is formed by depositing a high resistance Zinc oxide (ZnO) layer and a doped highly conductive ZnO layer by radio frequency (RF) sputtering or chemical vapor deposition. Finally, nickel/aluminum can be deposited using electron-beam evaporation to serve as the front contacts.

1.4.2. CIGS Crystal Structure and Composition

CIGS is formed by alloying $CuInSe_2$ with $CuGaSe_2$, which have the chalcopyrite lattice structure. The chalcopyrite crystal structure is a diamond-like structure very similar to the zincblende crystal structure but with an ordered substitution of group I (copper) and group III (In or Ga) elements on the group II (Zn) sites of zincblende which results in the tetragonal unit cell (Figure 1.3) with c/a close to 2. Deviation from the c/a value being close to 2 can occur due to the different strengths of the Cu-Se, In-Se and Ga-Se bonds.
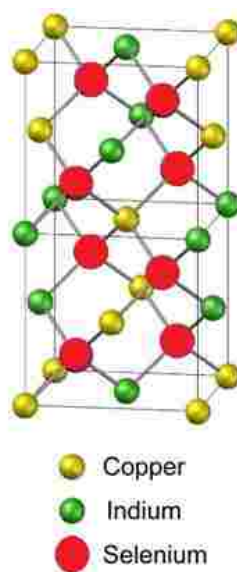
Figure 1.2 CIGS material crystal structure

1.4.3. CIGS Solar Cell Structure

a) Substrate

Soda lime glass is the most common substrate material used in fabricating CIGS solar cells, which is partly why these cells are very cost effective. The highest efficiency cells have typically been fabricated at a very high substrate temperature, T_{SS}, of 550°C, which the soda lime glass can withstand. Soda lime glass provides a good thermal expansion match for CIGS. It also contains some alkali impurities such as sodium that diffuse into the Mo and CIGS films during processing and have been shown to have beneficial effects on the efficiency of the cell. However, this glass may also contain some defects, which would make it less suitable for module application.

Other materials such as plastic foils or metals that are more lightweight and flexible than glass can also serve as substrates for CIGS fabrication.

b) Back Contact

Molybdenum (Mo) is typically used as the back contact of high efficiency cells. Molybdenum back contacts were deposited on soda lime glass (SLG) by DC magnetron sputtering with base pressure of ~ 2 x 10^{-6} Torr. 2 inch diameter Molybdenum targets, ¼ inch thickness, and 99.95% purity were used. Uniform film thickness (±5% error) was achieved using a rotatable substrate holder. The argon pressure was varied between 3 and 16 mTorr while keeping a constant sputtering power of 150 W. Sputter pressure affects the quality of the Mo film obtained because the pressure directly affects the adhesion of the Mo film on the glass substrate. During CIGS deposition, an intermediate layer of $MoSe_2$ is formed.

c) $Cu(InGa)Se_2$

The CIGS layer is typically deposited between 450 and 600°C by thermal co-evaporation from elemental sources (copper, indium, gallium and selenium). Depending on the number of

growth stages (actual elemental deposition), the co-evaporation process can be divided into a single stage process, two-stage process and three-stage process.

The single stage process involves one evaporation rate for each element and it is Cu deficient for its entirety. The two-stage process involves a Cu-rich growth in the first stage and a Cu-poor growth in the second and final stage of the deposition. Finally, the three-stage process involves indium and gallium deposition in the first stage, Cu deposition in the second stage and indium and Ga deposition in the third stage [5]. A constant Se flux is supplied during the entire co-evaporation process.

Other deposition methods include sequential selenization/sulfurization of precursor metal films and particle deposition by printing suitable inks on a substrate and then annealing [5].

d) CdS Buffer Layer

The cadmium sulfide (CdS) layer is grown using chemical bath deposition (CBD) and involves an alkaline solution containing the following: a cadmium salt such as $CdSO_4$, CdI_2, $CdCl_2$, a complexing agent, typically ammonia (NH_3) and a sulfur precursor, commonly thiourea ($SC(NH_2)_2$). The CIGS film is immersed in a bath containing the alkaline solution at a temperature of 60 to 80°C and in a few minutes, a thin CdS film precipitates from the solution and deposits onto the CIGS film.

e) Window layer

A highly transparent conducting oxide (TCO) layer is deposited onto the CdS layer and it is known as the window layer because it transmits the incident light to the CIGS absorber layer. A bilayer of Zinc oxide (ZnO) is typically used as the window layer. This bilayer consists of thin (50 nm) intrinsic ZnO layer and a thick (300 nm) n-type doped (Aluminum doped) ZnO layer. The intrinsic ZnO layer prevents the diffusion of aluminum from the Al-doped layer into the absorber

layer. The Al-doped ZnO layer provides much lower resistivity than the intrinsic ZnO layer, thus creating a very conductive and transparent layer. The TCO layer is usually deposited by RF magnetron sputtering.

f) Metal contacts

Metal grids are finally deposited onto the TCO layer to enable collection of current. The sandwich of Nickel/Aluminum/Nickel serve as the front metal contacts and they deposited by electron-beam evaporation. The two thin nickel layers protect the aluminum layer from reacting with oxygen from the TCO layer and from air in the ambient.

1.5   THESIS OBJECTIVES AND ORGANIZATION

The main objective of this work is to study the diffusion of sodium and potassium ions through the molybdenum layer. Using the work done in this thesis, the diffusion of other ions through any layer in the solar cell can subsequently be studied and understood.

In Chapter 2, the material properties of molybdenum films are discussed. The characterization techniques used to examine the molybdenum films are also studied and discussed.

In Chapter 3, the effects of sodium and potassium on device performance are discussed. Sodium and potassium diffusion models are then created in Microsoft Excel using the error and exponential function.

In Chapter 4, the COMSOL software is introduced. It is then used to create a better and more thorough diffusion model.

Finally, Chapter 5 provides a summary of the work presented in this thesis and a discussion of the future work.

CHAPTER 2

2 CU(IN,GA)SE₂ SOLAR CELL: BACK CONTACT MATERIAL PROPERTIES AND CHARACTERIZATION METHODS

2.1 MOLYBDENUM MATERIAL PROPERTIES

Molybdenum is the most common back contact material used for CIGS solar cells. The requirements for a good back contact material include inertness during the CIGS deposition process, ability to form an ohmic contact at the CIGS/back contact interface or low contact resistance with the CIGS layer, high conductivity and a comparable thermal expansion coefficient with the contact layers. Substantial research has been done on Ti, W, Ta, Nb, Mn, V, Mo and Cr to identify other possible contact materials, but molybdenum, with its relative stability at the CIGS processing temperature and low contact resistance to CIS, resistance to alloying with Cu and In, is the most outstanding choice for back contact material.

The molybdenum back contact is usually deposited by DC magnetron sputtering. It has been investigated and shown that there is a very high correlation between the deposition argon pressure and the conductivity and adherence of molybdenum films. Mo films sputtered under high argon pressure are under tensile stress; thus, they adhere well to the glass substrate, but this comes with the disadvantage of high resistivity, while those sputtered at low argon pressure are under compressive stress. Thus, they have low resistivity but adhere poorly to the substrate (delaminate). The trade-off between obtaining low resistivity while preventing the delamination of the Mo film comes from the development of a bi-layer Mo film. A thin layer is first sputtered at high argon pressure onto the glass, then followed by a thicker layer deposited at low argon pressure. The first layer provides good adhesion to the substrate while the second layer maintains good electrical

properties. This bi-layer concept is widely used in the fabrication of high efficiency CIGS solar cells.

2.2 CHARACTERIZATION METHODS

2.2.1 SECONDARY ION MASS SPECTROSCOPY (SIMS)

SIMS is a surface analysis technique method used to obtain the elemental depth profile and surface composition of thin films or solid surfaces. SIMS is a 'destructive' technique because it sputters the surface of the sample using a focused primary ion beam, such as Ar or Cs ions. The ions ejected from the sample are known as secondary ions and are then characterized by a mass/charge analyzer using their atomic mass values (Figure 2.1). The polarity of the sample determines whether positive or negative secondary ions will be extracted.

SIMS technique provides high lateral resolution (down to 40 nm) and very high sensitivity, enough to measure atoms in the ppm or even ppb range. It can also be used to analyze monolayers. The two main variations of the SIMS analysis based on the mode of operation are: Static and Dynamic SIMS. Static SIMS is used for elemental analysis of sub-monolayers using a pulsed ion beam and a time of flight mass spectrometer, while the dynamic SIMS is used to obtain the elemental depth profile of a sample using a DC primary ion beam and a quadruple or magnetic sector mass spectrometer. Dynamic SIMS analysis was used in this work to obtain the impurity profile of the molybdenum layer.
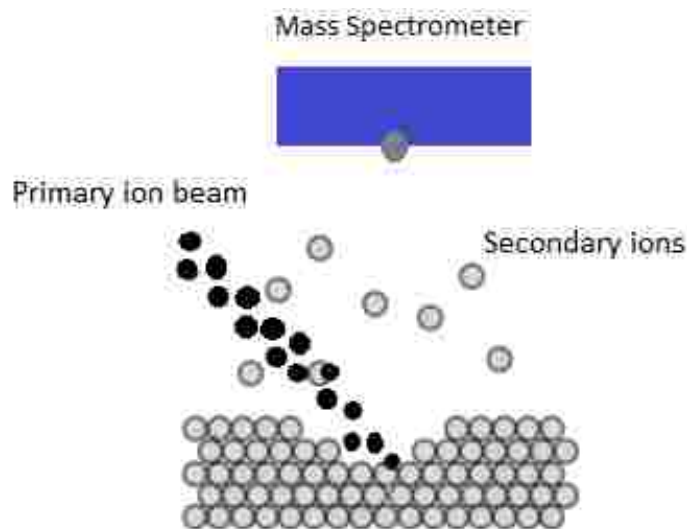
Figure 2.1 Schematic of a SIMS setup

SIMS depth profiles were used to characterize sodium and potassium concentrations as a function of substrate temperature. These depth profiles are shown in Figures 2.2 and 2.3. One can observe that the level of sodium concentration increases when T_{SS} is higher than room temperature, reaches a maximum at $T_{SS} = 100°C$ and subsequently starts to decrease as the T_{SS} is increased further (Figure 2.2). One can also observe a sharp edge at the molybdenum-glass interface. However, the accumulation of sodium at the molybdenum surface does not seem to differ very much for all temperatures. A similar trend is also seen in the potassium depth profile (Figure 2.3) where the maximum potassium level is at $T_{SS} = 100°C$ and subsequently starts to decrease as the T_{SS} is increased further. A sharp edge is also observed at the molybdenum-glass interface.
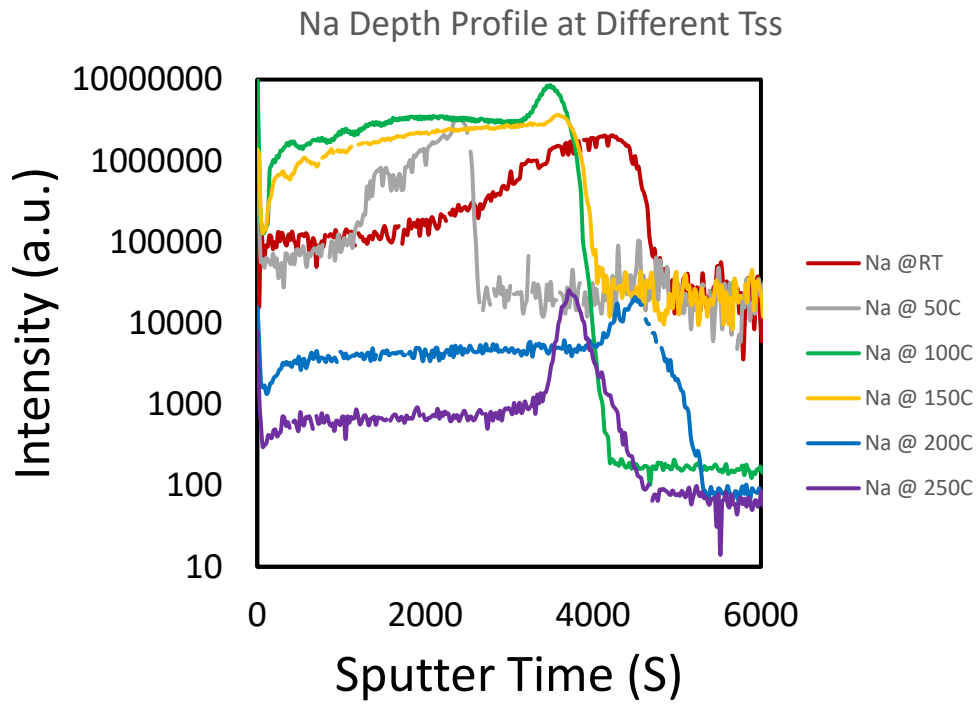
Figure 2.2 SIMS depth profile of Na as a function of substrate temperature.
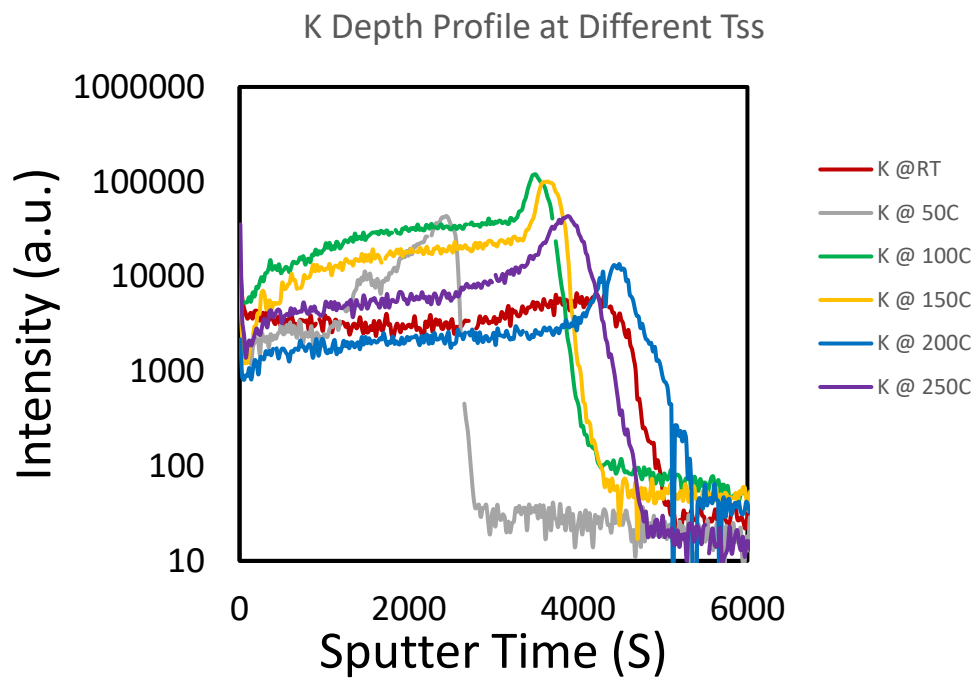
Figure 2.3 SIMS depth profile of K as a function of substrate temperature.

2.2.2   SCANNING ELECTRON MICROSCOPY (SEM)

Scanning electron microscopy is used to examine the microstructure of solid surfaces. Using SEM, we can determine the chemical composition, surface morphology, crystal structure and orientation of a sample. It produces high-resolution and high-magnification images of samples by using a focused high-energy electron beam in a raster-scan pattern that interacts with the atoms of the sample to generate a variety of signals at the surface of the samples. These signals may include secondary electrons (which produce SEM images), backscattered electrons (used to determine the bulk properties of the sample), diffracted backscattered electrons (used to determine crystal structures and orientations), characteristic x-rays (used for elemental analysis), photons and heat.

A SEM comprises of an electron source (gun), an electron lens condenser system, sample stage, an aperture control, electron detectors and an output display. Electron with energies 0-30 eV are detected and utilized to produce the image in secondary electron mode. These electrons are ejected from within a few nanometers of the surface of the specimen (Figure 2.4).
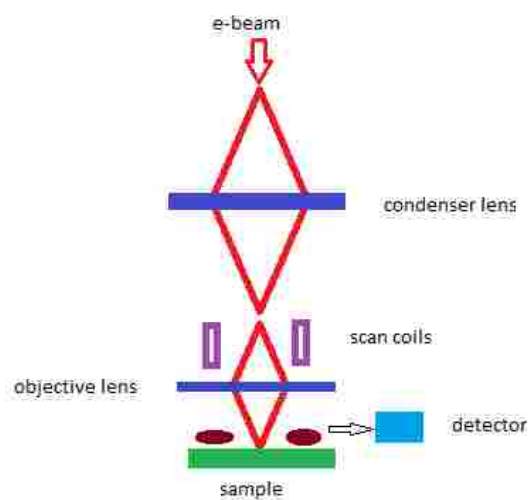
Figure 2.4 Schematic of SEM setup

The plan-view and cross-sectional SEM images of all as-deposited Mo films are presented in Figure 2.5. All molybdenum films show a columnar grain structure.
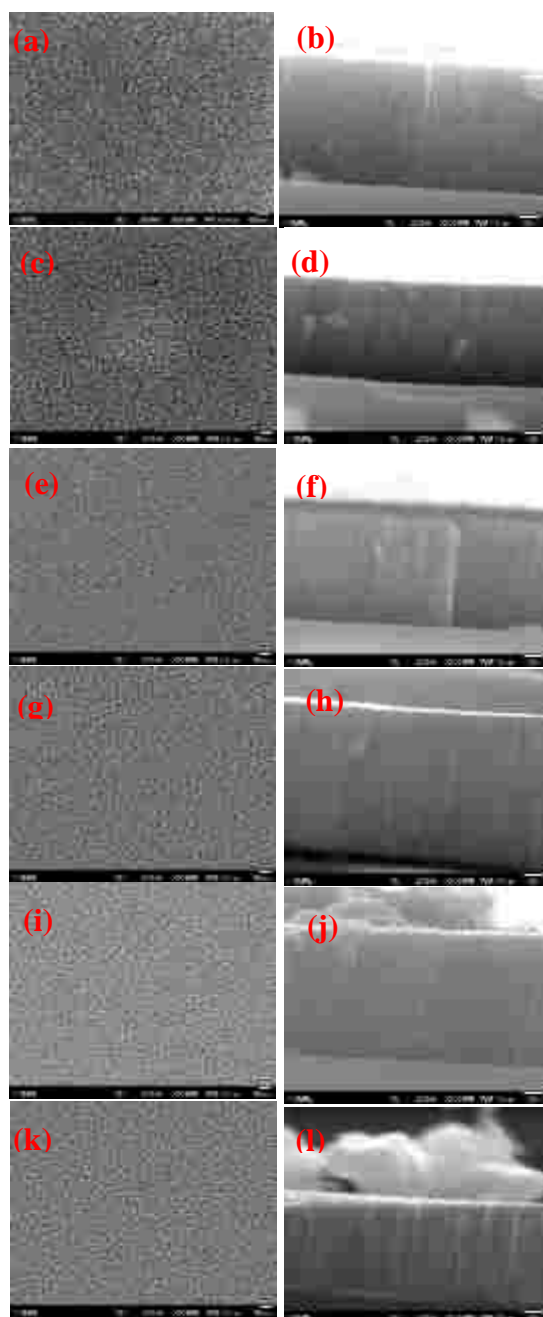
Figure 2.5 Plan-view (left) and cross-sectional (right) SEM images of the various Mo films on SLG as a function of T_{SS}: (a) and (b): RT; (c) and (d): 50 °C; (e) and (f): 100 °C; (g) and (h): 150 °C; (i) and (j): 200 °C; (k) and (l): 250°C.

The molybdenum layer thickness values (shown in Chapter 3 of this thesis) obtained above using SEM will be used in developing theoretical models to compare to our experimental SIMS data.

2.2.3   X-RAY PHOTOELECTRON SPECTROSCOPY (XPS)

X-ray photoelectron spectroscopy (XPS) is a quantitative surface analysis used to obtain elemental composition, and the electronic and chemical state of the elements present in a material. It is most suited for compositional analysis of ultra-thin films because the typical analysis depth of the XPS is less than 5 nm. A sample is irradiated with a beam of x-rays causing photoelectrons to be emitted from its surface. The kinetic energy of the emitted photoelectrons is subsequently measured using an electron energy analyzer. The chemical state, elemental composition and quantity of a detected element can be obtained from the binding energy and intensity of a photoelectron peak (Figure 2.6).
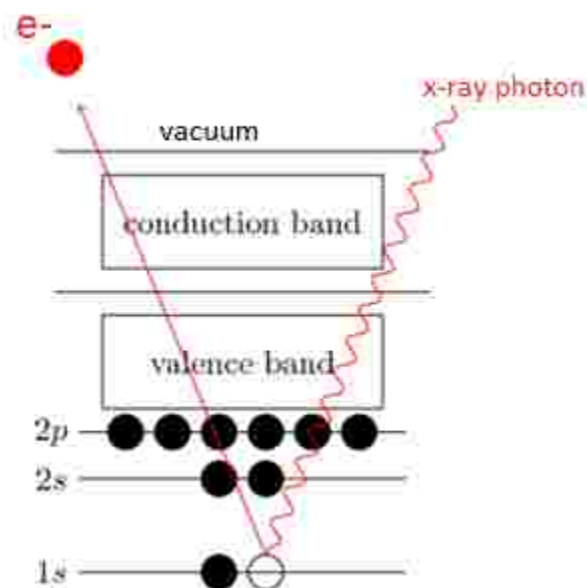
Figure 2.6 Schematic of an XPS setup

XPS analysis was performed on the molybdenum films to detect the oxidation states present in the films. XPS was performed before and after sputtering the surface of the molybdenum films.
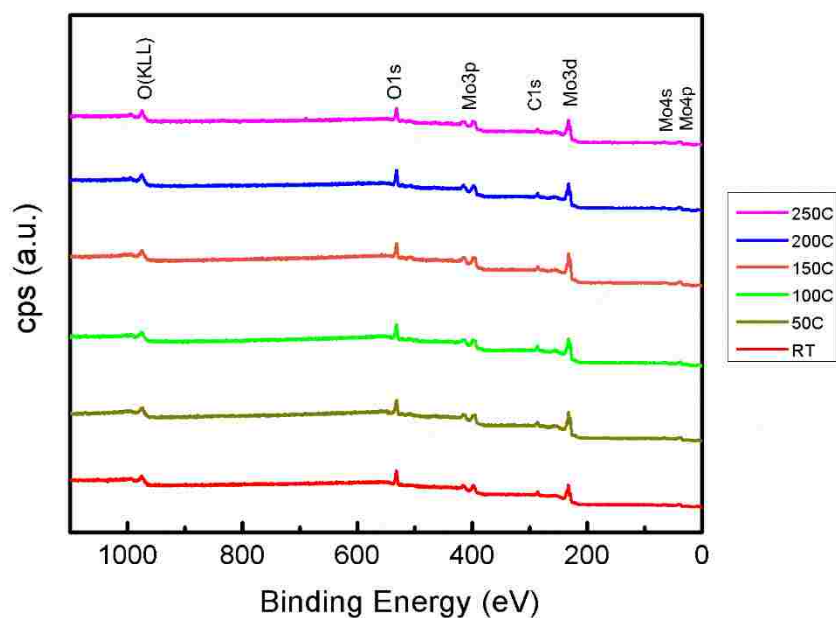
Figure 2.7 High-resolution XPS survey scans before sputtering the surface of the Mo films deposited by DC magnetron sputtering at different substrate temperatures.
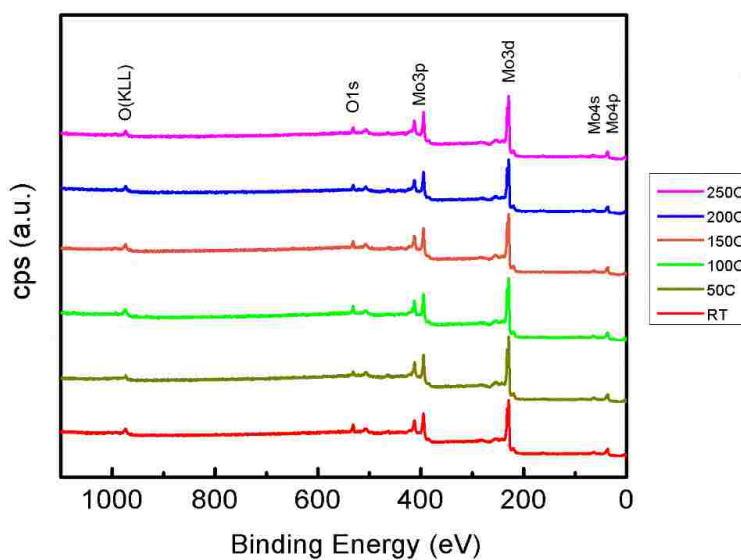
Figure 2.8 High-resolution XPS scans after sputtering the surface of the Mo films deposited by DC magnetron sputtering at different substrate temperatures.

The surface was heavily oxidized before sputtering was performed, with a mix of oxide and metallic peaks. Once sputtering was performed, the oxygen signal was shown to decrease significantly from around 70-80 at% to 15-30 at% as seen from Figure 2.9.
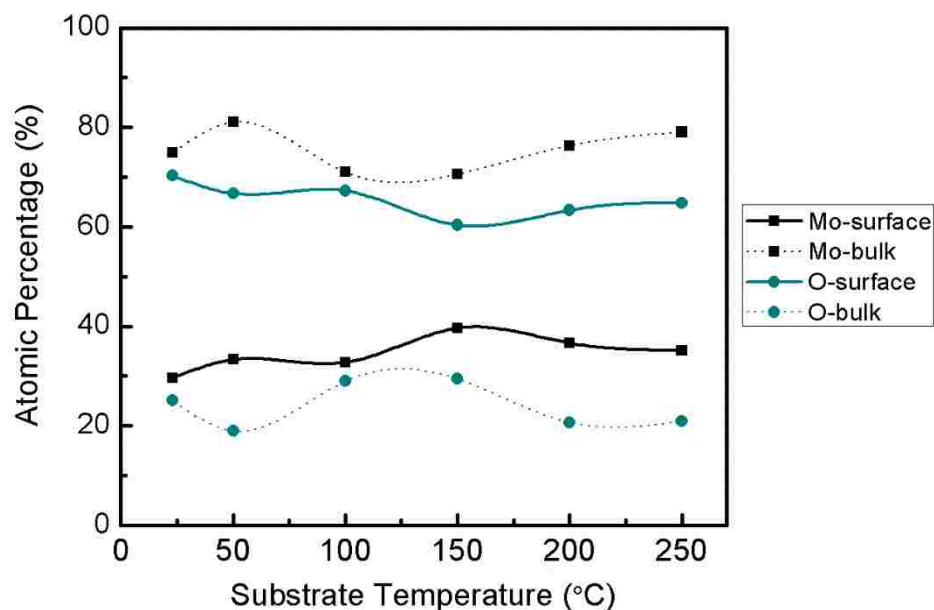
Figure 2.9 Atomic percentages of molybdenum and oxygen in the surface and bulk at different substrate temperatures.

The effect of oxidation on the molybdenum samples would prove to be useful later in explaining our results.

2.2.4   X-RAY DIFFRACTION (XRD)

X-ray diffraction is a characterization technique used to determine the crystallinity of a compound. When an incident beam of monochromatic x-rays impinges on the surface of a sample

material, these x-rays are scattered by the atoms in the material (Figure 2.10). If the material is crystalline, the x-rays undergo both constructive and destructive interference (i.e. diffraction). This diffraction can be described by Bragg's law:

$$2d \sin\theta = n\lambda$$

where θ is the incident angle, λ is the wavelength of the beam, d is the space between diffracting planes and n is any integer

X-rays are diffracted at different directions based on the size and shape of the unit cell of the material. When the diffraction spectrum of a sample is plotted as a function of 2θ, diffraction peaks appear, when Bragg's law is satisfied. The diffraction angle, the number of peaks and their intensity depend on the crystal structure, symmetry and lattice constant. Important information such as crystal orientation, phase and lattice constants is extracted by comparing the diffraction peaks with an XRD database. The x-ray penetration depth can be varied by changing the incident angle of the x-ray beams.
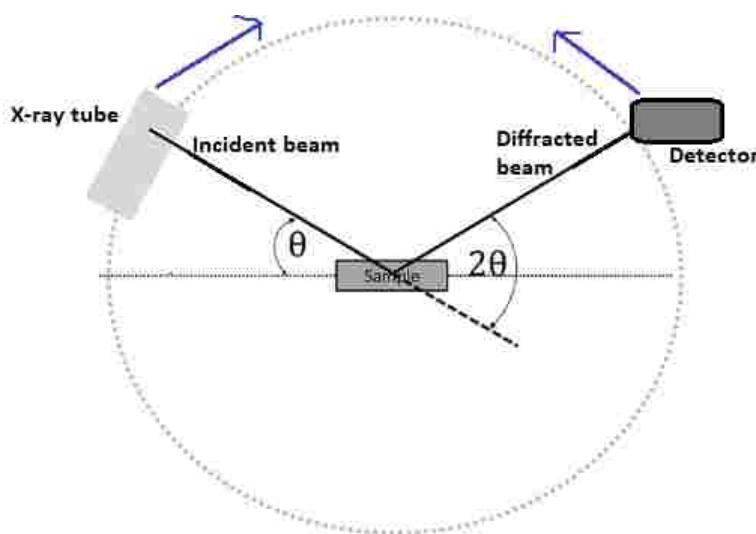
Figure 2.10 Schematic of XRD setup

XRD analysis was performed on our molybdenum samples to obtain the grain size/width

required to create our theoretical models.
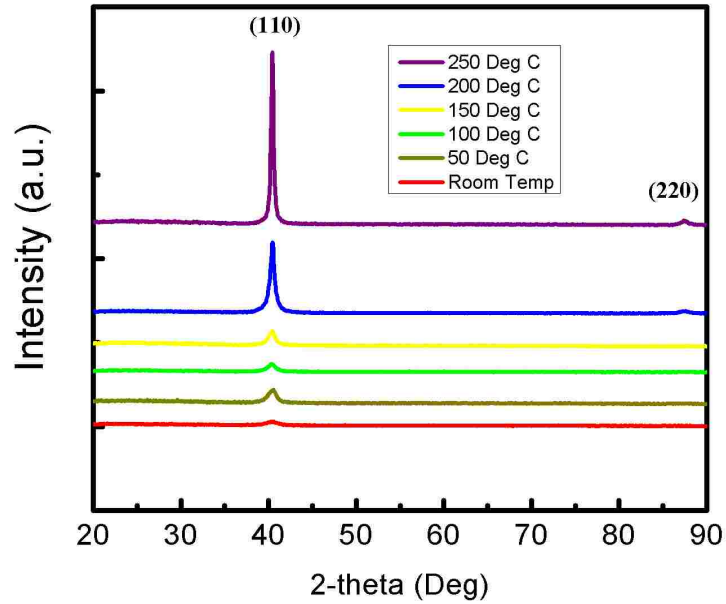
Figure 2.11 XRD spectra of the various Mo films on SLG as a function of substrate temperature.
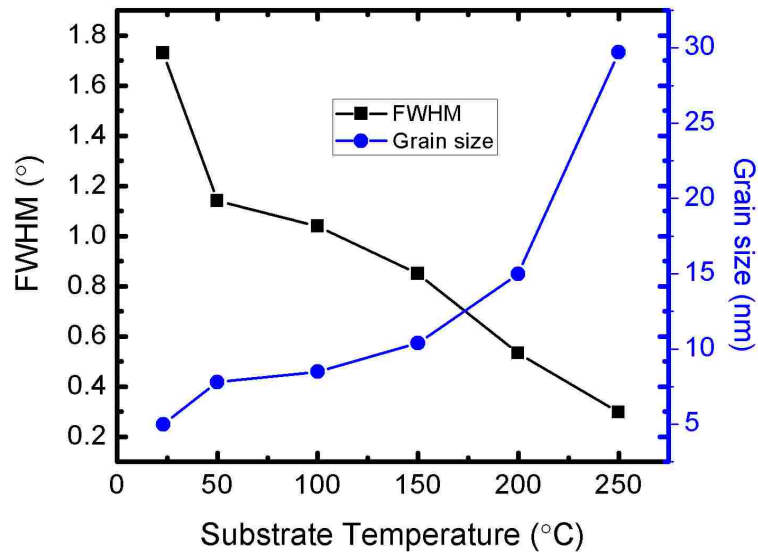
Figure 2.12 Relationship between FWHM and grain size of the various Mo films on SLG as a function of substrate

temperature

The results indicate that the preferred orientation of the moly films is along the <110> direction (Figure 2.11) but most importantly that the grain size increases with increasing substrate temperature (Figure 2.12) and reaches a maximum of almost 30 nm at a substrate temperature of $250^{o}C$.

CHAPTER 3

3 DIFFUSION OF IMPURITIES THROUGH THE MOLYBDENUM FILM

3.1 INTRODUCTION

Impurities have been shown to have a beneficial effect on CIGS solar cells. They can be introduced or incorporated into the CIGS absorber layer using different methods. Some impurities such as sodium and potassium can be found in the soda-lime glass substrate (providing high Na doping and low K doping). These impurities diffuse through the molybdenum back contact and into the CIGS absorber layer during the high temperature growth process of the CIGS layer. This method is cheap and straightforward, but the major problem associated with it is the inability to control the amount of impurities, say Na, supplied into the CIGS absorber layer, which results in a non-uniform distribution over some areas of the cell and unknown concentration profile.

To better control the amount of impurities in the device, alkali free substrates are sometimes used or a diffusion barrier is deposited onto the glass substrate prior to the Mo film growth. Thereafter, post-deposition treatment (PDT) using NaF and/or KF precursor is performed immediately after CIGS growth; alternatively, deposition of the precursor onto the Mo layer prior to CIGS growth is performed. In the former method, the Na/K incorporation is independent of CIGS growth and thus does not affect film growth, while in the latter, Na/K exist during the entire CIGS deposition process and thus directly impact the film growth. The different impurity incorporation methods result in different effects on the CIGS film, but regardless of how they are introduced into the solar cell, it has been shown that these alkali elements, especially sodium, are essential for achieving high efficiency cells.

These impurities tend to diffuse very quickly through defects and grain boundaries found in the Mo back contact. Thus, understanding the effect of the microstructure and geometry of the Mo layer is crucial in regulating the amount of impurity diffusion. Alkali elements play a significant role in the performance of the CIGS solar cell as discussed below.

3.1.1 EFFECT OF IMPURITIES ON DEVICE PERFORMANCE

Sodium has been shown to have the most significant effect on the properties and performance of CIGS solar cells. CIGS cells typically require about 0.1 at.% Na content incorporated into the CIGS absorber layer to be highly efficient [6]. Na has been shown to reduce CIGS grain size, improve open-circuit voltage and fill factor, increase p-type conductivity, enhance CIGS grading profile - [Ga]/([Ga] + [In]), prevent metal interdiffusion and increase the <112> orientation of the CIGS film, which is its preferred orientation [7]. Other alkali elements such as K, Li and Cs have been reported to have similar effects as Na, but at a minimized level. It has also been reported that the incorporation of an additional alkali source into the absorber besides Na leads to even higher increase in cell efficiency.

The effect of Na and K on device performance was studied previously [8]. Na and K were introduced into the CIGS absorber layer using three main methods: out-diffusion of Na and K from the SLG substrate, coevaporation of KF with the CIGS layer and a KF PDT. Different combinations of an SiO_2 diffusion barrier was used with the two incorporation methods. 2 mm thick SLG substrates with either a 0.8 um sputtered Mo film or 20-30 nm of sputter SiO_2 diffusion barrier followed by 250 nm of sputtered Mo was used to minimize the diffusion of Na and K from the substrate. A 2 um thick CIGS layer was deposited using thermal coevaporation. In general, all three methods lead to an increase in carrier concentration, open-circuit voltage, fill factor, and

power conversion efficiency. Specifically, it was shown that solar cells fabricated by the KF coevaporation method with no diffusion barrier exhibited the largest photovoltaic conversion efficiency. The use of a KF precursor also seemed to enhance the diffusion of Na from the substrate.

Laemmle et al [6] also investigated the effect of potassium on the growth kinetics of the CIGS layer and electrical properties of the device fabricated on alkali-free alumina substrates. Potassium was introduced into the CIGS layer by K doping using precursor layer and KF PDT. SEM images revealed smaller CIGS grains for the KF-precursor sample than those of the KF-PDT sample and K-free reference sample. J-V measurements showed an increase in cell conversion efficiency for both KF precursor and KF-PDT samples when compared to the reference cell. Quantum efficiency measurements of the KF-precursor sample reveal increased absorption in the infrared region of the spectrum, while capacitance-voltage (C-V) measurements showed an increase in the net doping concentration of both KF-PDT and KF-precursor samples.

3.2   SINGLE LAYER MODELING USING EXCEL

Diffusion in semiconductors involves the atomic movement of dopant atoms in the crystal lattice by vacancies or interstitials. Adolf Fick, in the 19th century, derived two laws known as Fick's Laws of Diffusion to provide a description for the mechanism of diffusion [9].

The first law states that the molar flux due to diffusion (or diffusive flux) is proportional to the concentration gradient in the diffusion direction. Diffusive flux (J) can be described as rate of transfer of the diffusant across a unit area of a section normal to the diffusion direction. Dopant atoms will move from a high-concentration region towards a low-concentration region. This law is expressed as follows:

$$J = -D\Delta C \tag{3.1}$$

where J is the diffusive flux, C is the concentration and D is the diffusion coefficient and depends heavily on the type of materials being used.

It is difficult to experimentally obtain the diffusivity, D, using equation (3.1) because it requires the measurement of the steady-state concentration gradient and steady state flux. A more suitable form of equation (3.1), known as Fick's Second Law of Diffusion, can be used to easily obtain the diffusivity value provided that the material balance across a volume of elements of the system is accounted for. Fick's second law states that the rate of change of concentration at a point in space is proportional to the second derivative of concentration with space. It can be derived from the first law as follows:

$$\frac{\partial C}{\partial t} = -\nabla \mathbf{J} \tag{3.2}$$

where t is the time. Assuming D is position independent and substituting J from equation (3.1) to (3.2), gives:

$$\frac{\partial C}{\partial t} = D\nabla^2 C \tag{3.3}$$

where ∇^2 is the Laplacian operator defined as:

$$\nabla^2 = \frac{\partial^2}{\partial x^2} + \frac{\partial^2}{\partial y^2} + \frac{\partial^2}{\partial z^2}$$

The main objective of this work is to predict the diffusion mechanisms of impurities from the glass through the molybdenum into the CIGS absorber layer. Thus, by fitting our experimental data to varying diffusion models, we are trying to obtain and understand appropriate modeling parameters such as: grains and grain boundaries size and geometry, diffusivity in the grain and the GBs, variation of these parameters as a function of deposition process parameters such as power, pressure, Tss, post-deposition temperature treatment.

To estimate the diffusion coefficient through the developed model, we can use either concentration data through depth profiling techniques (typically SIMS analysis) or surface accumulation data (obtained from XPS, etc.). Depth profiling techniques include diffusing a substance for a certain time and then measuring concentration as a function of depth. In this work, depth profiles obtained using secondary ion mass spectroscopy (SIMS) have been used.

The diffusion mechanism in polycrystalline solids involves mainly the use of vacancies. Interstitial diffusion can also occur if the diffusing atoms are significantly smaller than host material atoms. The dependency of vacancy formation results in much faster diffusion along the grain boundaries than in the grain because there is a higher likelihood of finding vacancies in the grain boundary [9]. The grain boundary diffusion coefficient tends to be several orders of magnitude larger than the grain diffusivity value. Diffusion in polycrystalline materials was categorized based on the differences among the average grain width, the grain diffusion length and the grain boundary width. This classification resulted in three types of diffusion profiles, namely types A, B, and C, where Type A is uniform diffusion through grains and grain boundaries, type B preferential diffusion through grain boundaries and type C is diffusion entirely through grain boundaries [11]. We will assume type C diffusion in the diffusion models discussed below.
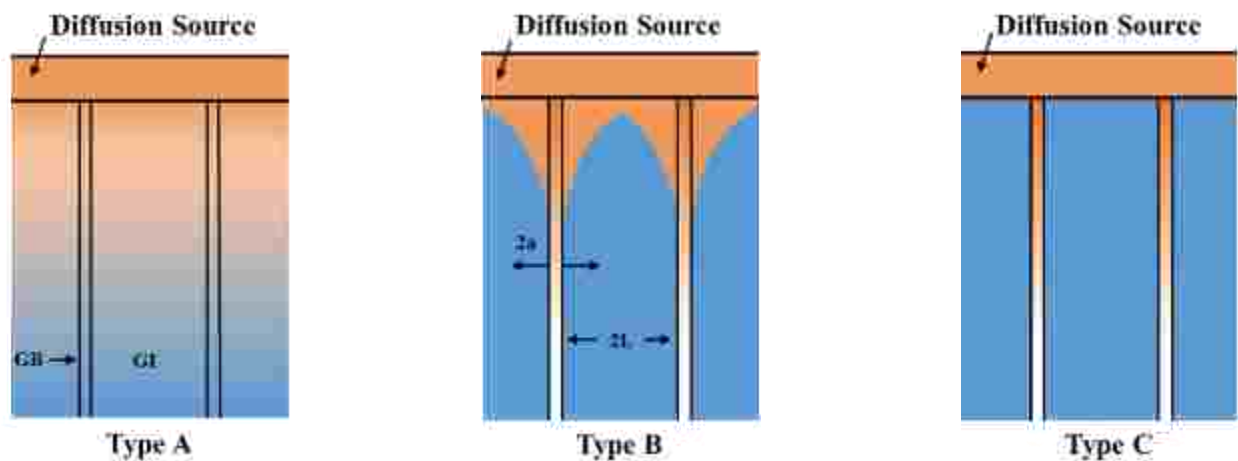

Figure 3.1 Schematic of the three diffusion models

We started out with some basic diffusion models based on constant-surface-concentration (CSC) diffusion and constant-total-dopant (CTD) diffusion. In the first instance, impurity atoms are transported from a source onto the semiconductor surface which subsequently diffuse into the semiconductor material, but the source maintains a constant level of surface concentration during the entirety of the diffusion time. In the second instance, a fixed amount of dopant is deposited onto the semiconductor surface, which is subsequently diffused into the semiconductor material [9].

The constant-surface-concentration diffusion profile provides a solution to equation 3.3 where the initial condition (which states that the initial dopant concentration is 0) at $t = 0$ is

$$C(x, 0) = 0 \qquad (3.4)$$

and boundary conditions are as follows:

$$C(0, t) = C_0 \qquad (3.5)$$

where C_0 is the surface concentration at x = 0 and it is independent of time

$$C(\infty, t) = 0 \qquad (3.6)$$

which states that there are no impurity atoms at large distances from the surface. The solution to equation 3.3 that satifies the initial and boundary conditions is given by:

$$C = C_0 erfc \left(\frac{x}{2\sqrt{Dt}} \right) \qquad (3.7)$$

where erfc is the complementary error funtion and $\sqrt{Dt}$ is the diffusion length.

For the constant-total-dopant diffusion profile, the initial condition is the same as in equation 3.4 but with the following boundary conditions:

$$\int_0^\infty C(x,t)dx = S \tag{3.8}$$

$$C(\infty, t) = 0 \tag{3.9}$$

where S is the total amount of dopant per unit area

The solution to equation 3.3 that satifies the initial and boundary conditions is given by:

$$C(x,t) = C(t)\exp(-\frac{x^2}{4Dt}) \tag{3.10}$$

where $C(t) = \frac{S}{\sqrt{\pi Dt}}$

3.2.1   SODIUM DIFFUSION MODEL

The constant-surface-concentration and constant-total-dopant diffusion models are in terms of concentration and film thickness whereas the SIMS data are provided in terms of intensity and sputter time. Since, there are varying units (time, thickness, intensity and concentration) on all four axes being compared, we had to normalize both the SIMS data and the diffusion models. We first normalized the SIMS data, then we converted our normalized time values into film thickness values using the following relation:

$$x = (1 - normalized\ time) * thickness \tag{3.11}$$

x is used in equations 3.7 and 3.10 to obtain the concentration profiles of both diffusion models. The concentration profiles are then normalized as well for easy fitting in Excel.

The film thickness values are listed in Table 3.1 below and the molybdenum deposition time was experimentally imposed to be 90 minutes long or 5400 seconds.

T$_{SS}$ (°C)	Film Thickness (nm)
23	550
50	450
100	500
200	530

Table 3.1 Value of the molybdenum thin film thickness used in this study for various Tss

The Solver function in Excel was used in fitting the diffusion models to the experimental SIMS data. We applied the sum of squared errors of prediction (SSE) to the Solver function to get the best fit possible.

Figure 3.2 shows a plot comparing the normalized data from the constant-surface-concentration diffusion wafer (a slab of molybdenum with no grain boundary) model with the normalized experimental SIMS data, for deposition temperatures of 23 (room temperature), 50, 100 and 200°C. The model fit very well for RT and 50°C, but did not fit at all for 100 and 200°C because the depth profile has a different shape, which might indicate a different diffusion mechanism and/or additional chemical reactions taking place as the film is grown. It might be a type A or type B diffusion process; there might be a lot more sodium diffusing through the grain, which would void our type C assumption for this model. This will be investigated later with a type A/type B diffusion model where the assumption is made that some sodium actually diffuses through the bulk/grain.
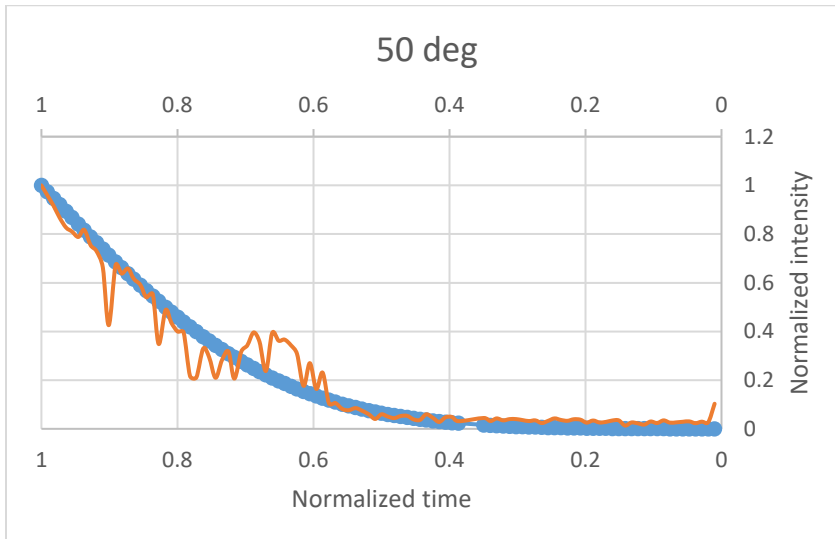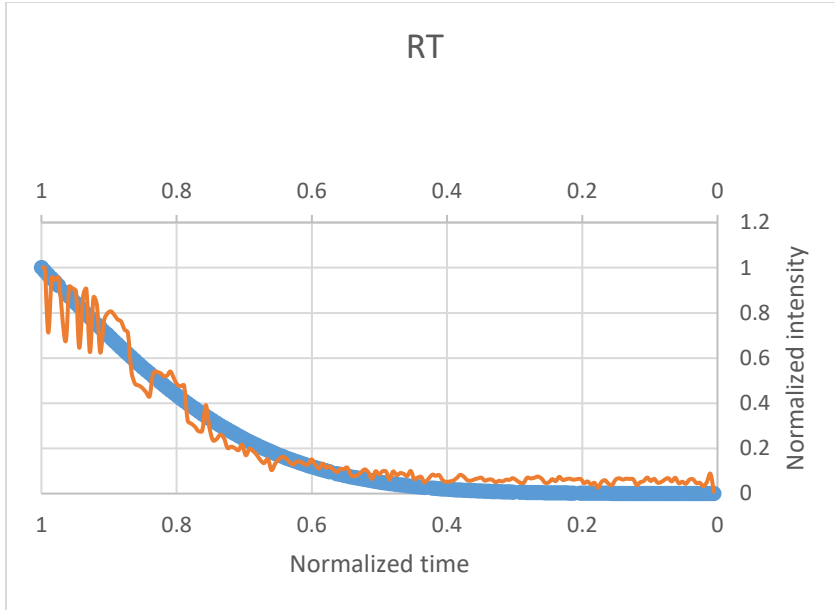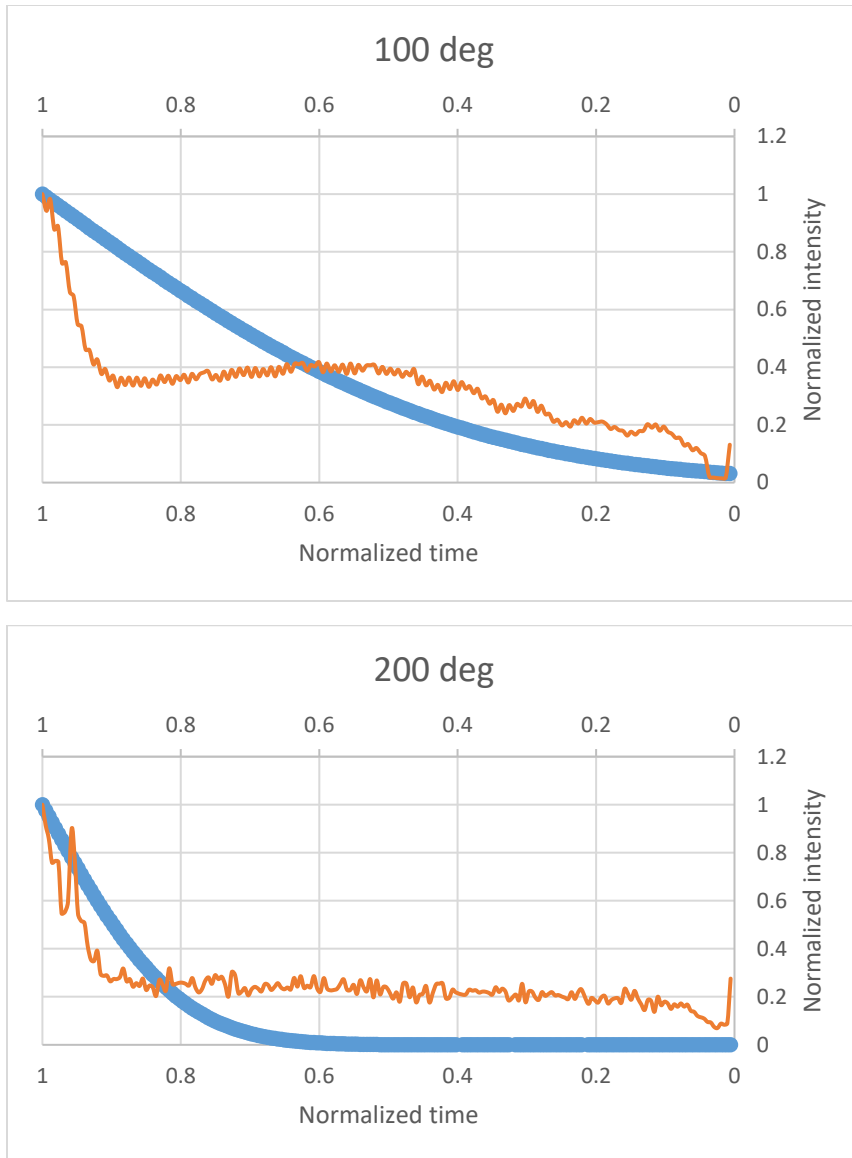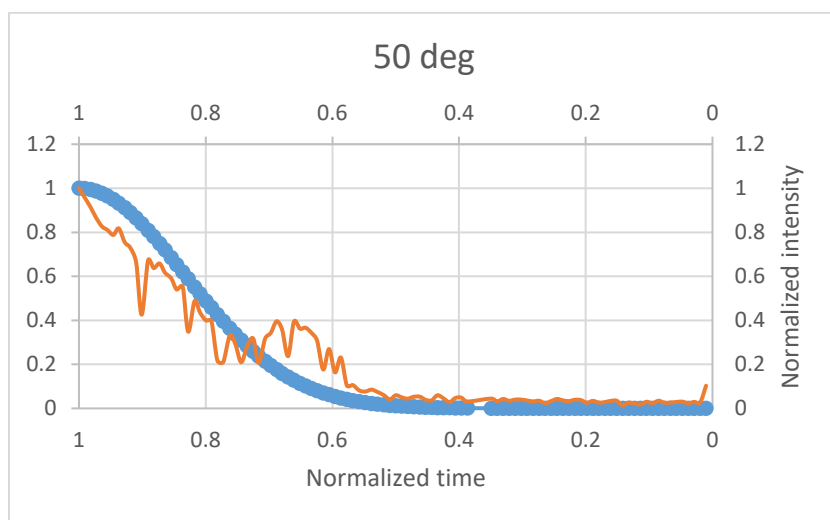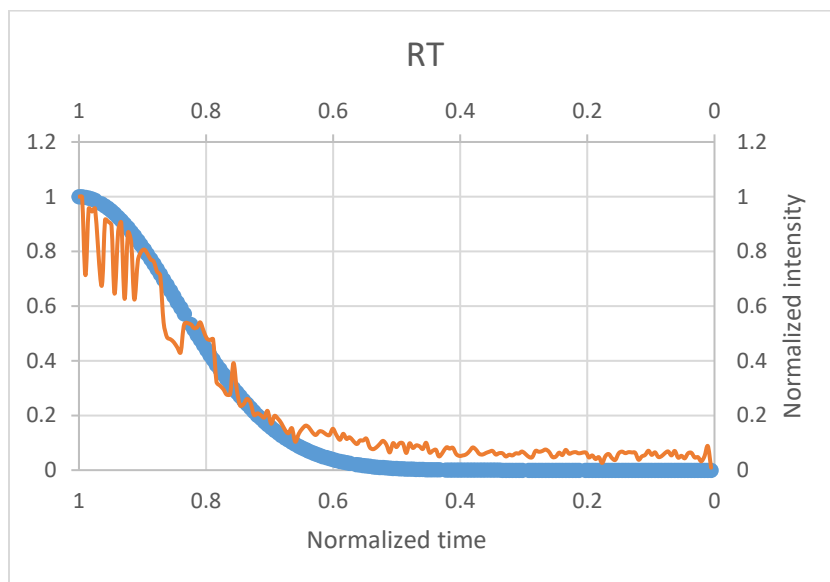
Figure 3.2 Comparison of the experimental SIMS profile (orange line) and the CSC wafer model (blue line)

Next, we tried using the constant-total-dopant wafer (a slab of molybdenum with no grain boundary) model to fit the SIMS data. Figure 3.3 shows a plot comparing the normalized data from the constant-total-dopant diffusion model with the normalized experimental SIMS data, for deposition temperatures of 23 (room temperature), 50, 100 and 200ºC. Like the earlier model, this model fit very well for RT and 50ºC but did not fit again for 100 and 200ºC, which might indicate

a different diffusion process and/or additional chemical reactions taking place as the film is grown.

A type A or type B diffusion process might be at play here.
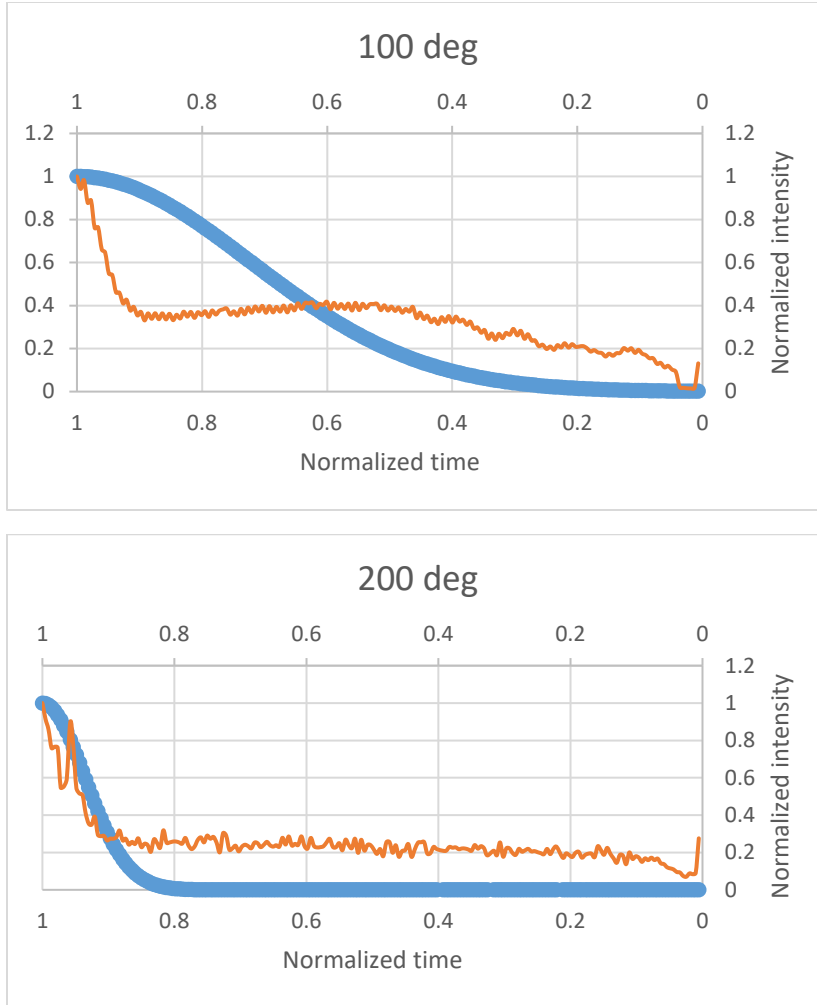
Figure 3.3 Comparison of the experimental SIMS profile (orange line) and the CTD wafer model (blue line)

The values of the grain boundary diffusivities extracted from both models are reported Table 3.2.

	Diffusivity (cm^2/s)	
Tss (^{0}C)	CSC	CTD
23	1.84e-14	6.89e-15
50	1.37e-14	5.24e-15
100	4.91e-14	1.77e-14
200	5.98e-15	1.06e-15

Table 3.2 Diffusivity coefficients of sodium into molybdenum as a function of Tss, extracted for CSC and CTD models.

Due to our constant inability to fit the SIMS data for 100 and 200ºC, we had to rethink our earlier assumption that type C diffusion mechanism is so dominant that the type A/B diffusion mechanisms are rendered insignificant. We also decided against assuming a constant initial surface concentration value like we did for the earlier models. Thus, we had the Solver function find the best fit using four variables, namely: grain diffusivity (D_{grain}), grain boundary diffusivity ($D_{boundary}$), initial grain concentration (C_{grain}) and initial grain boundary concentration ($C_{boundary}$) instead of just the grain boundary diffusivity like we had for the earlier models. Therefore, the Solver function tried to minimize the sum-squared error value using these four variables.

So, we ran 3 diffusion models (CSC, CTD and a combination of both), but this time, we did not make any assumptions. The results obtained from Solver function would essentially determine the dominant mechanism and we would compare that with our initial models.

Figure 3.4 shows a plot comparing the normalized data from the constant-surface-concentration polycrystalline (grain and grain boundary included) model with the normalized experimental SIMS data, for deposition temperatures of 23 (room temperature), 50, 100 and 200ºC.
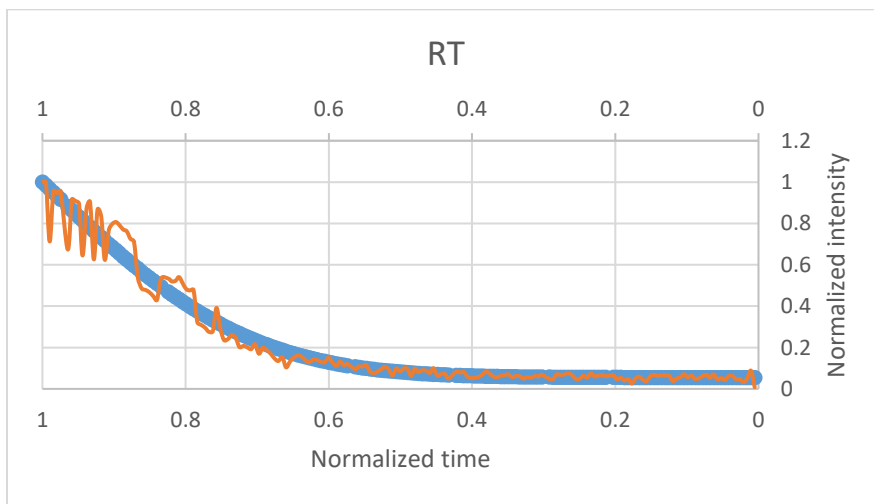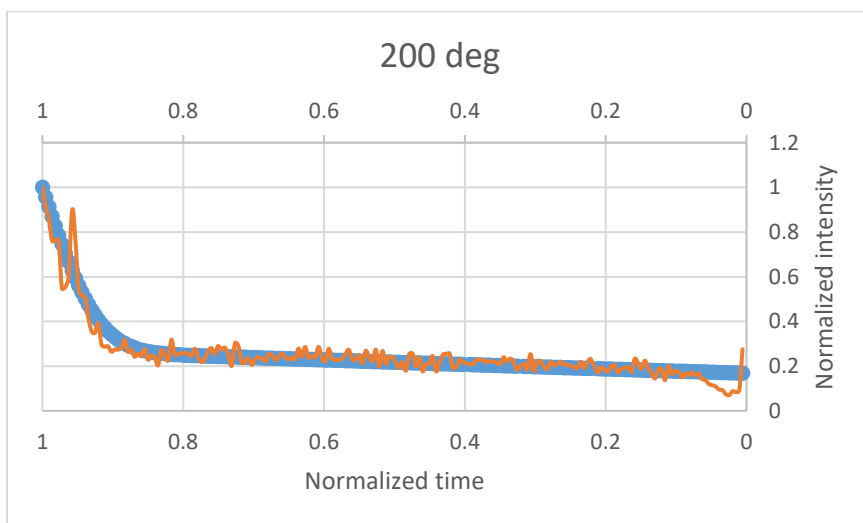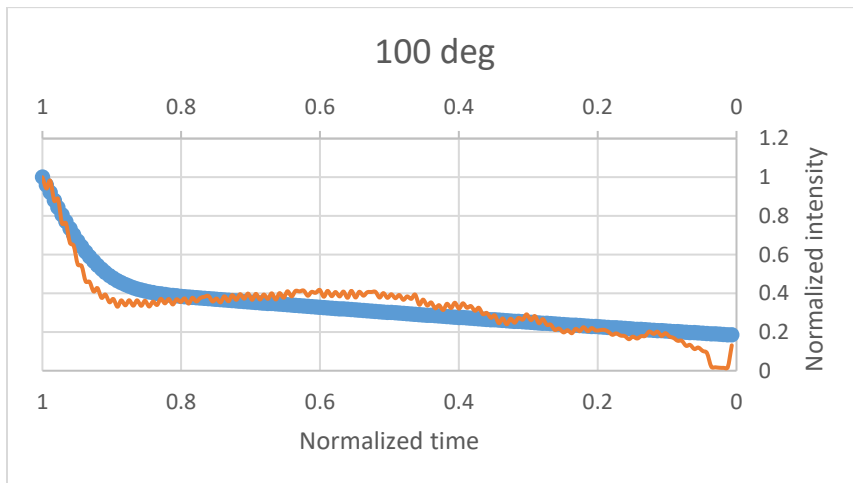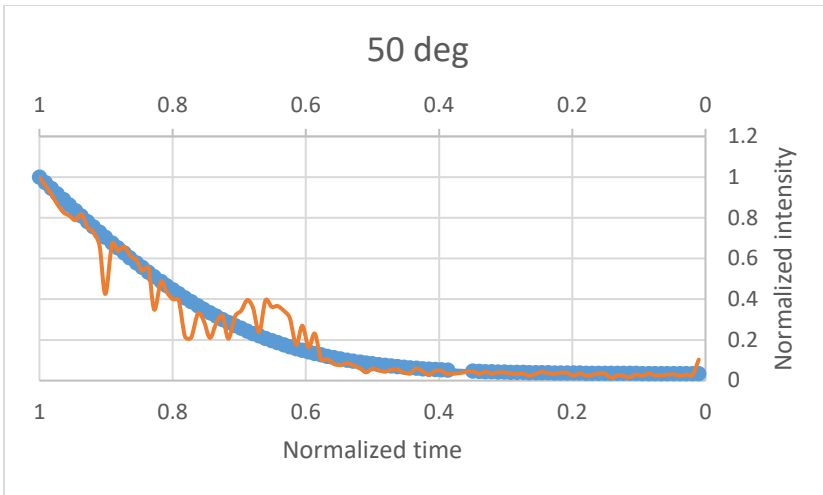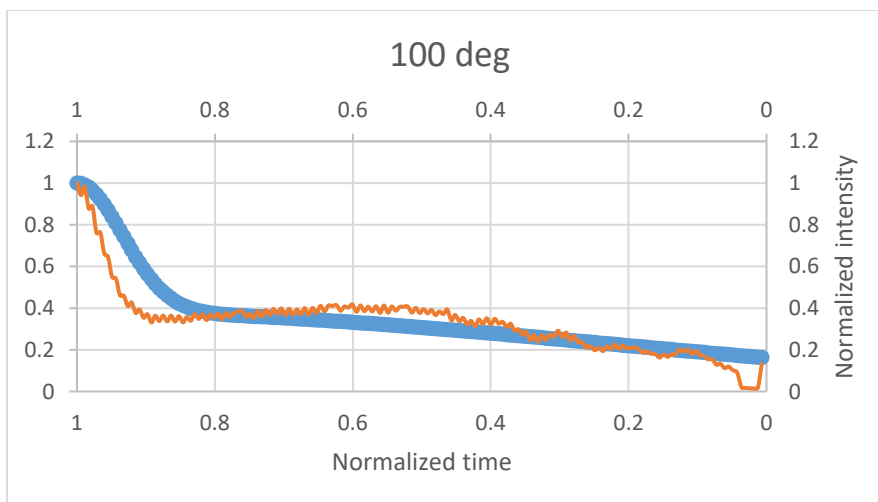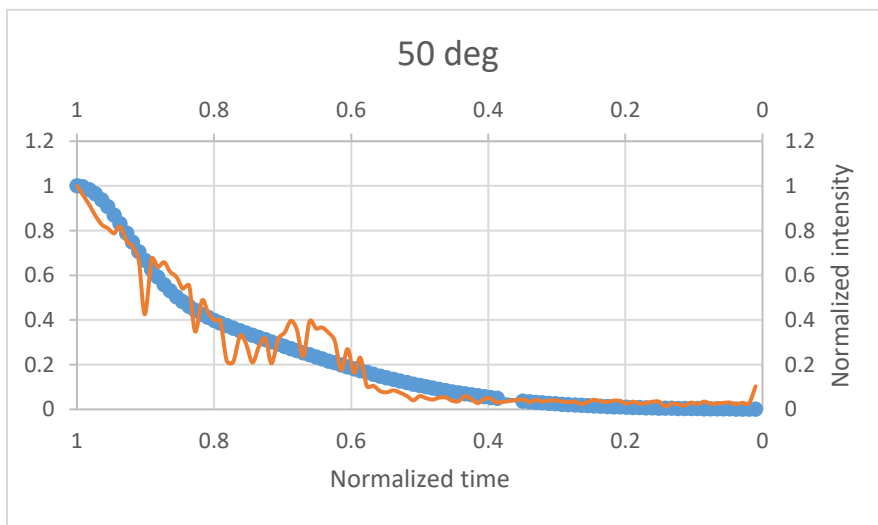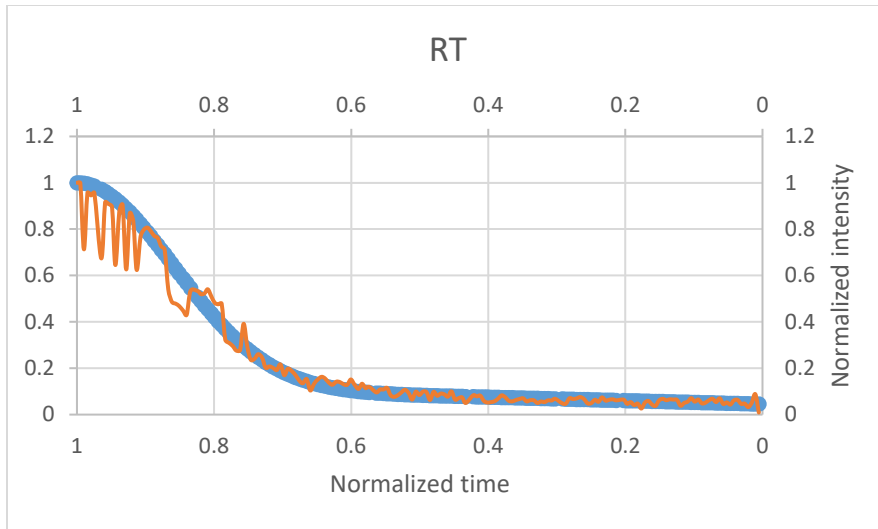
Figure 3.4 Comparison of the experimental SIMS profile (orange line) and CSC polycrystalline model (blue line)

This time, we could fit the SIMS data for all temperatures. A closer look at the diffusivity and concentration values for all temperature data in Table 3.3 indicates a type B diffusion mechanism but with a dependence on varying initial concentration values. RT and 50 °C data specifically show a larger disparity in the initial concentration values of the grain and grain boundary, which might be because a lot of sodium, unable to properly diffuse through the grain due to its low diffusivity, accumulates at the grain interface.

Tss (°C)	D_{grain} (cm²/s)	$D_{boundary}$ (cm²/s)	C_{grain} (mol/m³)	$C_{boundary}$ (mol/m³)
23	1.44e-14	1.00e-10	147.15	8.80
50	1.17e-14	2.04e-12	66.46	3.06
100	1.00e-15	3.52e-13	80.54	63.08
200	1.00e-15	1.08e-12	81.34	30.03

Table 3.3 Diffusivity coefficients and concentration values of sodium into molybdenum as a function of Tss

Next was the constant-total-dopant polycrystalline model; Figure 3.5 shows a plot comparing the normalized data from the constant-total-dopant model with the normalized experimental SIMS data.
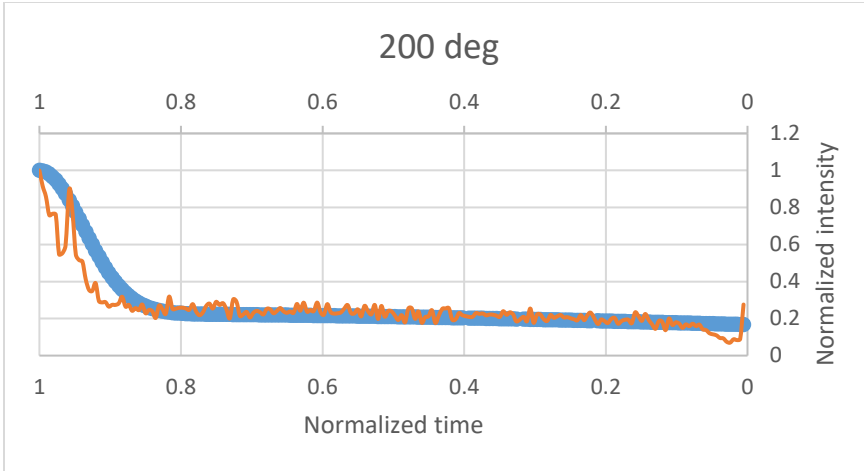
RT

50 deg

100 deg

Figure 3.5 Comparison of the experimental SIMS profile (orange line) and CTD polycrystalline model (blue line)

We could fit the SIMS data for all temperatures. A closer look at the diffusivity and concentration

values for all temperatures in Table 3.4 suggest a type B diffusion process which seems logical.

There is also a reliance on varying initial concentration values of the grain and boundary. A much

larger disparity in initial concentration values is noticed at RT and 200°C.

Tss (°C)	D_{grain} (cm²/s)	$D_{boundary}$ (cm²/s)	C_{grain} (mol/m³)	$C_{boundary}$ (mol/m³)
23	5.51e-15	1.75e-13	102.17	11.36
50	1.00e-15	1.53e-14	5.74	5.62
100	1.00e-15	1.34e-13	77.22	47.49
200	1.00e-15	4.26e-13	155.18	45.56

Table 3.4. Diffusivity coefficients and concentration values of sodium into molybdenum as a function of Tss

Finally, we tried combining the effects of the CSC and CTD polycrystalline models, which are

shown on the plots in Figures 3.6 and 3.7. For the plots in Figure 3.6, we applied CTD to the grain

boundary and CSC to the grain. For the plots in Figure 3.7, we applied CSC to the grain boundary

and CTD to the grain.

RT

50 deg

100 deg
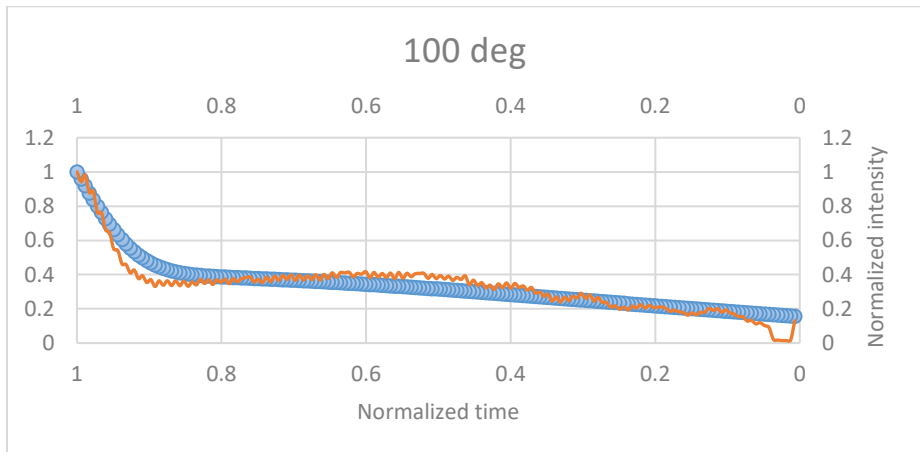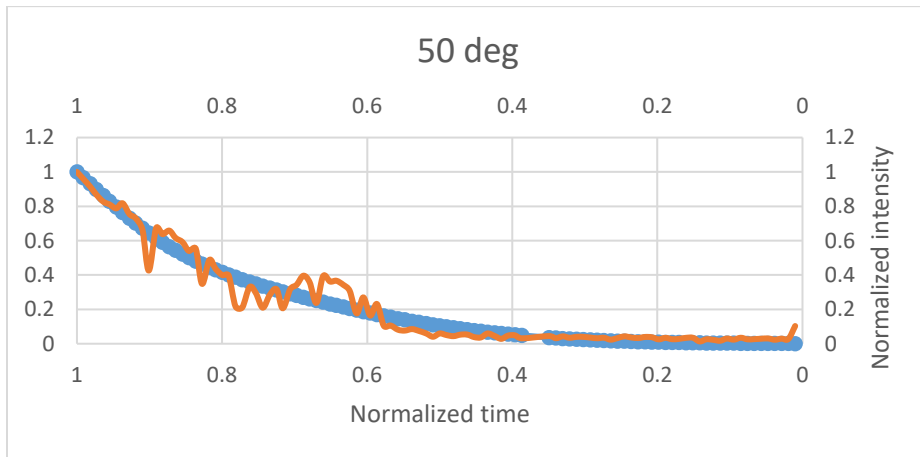
Figure 3.6 Comparison of the experimental SIMS profile (orange line) and CSC & CTD models (blue line)

We were able to fit the data for all temperatures and the data in Table 3.5 below suggests a type

B mechanism for all temperatures with some dependence on a varying initial concentration.

Tss (^{0}C)	D_{grain} (cm^2/s)	$D_{boundary}$ (cm^2/s)	C_{grain} (mol/m^3)	$C_{boundary}$ (mol/m^3)
23	4.57e-15	1.25e-13	63.93	17.84
50	2.19e-15	1.52e-14	26.23	25.25
100	1.00e-15	1.22e-13	75.26	50.10
200	1.00e-15	3.24e-12	120.45	36.44

Table 3.5. Diffusivity coefficients and concentration values of sodium into molybdenum as a function of Tss

The plots from the second combination of the CSC and CTD diffusion models are shown in

Figure 3.7 below.

RT

Normalized intensity

Normalized time

50 deg

Normalized intensity

Normalized time

100 deg

Normalized intensity

Normalized time

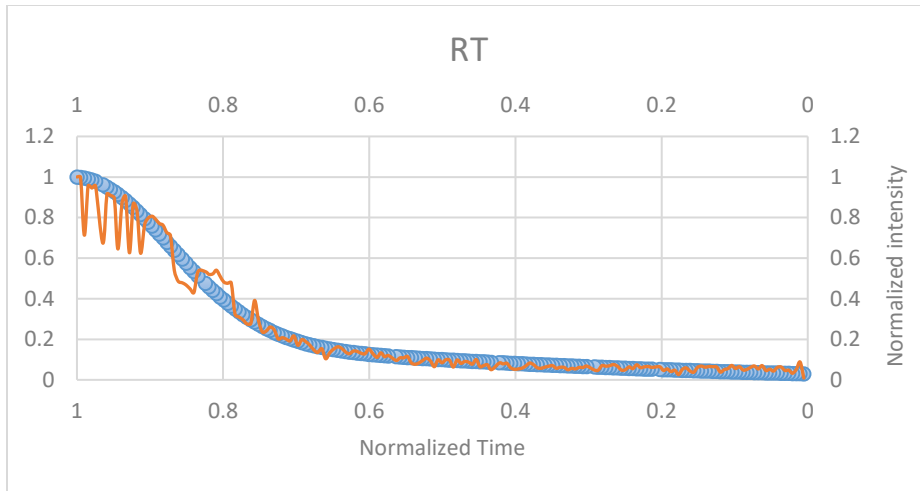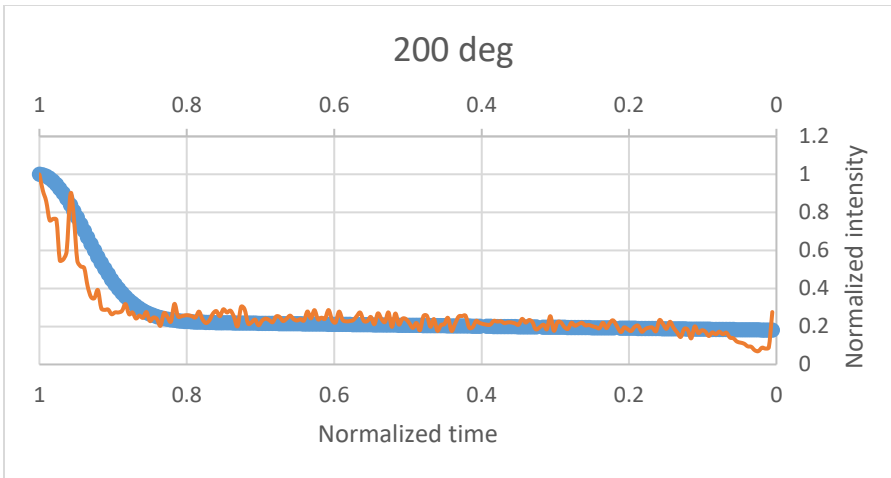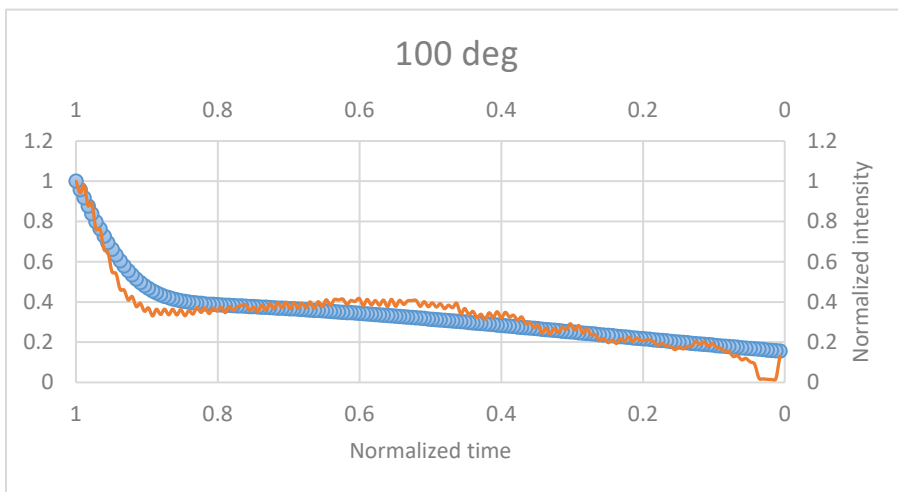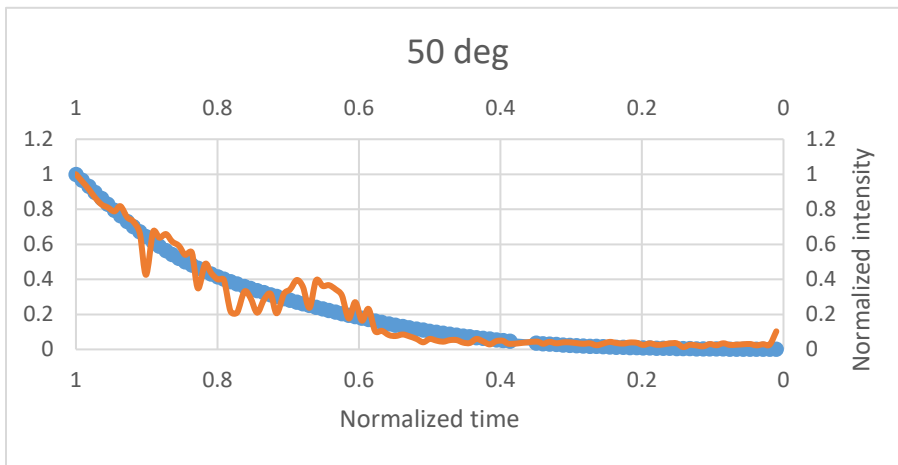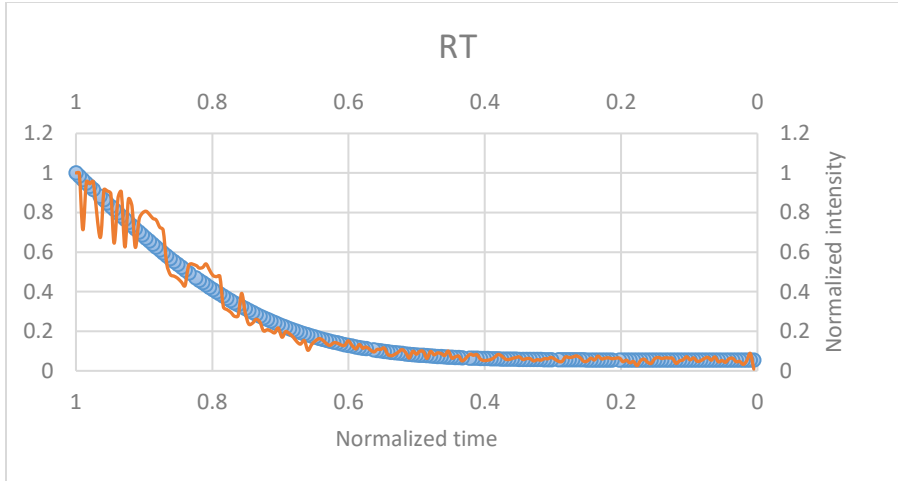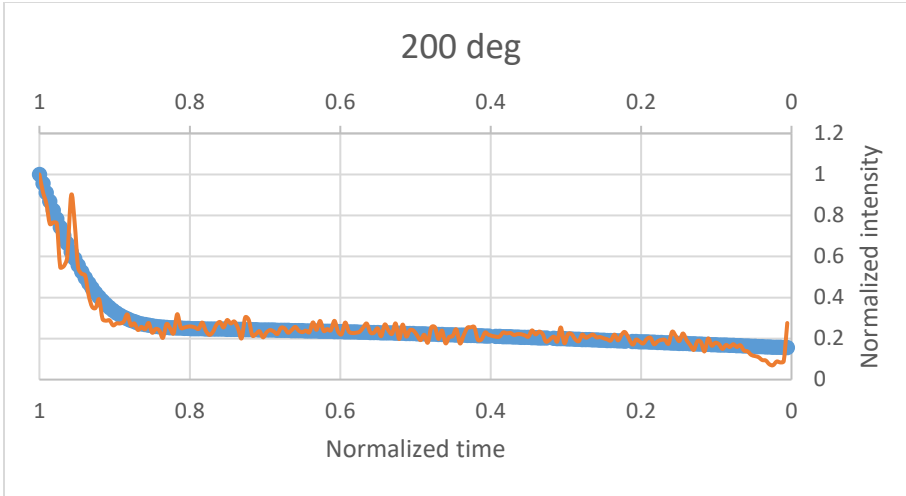Figure 3.7 Comparison of the experimental SIMS profile (orange line) and CSC & CTD models (blue line)

We could fit the data for all temperatures, and the data in Table 3.6 below suggests a type B mechanism for all temperatures with some dependence on a varying initial concentration. There seems to be a large disparity in initial concentration values for RT, 100 and 200°C.

Tss (^{0}C)	D_{grain} (cm^2/s)	$D_{boundary}$ (cm^2/s)	C_{grain} (mol/m^3)	$C_{boundary}$ (mol/m^3)
23	1.45e-14	1.00e-10	141.42	8.12
50	2.18e-15	1.52e-14	13.25	12.76
100	1.00e-15	1.22e-13	116.01	77.23
200	1.00e-15	2.64e-13	120.87	40.93

Table 3.6. Diffusivity coefficients and concentration values of sodium into molybdenum as a function of Tss

3.2.2 POTASSIUM DIFFUSION MODEL

We ran a similar analysis to extract the diffusivity values for a potassium impurity at the same temperatures. We also used the CSC and CTD diffusion models in our attempt to fit the experimental SIMS data, but this time we encountered problems when trying to fit the data for RT,

100 and 200ºC. A similar initial assumption of a type C diffusion mechanism and a constant initial concentration were made.

Figure 3.8 shows the plot fits using the CSC wafer model at 23, 50, 100 and 200ºC.
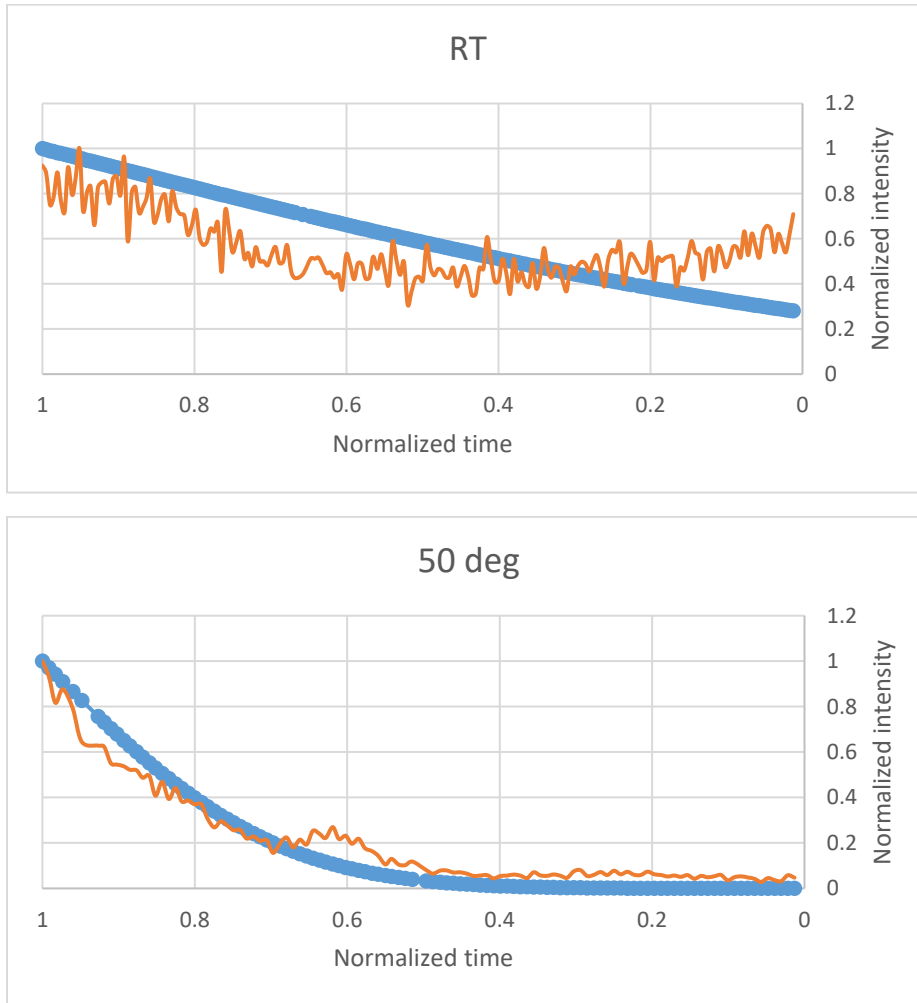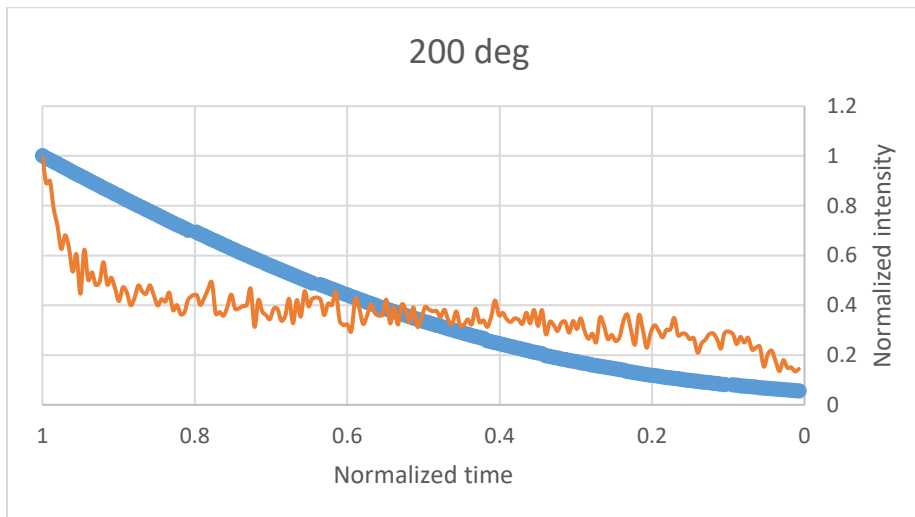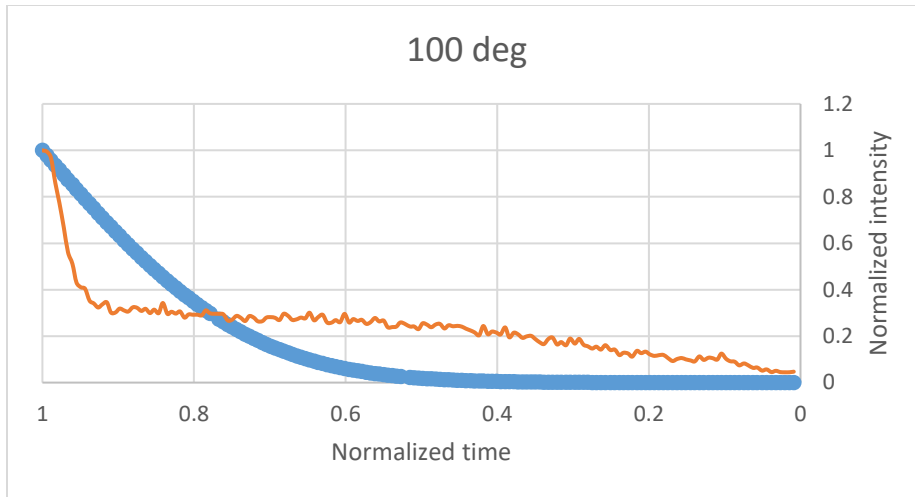
Figure 3.8 Comparison of the experimental SIMS profile (orange line) and CSC wafer model (blue line)

Figure 3.9 shows the plot fits using the CTD wafer model at 23, 50, 100 and 200°C.
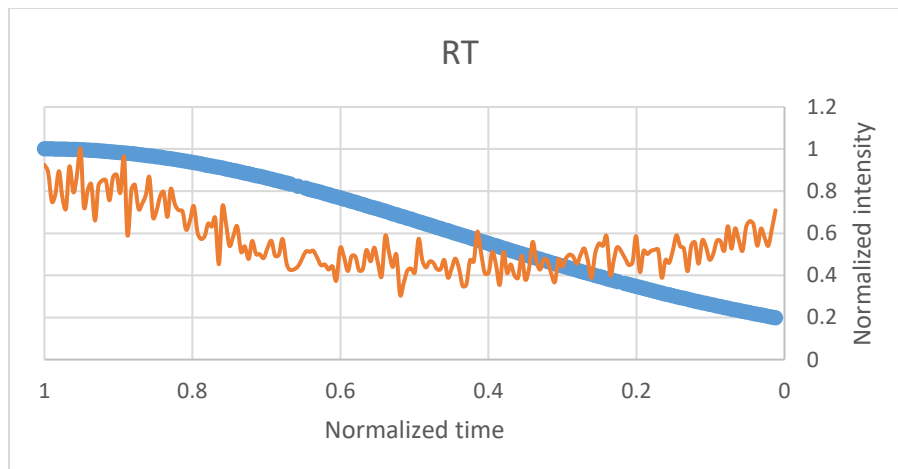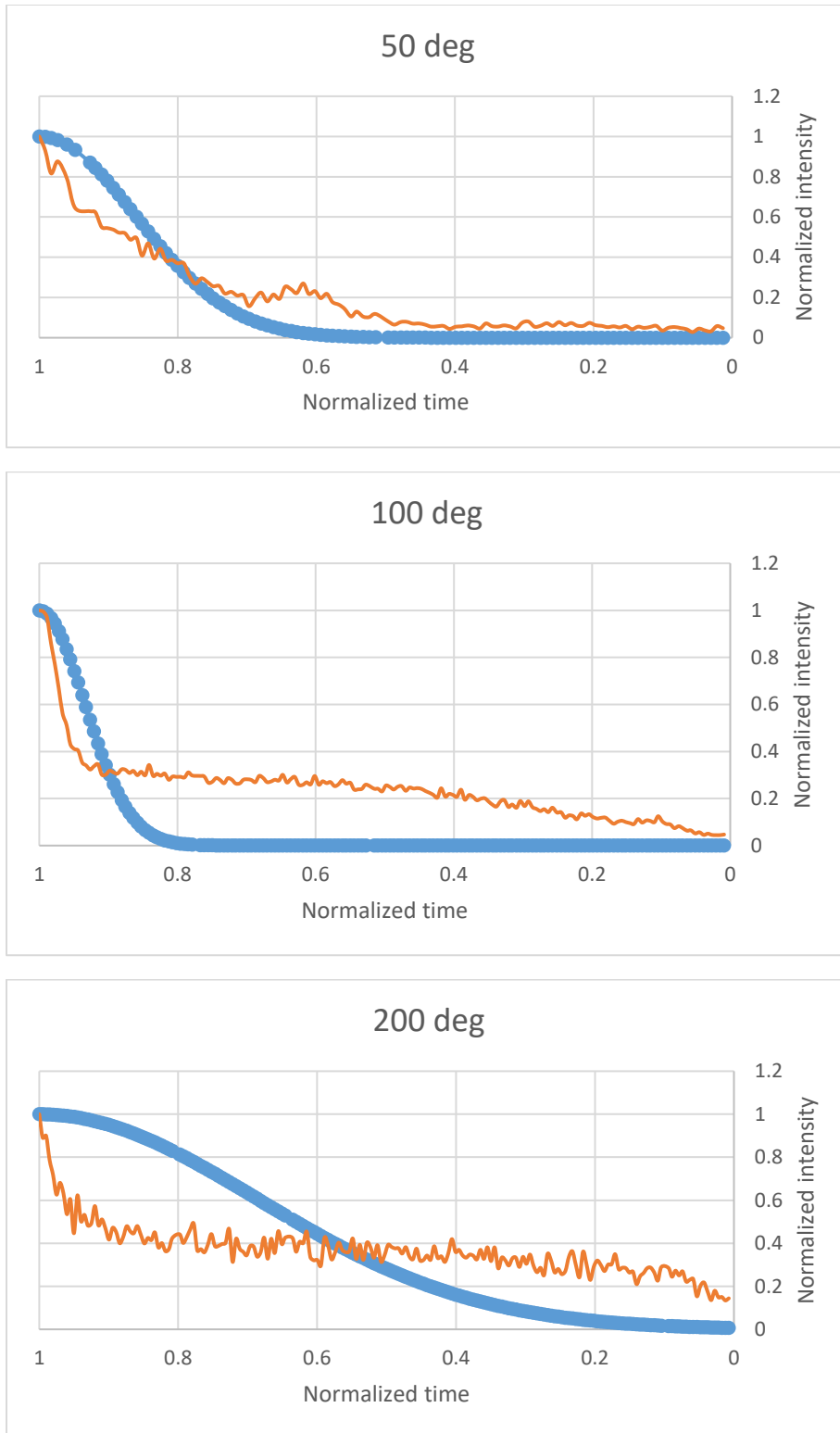
Figure 3.9 Comparison of the experimental SIMS profile (orange line) and CTD wafer model (blue line)

We were only able to fit the SIMS data at 50°C for both diffusion models. The depth profiles at the other temperatures all had different shapes which would indicate a different diffusion mechanism and maybe some other factors such as chemical reactions, an evolving geometry of the Molybdenum film, segregation, etc. The values of the grain boundary diffusivities extracted from both models are reported Table 3.6.

|	Diffusivity (cm^2/s)	
Tss (°C)	CSC	CTD
23	2.35e-13	8.45e-14
50	1.05e-14	3.63e-15
100	1.05e-14	1.00e-15
200	6.68e-14	2.56e-14

Table 3.7. Diffusivity coefficients of potassium into molybdenum as a function of Tss, extracted for two different models.

Just as we did for the sodium diffusion model, we had to modify the existing models to account for any diffusion through the grain. Thus, we used the Solver function find the best fit using four variables, namely: grain diffusivity (D_{grain}), grain boundary diffusivity ($D_{boundary}$), initial grain concentration (C_{grain}) and initial grain boundary concentration ($C_{boundary}$).

Figure 3.10 shows the plot fits using the CSC polycrystalline model at 23, 50, 100 and 200°C.
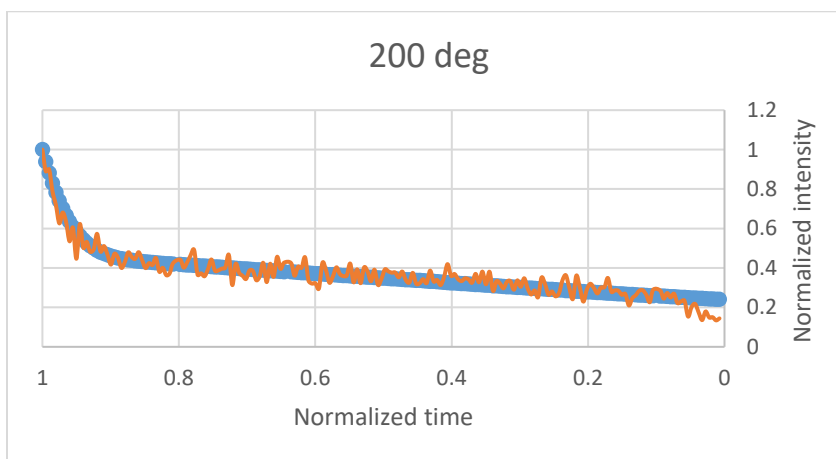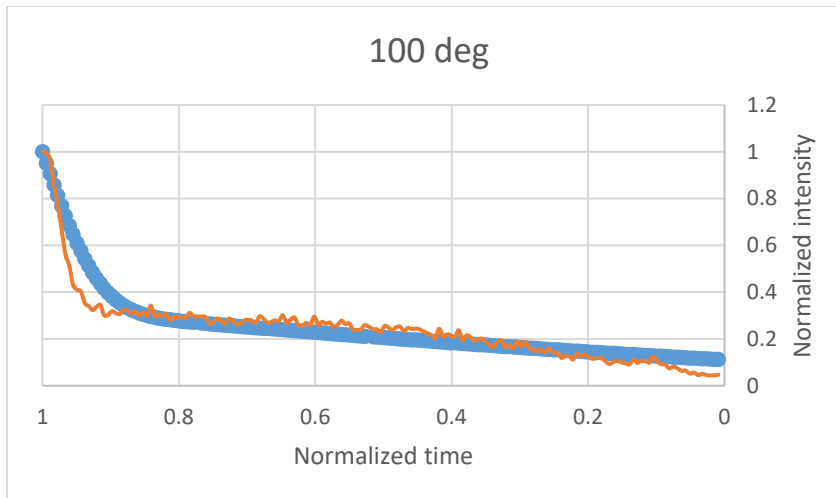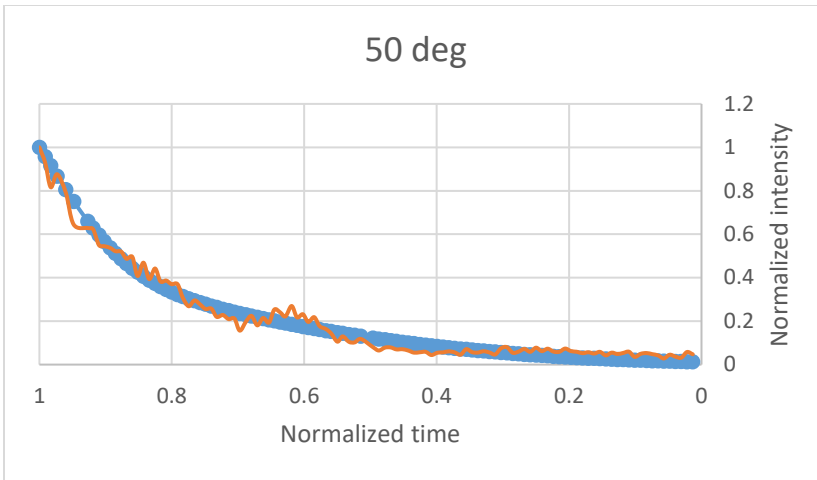
Figure 3.10 Comparison of the experimental SIMS profile (orange line) and CSC polycrystalline model (blue line)

We could fit the data for all temperatures, and the data in Table 3.8 below indicates a type B

diffusion mechanism with some disparity in initial concentration values. 100 and 200ºC

specifically shows more disparity in the initial concentration values.

Tss (ºC)	D_{grain} (cm²/s)	$D_{boundary}$ (cm²/s)	C_{grain} (mol/m³)	$C_{boundary}$ (mol/m³)
23	9.41e-15	1.00e-10	99.89	98.72
50	1.95e-15	3.73e-14	107.88	95.86
100	1.00e-15	2.53e-13	144.80	69.49
200	1.00e-15	5.58e-13	101.58	26.75

Table 3.8. Diffusivity coefficients and concentration values of potassium into molybdenum as a function of Tss

Figure 3.11 shows the plot fits using the CTD polycrystalline diffusion model at 23, 50, 100 and

200ºC.
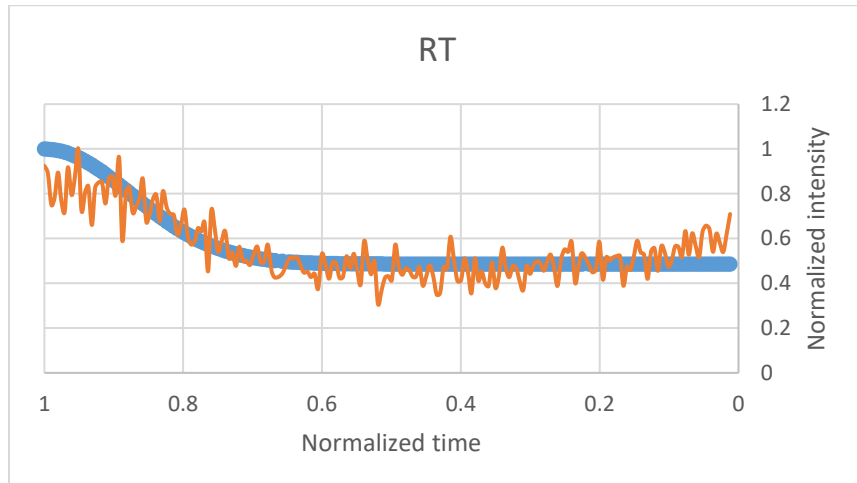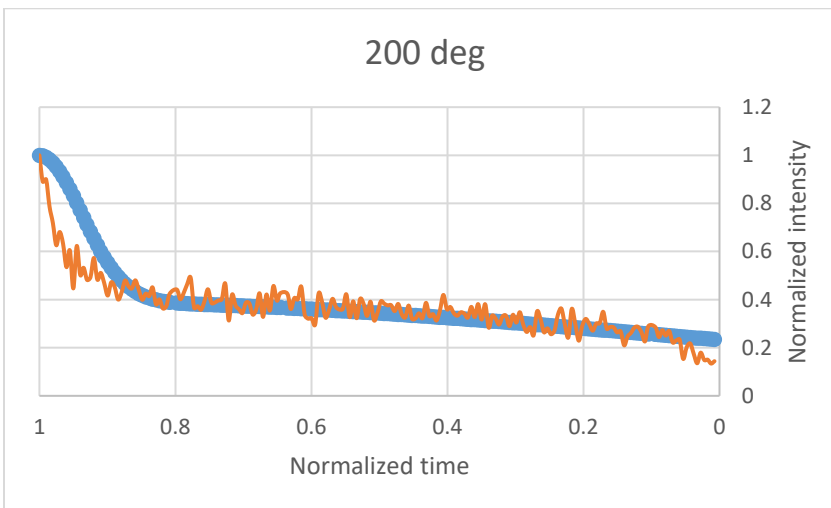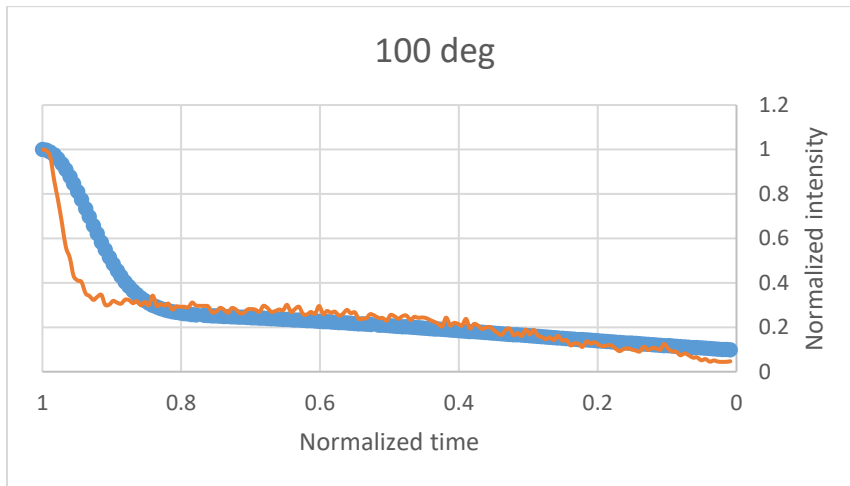
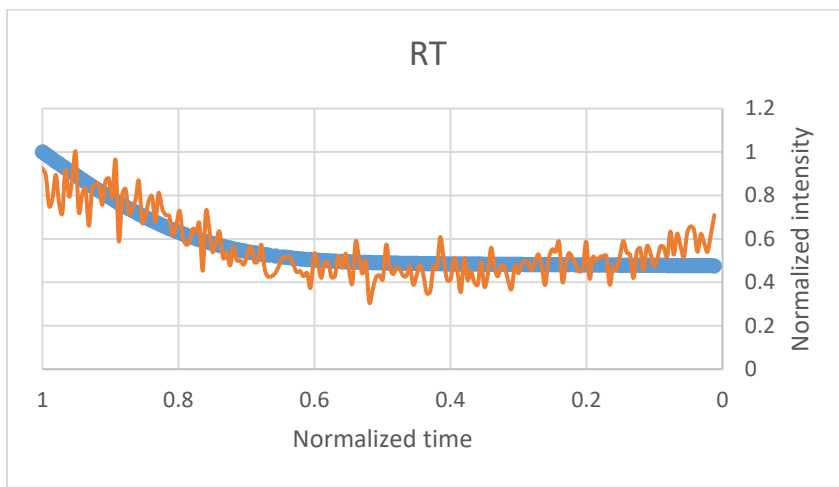Figure 3.11 Comparison of the experimental SIMS profile (orange line) and CTD polycrystalline model (blue line)

We could fit the data for all temperatures, and the data in Table 3.9 below indicates a type B

diffusion mechanism with some disparity in initial concentration values. 100 and 200ºC

specifically shows more disparity in the initial concentration values.

Tss (^{0}C)	D_{grain} (cm^2/s)	$D_{boundary}$ (cm^2/s)	C_{grain} (mol/m^3)	$C_{boundary}$ (mol/m^3)
23	4.38e-15	1.00e-10	84.71	80.35
50	1.00e-15	2.29e-14	22.74	12.34
100	1.00e-15	1.14e-13	65.93	23.99
200	1.00e-15	2.49e-13	145.02	93.52

Table 3.9. Diffusivity coefficients and concentration values of potassium into molybdenum as a function of Tss

We then tried combining the effects of the CSC and CTD polycrystalline models, which are shown

on the plots in Figures 3.12 and 3.13. For the plots in Figure 3.12, we applied CTD to the grain

boundary and CSC to the grain and for the plots in Figure 3.13, we applied CSC to the grain

boundary and CTD to the grain.

RT

50 deg

100 deg
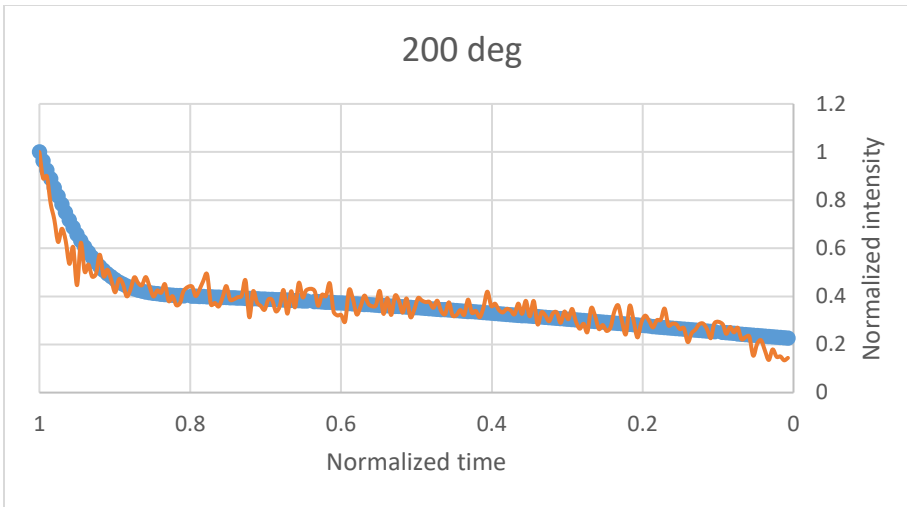
Figure 3.12 Comparison of the experimental SIMS profile (orange line) and the CSC & CTD models (blue line)

We were able to fit the data for all temperatures, and from the data in Table 3.10 below, the

dominant diffusion mechanism at all temperatures seems to be of the type B with some

discrepancy in the initial concentration of the grain and grain boundary.

T_{ss} (^{0}C)	D_{grain} (cm^2/s)	$D_{boundary}$ (cm^2/s)	C_{grain} (mol/m^3)	$C_{boundary}$ (mol/m^3)
23	9.84e-15	1.00e-10	52.40	49.01
50	2.58e-15	2.66e-14	69.88	30.94
100	1.00e-15	9.85e-14	74.08	30.22
200	1.00e-15	2.16e-13	115.04	79.94

Table 3.10. Diffusivity coefficients and concentration values of potassium into molybdenum as a function of Tss

The plots from the second combination of the CSC and CTD diffusion models are shown in

Figure 3.13 below.
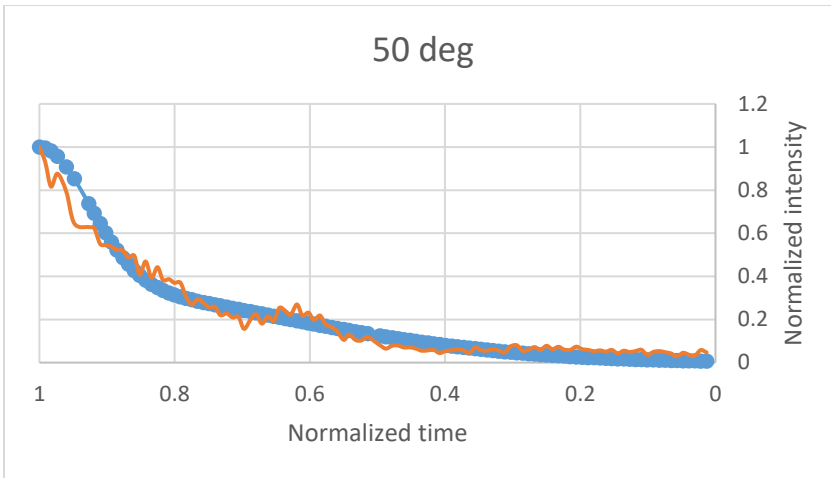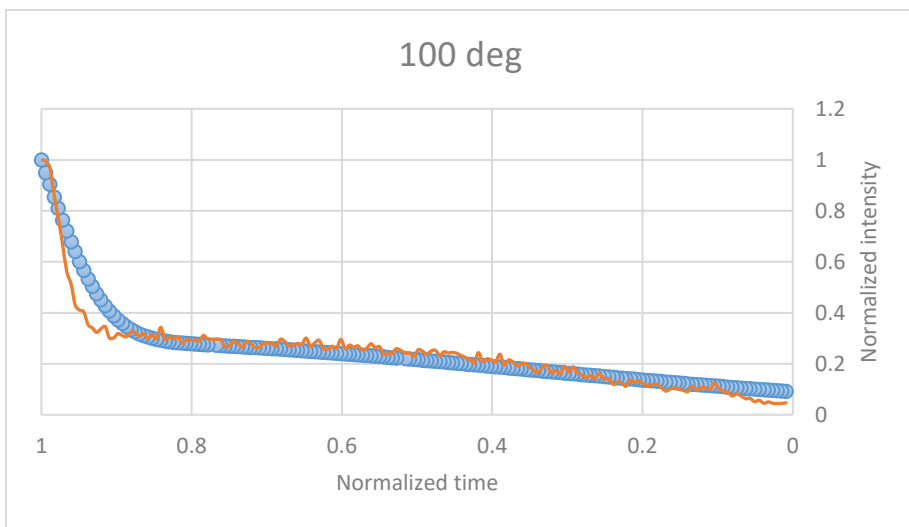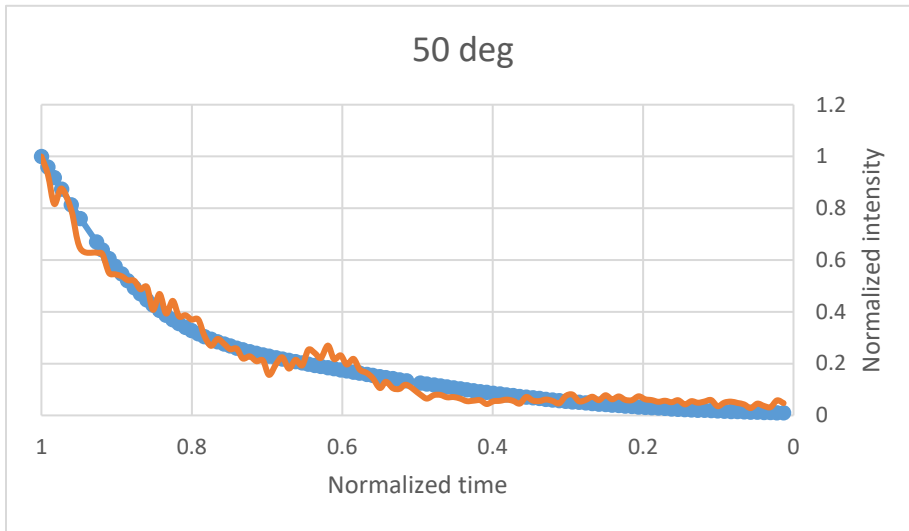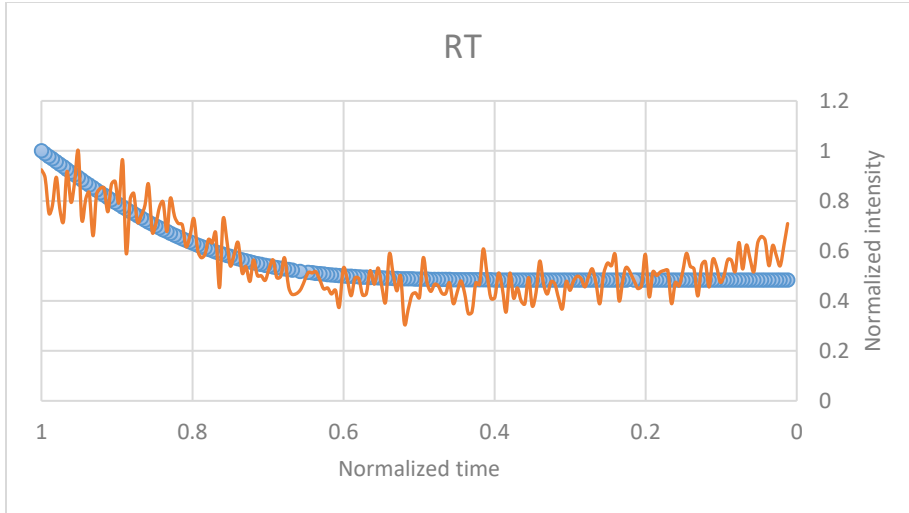
RT

50 deg

100 deg
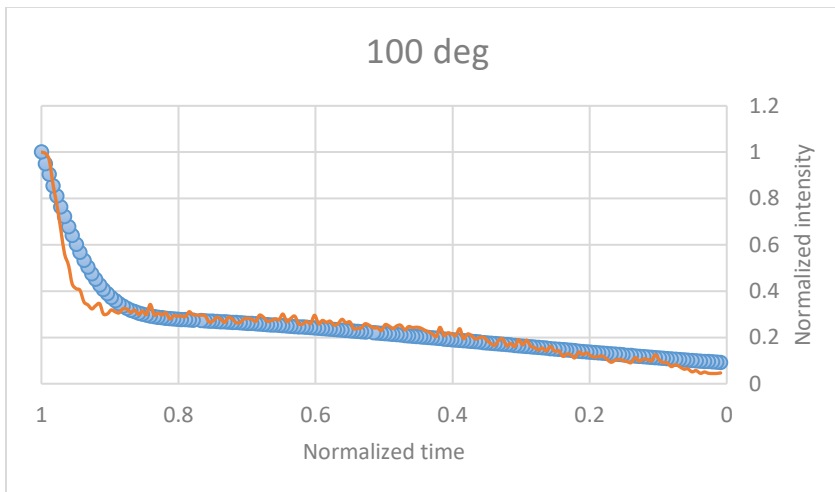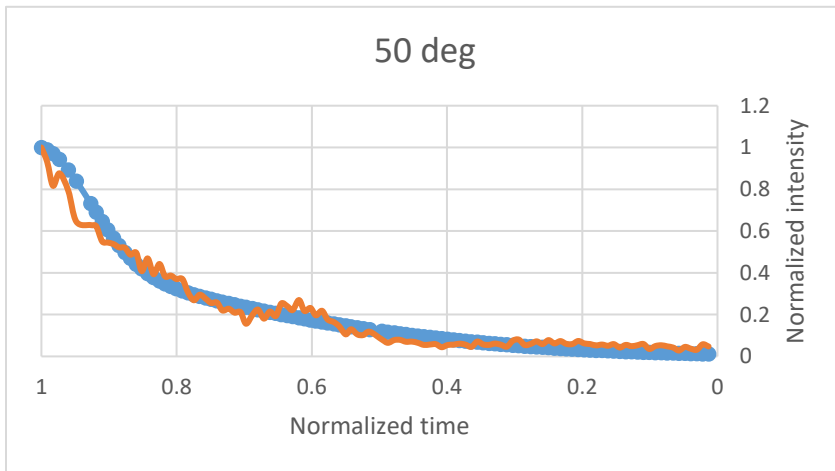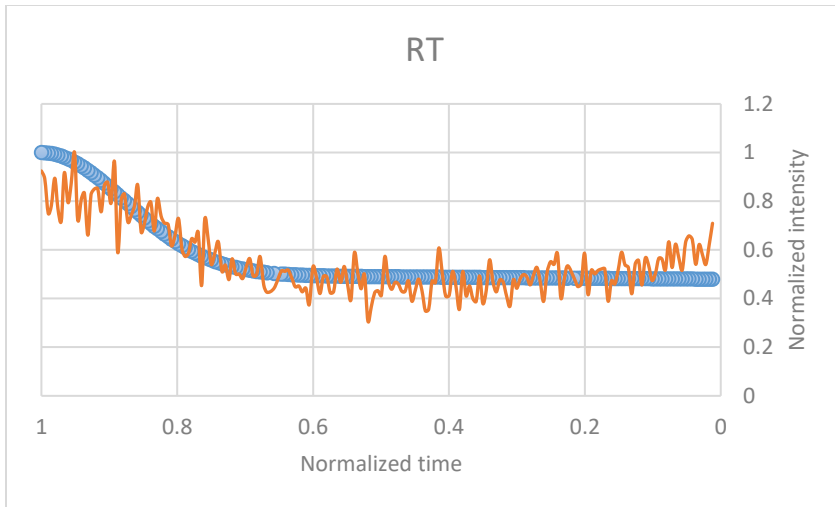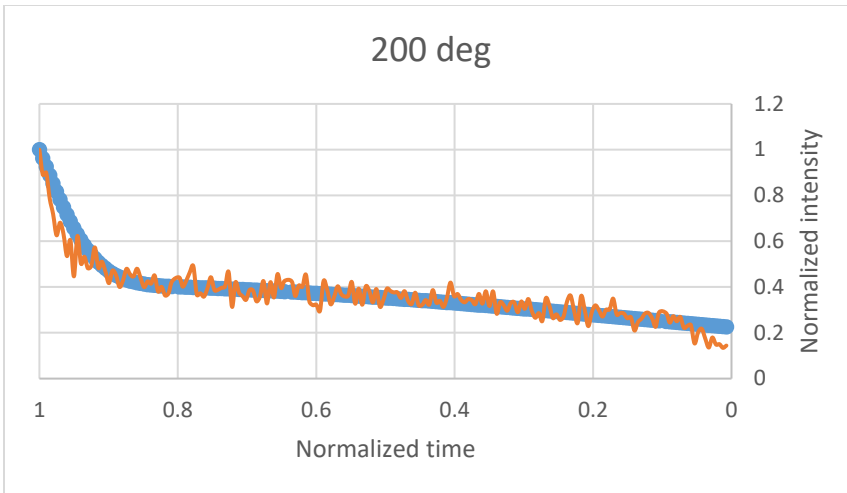
Figure 3.13 Comparison of the experimental SIMS profile (orange line) and the CSC & CTD models (blue line)

We could fit the data for all temperatures, and from the data in Table 3.11 below, the dominant diffusion mechanism at all temperatures also seems to be of the type B with some discrepancy in the initial concentration of the grain and grain boundary. A large disparity in initial concentration is noticed at 100°C.

Tss (^{0}C)	D_{grain} (cm^2/s)	$D_{boundary}$ (cm^2/s)	C_{grain} (mol/m^3)	$C_{boundary}$ (mol/m^3)
23	4.23e-15	1.00e-10	68.89	68.96
50	1.00e-15	3.62e-14	69.97	64.49
100	1.00e-15	9.84e-14	196.95	80.39
200	1.00e-15	2.16e-13	93.81	65.19

Table 3.11. Diffusivity coefficients and concentration values of sodium into molybdenum as a function of Tss

3.2.3   SUMMARY

Throughout this diffusion study using Excel, 100 and 200°C were notoriously difficult to fit. We were only able to fit the SIMS data at these temperatures because we varied the initial

surface concentration of the grain and grain boundary (most times with huge discrepancies), which physically does not make much sense because the initial surface concentration of sodium/potassium coming from the source should be fairly constant. It should not be selectively higher on either the grain or grain boundary until the diffusion process starts. Even though the purpose of introducing a varying initial concentration was to obtain a fit for the SIMS data, the need for a large discrepancy in the initial concentration values might signify other underlying factors affecting the diffusion process such as an evolving change in geometry of the molybdenum film as the impurities diffuse through it or some chemical reactions which are not being considered in this study. Thus, it is difficult to determine the accuracy of the obtained diffusivity values because the geometry of the grain and grain boundary was not considered in the basic models discussed in this section.

A much more comprehensive model can be achieved using COMSOL which numerically solves Fick's Law and allows one to fully consider the geometry of the grain and grain boundary as well as any chemical reactions that might be taking place in the film during film growth

CHAPTER 4

4 MODELING OF IMPURITY DIFFUSION USING COMSOL

4.1 INTRODUCTION TO COMSOL

COMSOL Multiphysics® is a general-purpose software platform, based on advanced numerical methods, for modeling and simulating physics-based problems. It allows users to simulate and solve problems in fields or domains such as fluid flow, heat transfer, mechanics, semiconductors and many more. Screen shots of the COMSOL Desktop environment are shown in Figures 4.1 and 4.2 below. The two main parts of the COMSOL Desktop environment are the Model Builder and Application Builder. The Model Builder helps you define your model, provides a solution path, an analysis of results and creates reports. The model tree contains settings for geometry, physics, boundary conditions, studies, solvers, mesh, etc. The Application Builder helps you to create an easy to use application.
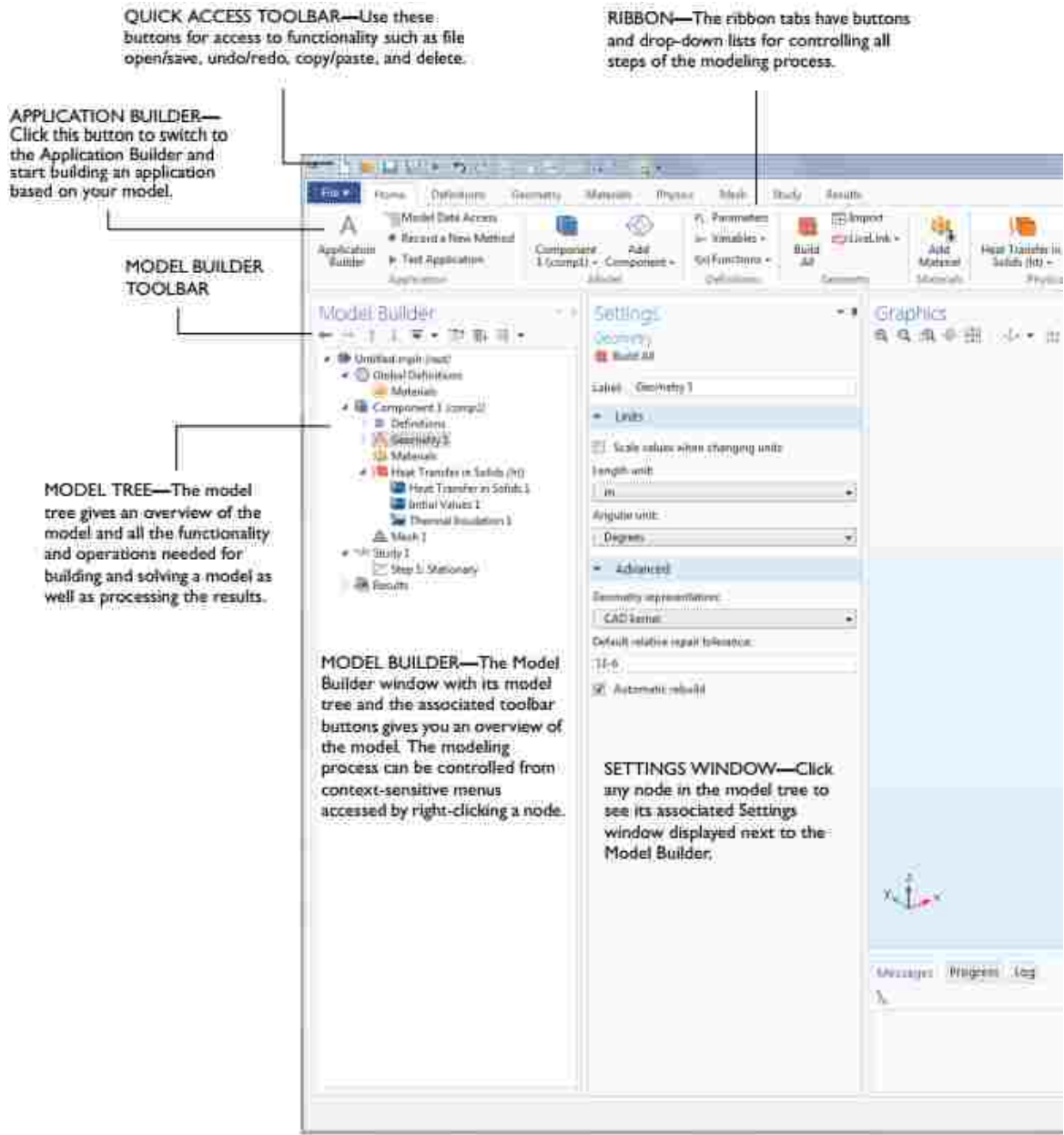
Figure 4.1 COMSOL desktop environment [10]

GRAPHICS WINDOW TOOLBAR
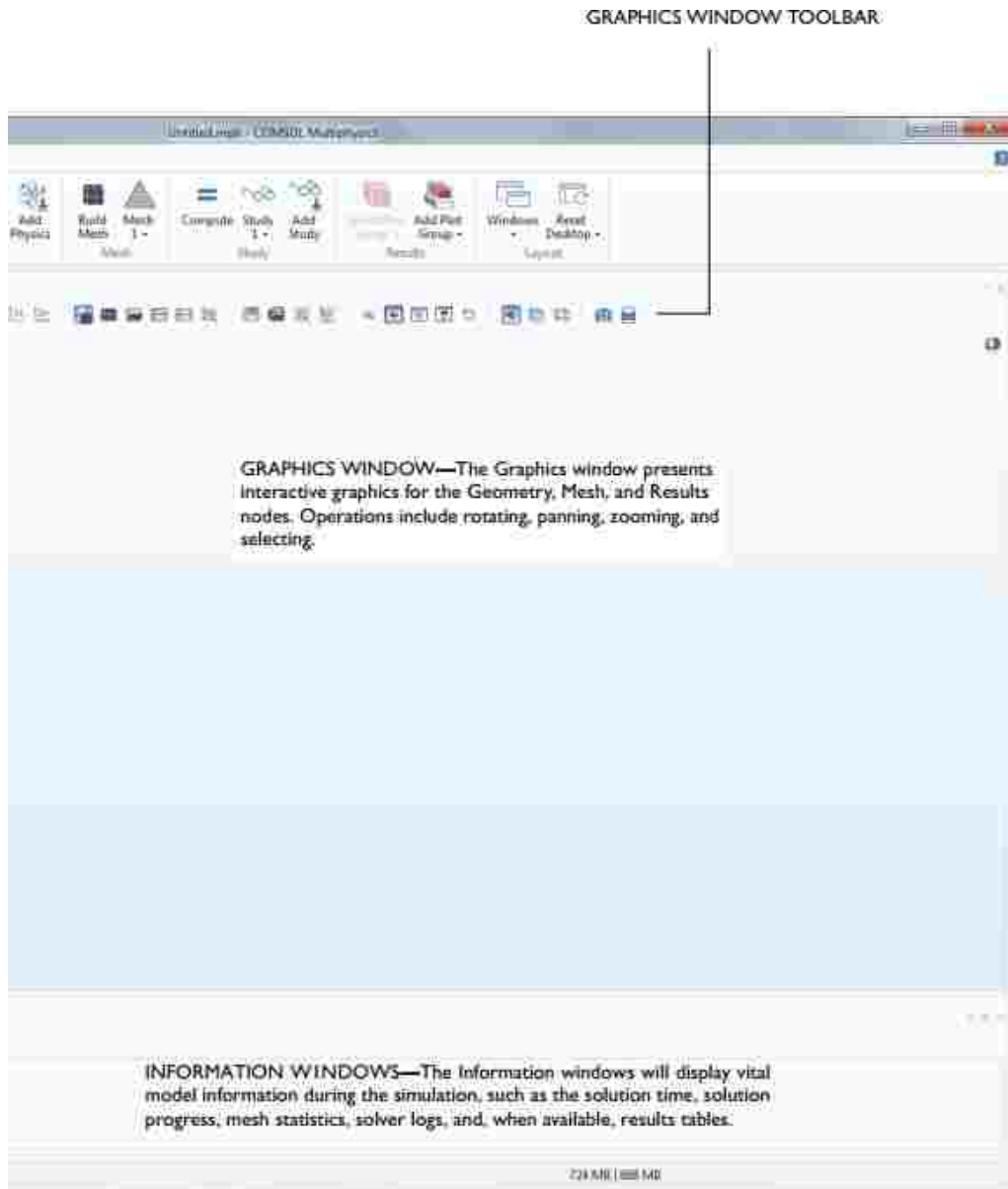
Figure 4.2 COMSOL graphics window [10]

Suppose you are given a problem to solve using COMSOL, the following would be your basic solution steps. First, you would need to create a new model using either of two ways (Figure 4.3): the Model Wizard or the Blank Model.

Figure 4.3 Creating a new model [10]

The Model Wizard helps you set up the space dimension, physics and study type (Figure 4.4).

Figure 4.4a Model Wizard – Space Dimension [10]
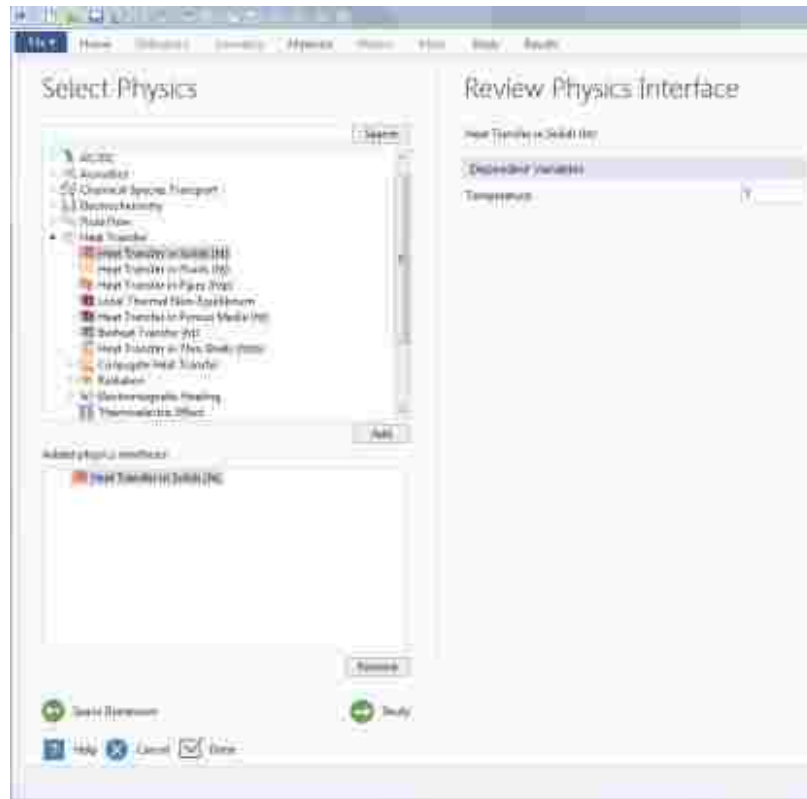
Figure 4.4b Model Wizard – Physics selection [10]

Figure 4.4c Model Wizard – Study selection[10]

The Model Wizard automatically creates a Component node (Figure 4.5) and a Study node after specifying the type of physics you are simulating and the type of Study you plan on using. These nodes help you develop your model.
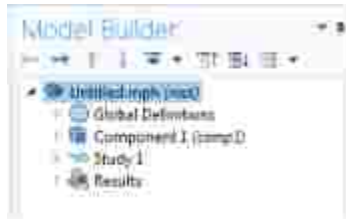
Figure 4.5 Component and Study Nodes [10]

The Blank Model would open the COMSOL user interface without any Component or Study. Then, you would use the Model Builder to build your model (Figure 4.6). The model tree contains a root node which is initially labelled 'Untitled.mph', a Global Definitions node and a Results node.
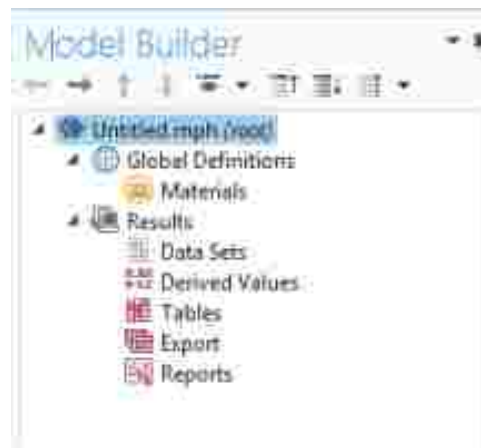
Figure 4.6 Model Builder [10]

The Global Definitions node allows you to define your parameters, functions, variables and couplings. It contains the Materials subnode which by default stores material properties that can be referenced in the Component nodes of the model. The Results node provides the solution to the simulated model. It also provides tools for further data processing. The Results node initially has 5 subnodes: data sets, derived values, tables, export and reports. Data sets contains a list of solutions. Derived values defined values to be derived from the solution. Tables creates a table for the derived values or results subnode. Numerical data and images can be exported to other files using the export subnode. The reports subnode creates custom reports about the model. Plot group which helps to define graphs or plots can also be added as a subnode.

COMSOL allows you to define global parameters and variables (Figure 4.7). Global parameters are user-defined constant values that can be used at any time during the study. They can be used to specify mesh element size and define parametric sweeps. Variables, on the other hand, can be defined in the Global Definitions node or in the Definitions subnode of a Component node.
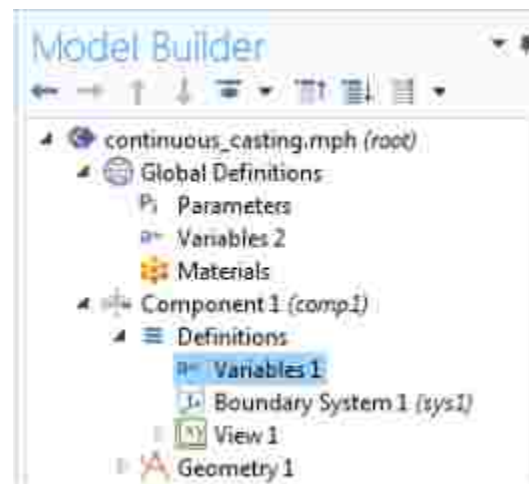
Figure 4.7 Parameters and Variables Definition [10]

4.2   SINGLE LAYER DIFFUSION STUDY

An important observation that was not considered in the diffusion models discussed earlier is that the sputtering beam during SIMS data acquisition collects contributions from both grain and grain boundary. This observation is valid because depending on the deposition temperature, the proportion of grains and grain boundaries is very different. The theoretical diffusion models presented are not comprehensive enough to address both the contribution of grain and grain boundary diffusion and they do not address the issue of an evolving grain structure which leads to having different parameters for different types of grain structures. These problems need to be addressed in a better, more advanced model.

This advanced model can be achieved using COMSOL because it has the capability of solving Fick's equations in real time (diffusivity is given as input) and outputting a concentration profile that can be compared to our experimental SIMS data. COMSOL provides a realistic structural model that can be used for the polycrystalline molybdenum layer.

We created three molybdenum models in COMSOL for both the sodium and potassium diffusion studies. These models include: a wafer model, a polycrystalline model and an approximation of a molybdenum TEM image (Figure 4.8). We performed TEM characterization on one of our CIGS solar cell samples in the past. TEM is required in this work to obtain the grain boundary width needed to develop the models outlined above. The 'white' part of the image is the molybdenum layer with the other dark parts on either side of it being the SLG substrate and the CIGS absorber layer.
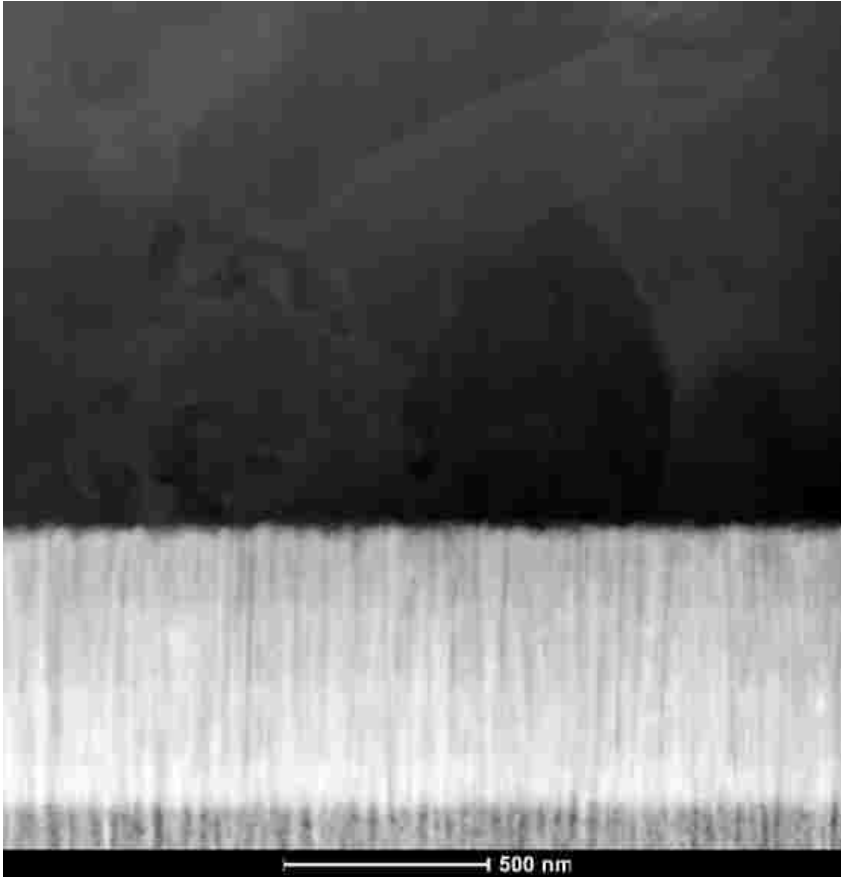
Figure 4.8 TEM image of CIGS solar cell sample

The wafer model, shown in Figure 4.9, is just a slab of molybdenum (no grain or grain boundary) with a varying thickness per Table 3.1 and a constant width of 100 nm and a constant initial concentration of 100 mol/m^3. Figure 4.10 shows the polycrystalline model, which consists of one grain and one grain boundary. The grain width is 30 nm while the grain boundary width is 3 nm. The thickness of the molybdenum layer is varied as per Table 3.1. Finally, we approximated a TEM image of a molybdenum layer using rectangles as shown in Figure 4.11. The grain width is between 30 and 40 nm while the grain boundary width is between 3 and 4 nm. Again, the thickness of the molybdenum layer is varied as per Table 3.1.

Figure 4.9 Wafer Model

Figure 4.10 Polycrystalline Model
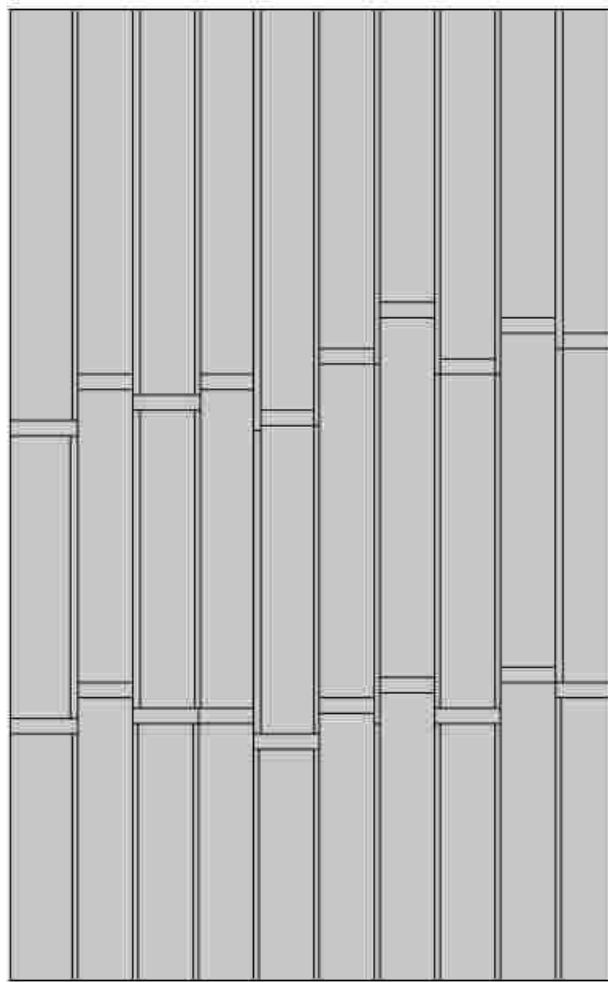
Figure 4.11 TEM Approximation Model

We simulated these models, normalized the obtained concentration profiles from COMSOL and tried to fit the normalized SIMS data with the concentration profiles. A MATLAB script was written to take care of the normalization of the COMSOL concentration profile and the actual fitting of the experimental SIMS data. The diffusion coefficient was the only value that was varied at each temperature and for each model to fit the SIMS data. The initial concentration was kept at

a constant value of 100 mol/m^3 throughout the entire COMSOL study. After each simulation, we would look at the fit and subsequently adjust the diffusivity value until we obtained a good fit. We would then examine the final diffusivity value to make sure it was realistic or feasible.

4.2.1 SODIUM DIFFUSION STUDY

We simulated the diffusion of sodium through the molybdenum film using the three models described in the above section. Figure 4.12 shows the plot fits for the experimental SIMS data using the wafer model.

50 deg

100 deg
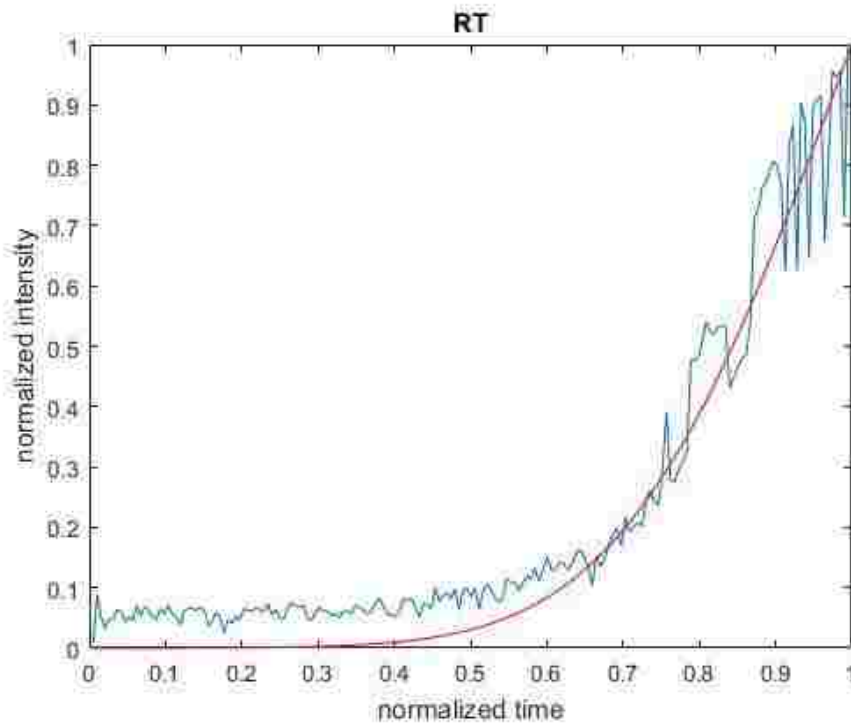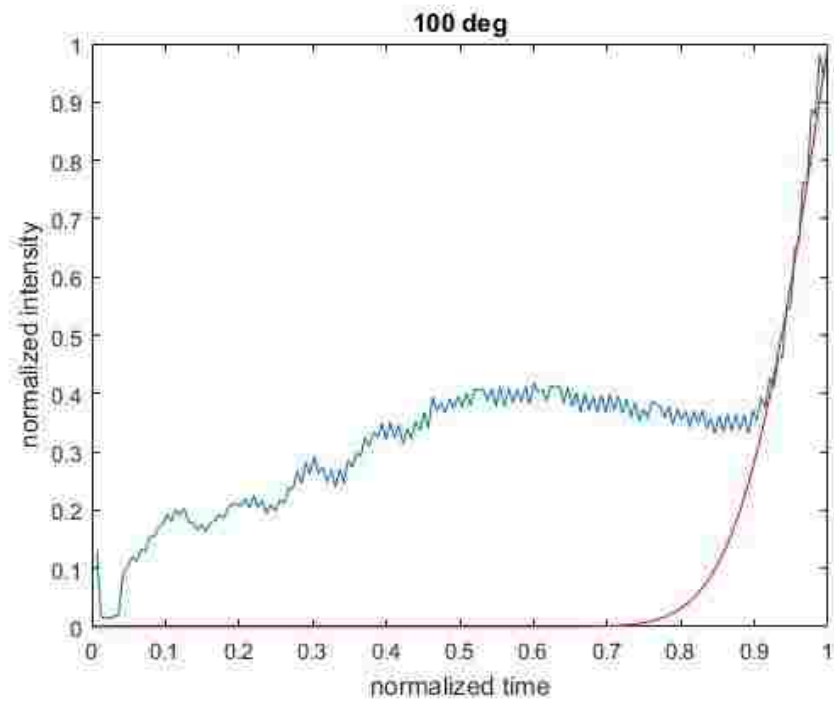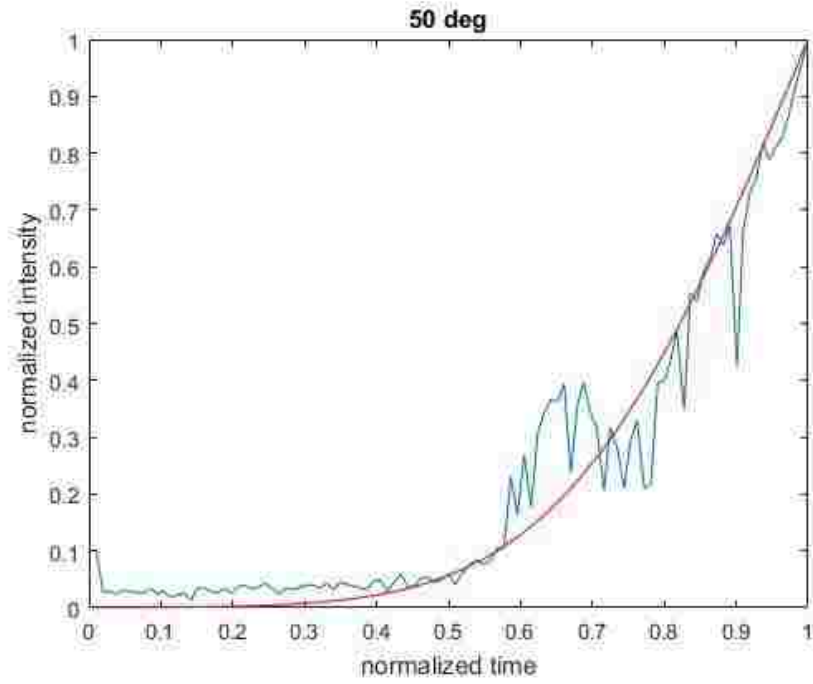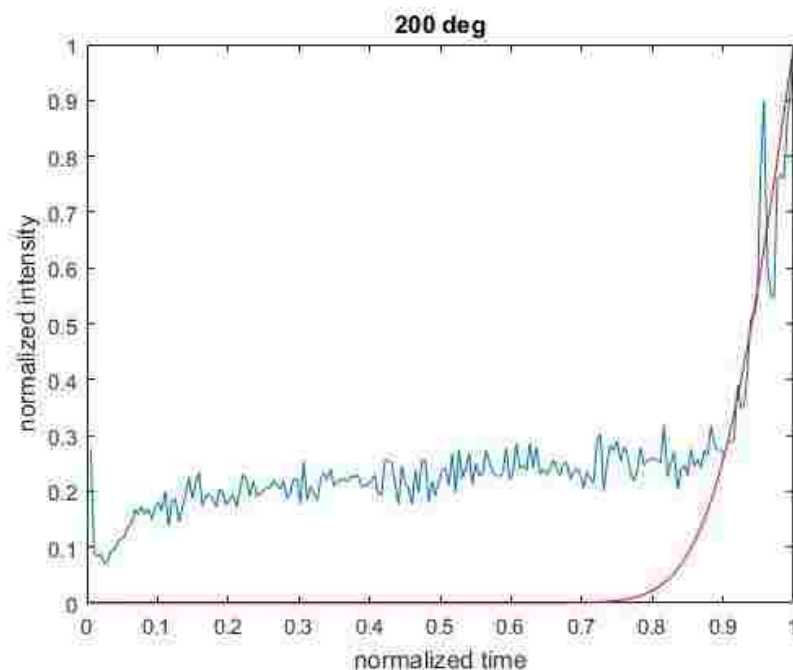
Figure 4.12 Comparison of the experimental SIMS profile (blue line) and the COMSOL wafer model (red line)

As can be seen from the plots, we could not quite obtain a good fit for the 100 and 200°C data. The diffusivity values obtained for this model are given in Table 4.1.

Tss (°C)	Diffusivity (cm²/s)
23	1.5e-14
50	1.3e-14
100	2.0e-15
200	2.0e-15

Table 4.1. Diffusivity coefficients of sodium into molybdenum as a function of Tss, extracted for COMSOL wafer model.

These values, while realistic, do not provide much insight as to why we were unable to properly fit the 100 and 200°C data. A closer look at the original SIMS data shows that the sodium level

rises when Tss is higher than room temperature and eventually reaches its peak at Tss = 100°C, but then it starts to decrease as the Tss is increased beyond 100°C. Thus, there might be some saturation of the sodium impurity at 100°C that subsequently affects its diffusion process at higher temperatures.

Figure 4.13 shows the plot fits for the experimental SIMS data using the polycrystalline model.

50 deg

100 deg
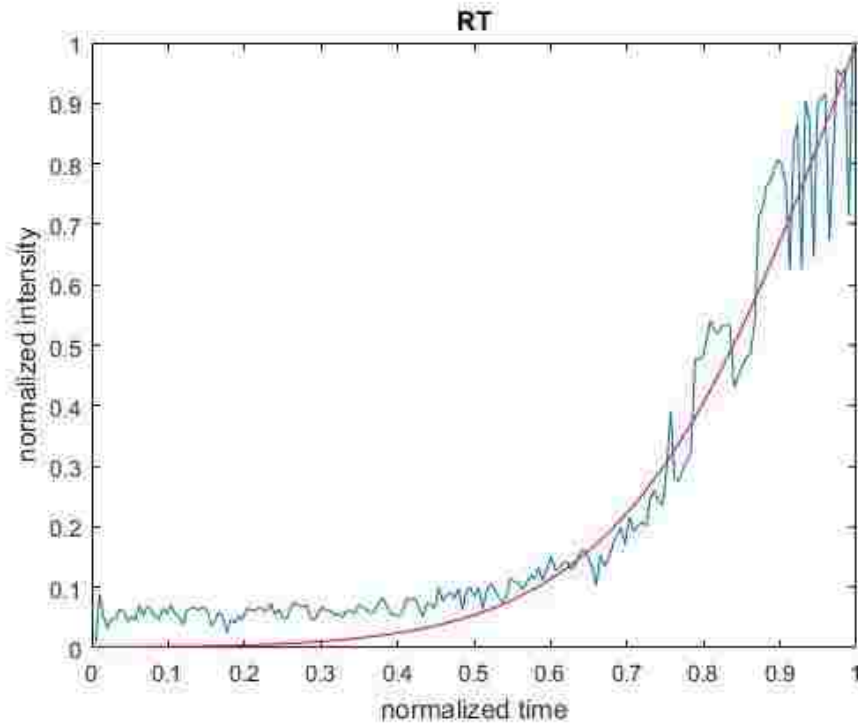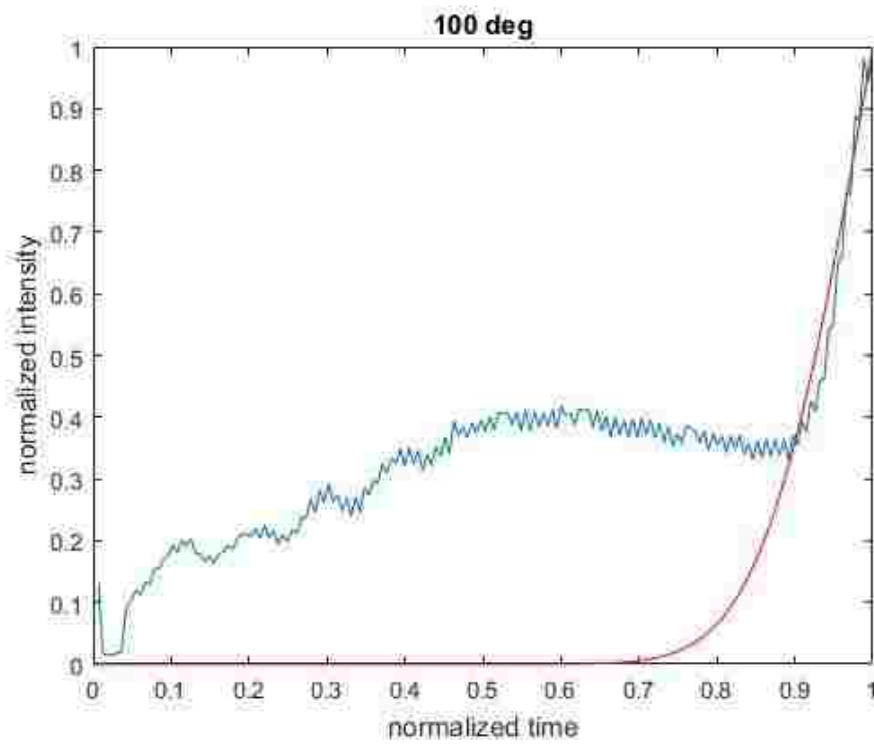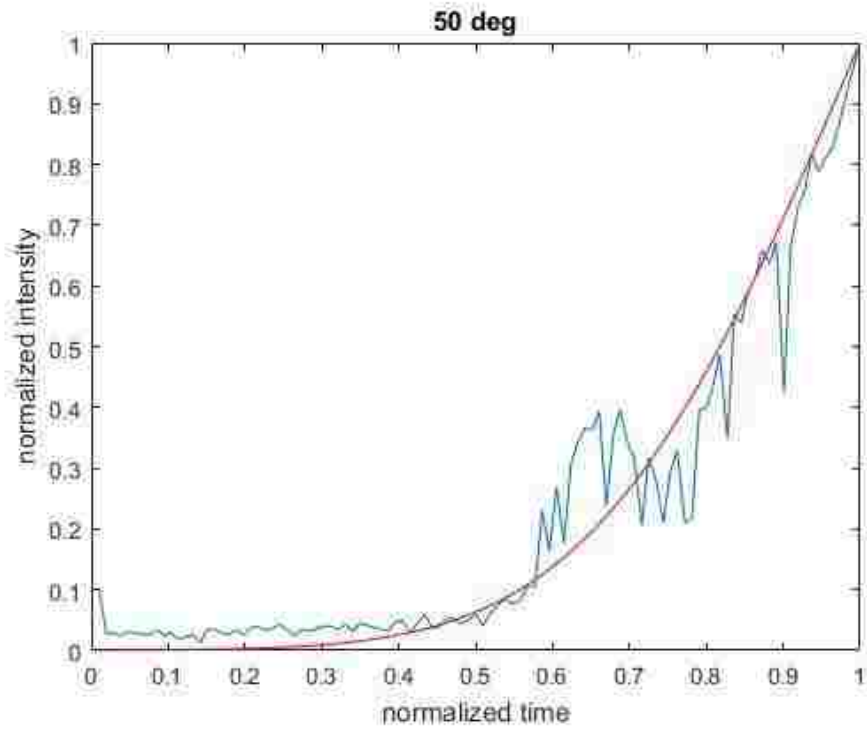
Figure 4.13 Comparison of the experimental SIMS profile (blue line) and COMSOL polycrystalline model (red line)

Again, we could not obtain a good fit for the 100 and 200°C data, which might be due to
saturation of sodium at 100°C. The diffusivity values obtained for the grain and grain boundary
are given in Table 4.2. One can notice that the diffusivity for the grain boundary is always higher
than for the grain, which makes sense physically.

Tss (^{0}C)	$D_{boundary}$ (cm^2/s)	D_{grain} (cm^2/s)
23	5.0e-13	1.0e-14
50	5.0e-14	4.0e-14
100	1.0e-14	8.0e-15
200	1.0e-14	5.0e-15

Table 4.2. Diffusivity coefficients of sodium into molybdenum as a function of Tss, extracted for COMSOL
polycrystalline model.

Finally, we simulated the TEM approximation model, and the plot fits obtained from this model

are shown in Figure 4.14.

Figure 4.14 Comparison of the experimental SIMS profile (blue line) and the COMSOL TEM approximation model (red line)

We could not obtain a good fit for the 100 and 200℃ data, which might be due to saturation of sodium at 100°C. The diffusivity values obtained for the grain and grain boundary are given in Table 4.2. Here again, the values for the diffusivity for the grain boundary are higher than for the grain, which makes sense physically.

Tss (^{0}C)	$D_{boundary}$ (cm^2/s)	D_{grain} (cm^2/s)
23	1.5e-13	8.0e-15
50	4.0e-14	7.0e-15
100	1.0e-14	1.0e-15
200	1.0e-14	1.0e-15

Table 4.3. Diffusivity coefficients of sodium into molybdenum as a function of Tss, extracted for COMSOL TEM approximation model.

4.2.2   POTASSIUM DIFFUSION STUDY

We also simulated the diffusion of potassium through the molybdenum film using the wafer, polycrystalline and TEM approximation models. Figure 4.15 shows that the plot fits for the experimental SIMS data using the wafer model.
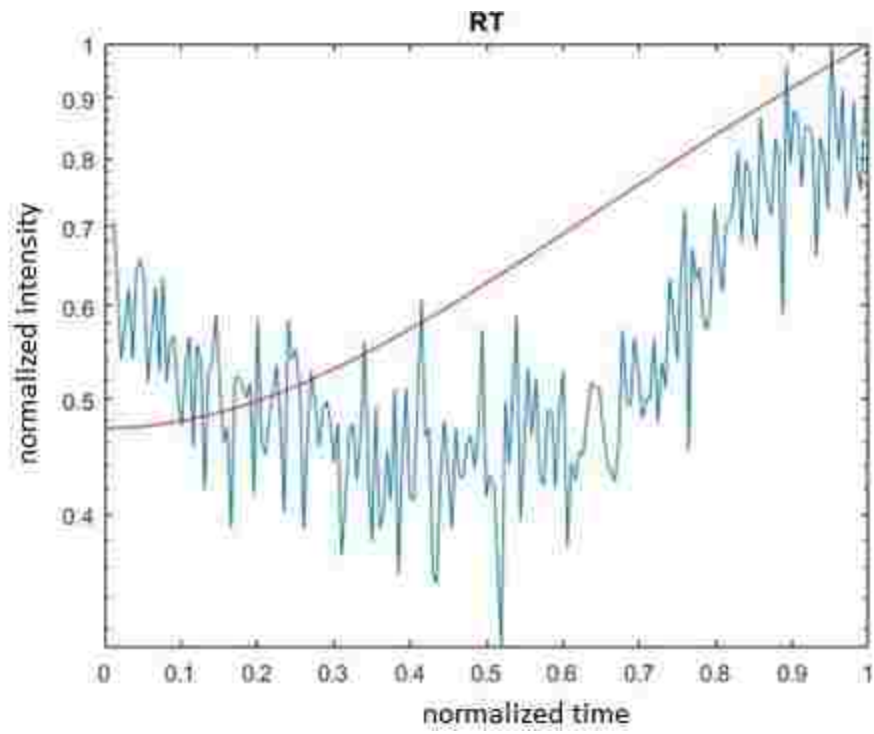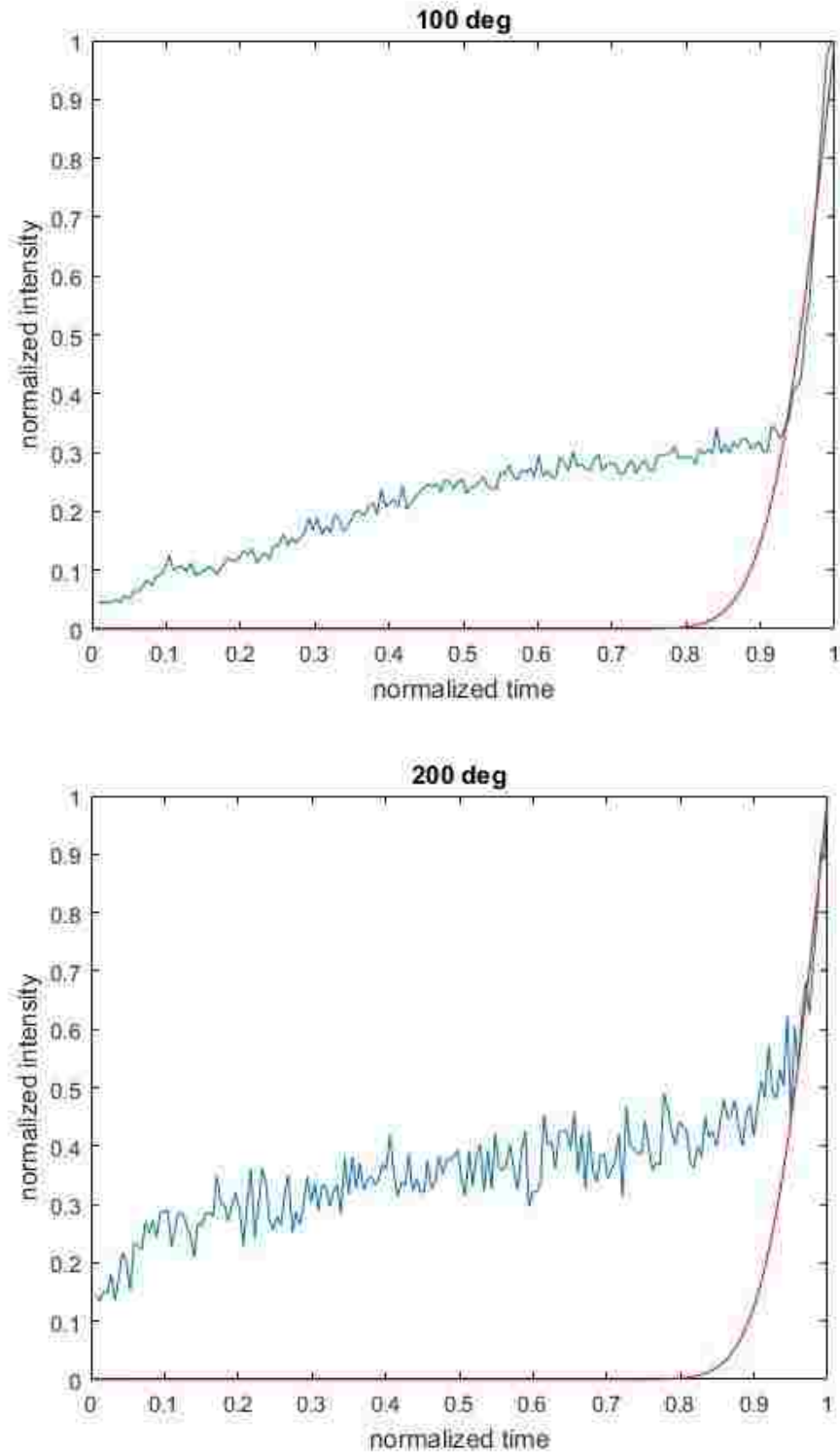
Figure 4.15 Comparison of the experimental SIMS profile (blue line) and COMSOL wafer model (red line) for potassium

We were unable to obtain a good fit for 100 and 200ºC. A closer look at the potassium depth profile highlights a potential saturation problem, similar to that seen in the sodium data. The potassium level rises when Tss is higher than room temperature and eventually reaches its peak at Tss = 100°C, but then it starts to decrease as the Tss is increased beyond 100°C. We also could not quite get a very good fit for the RT data. The diffusivity values obtained for this model are given in Table 4.4.

Tss (ºC)	Diffusivity (cm²/s)
23	2.0e-13
50	8.0e-15
100	1.1e-15
200	1.1e-15

Table 4.4. Diffusivity coefficients of potassium into molybdenum as a function of Tss, extracted for COMSOL wafer model.

Figure 4.16 shows the plot fits for the experimental SIMS data using the polycrystalline model.
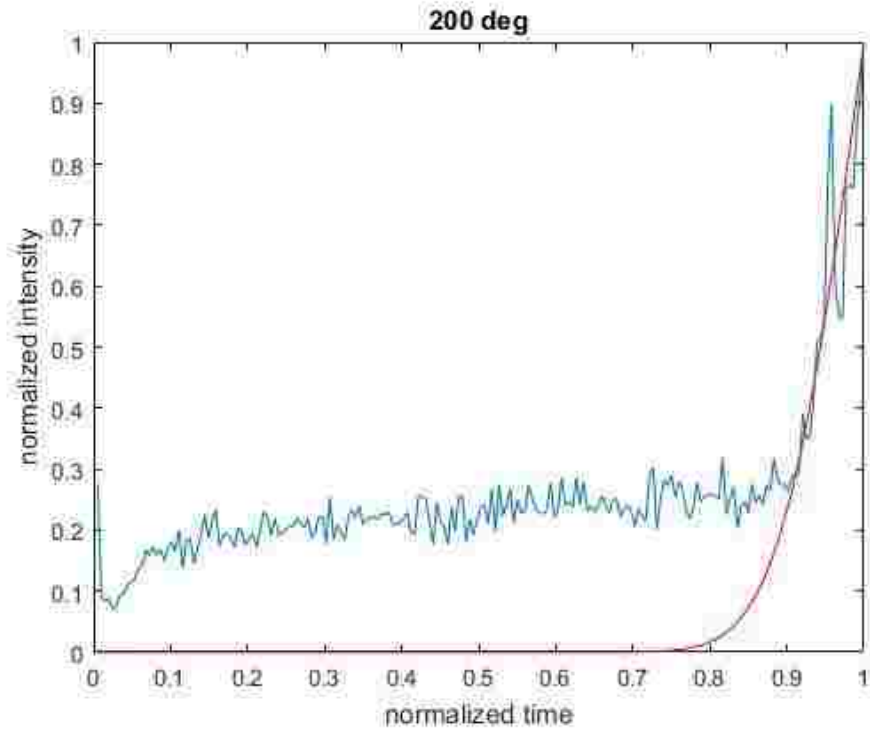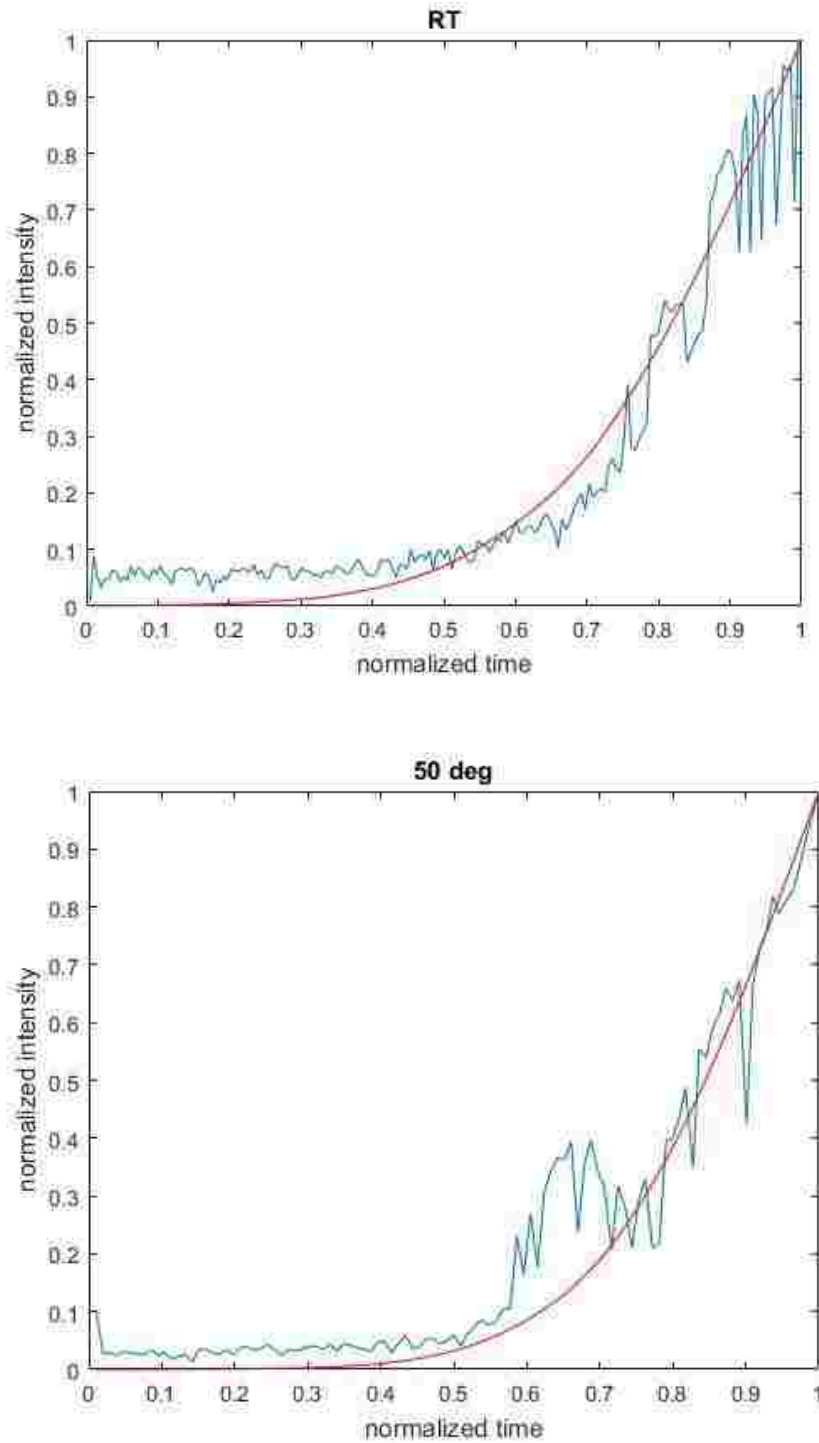
50 deg

100 deg
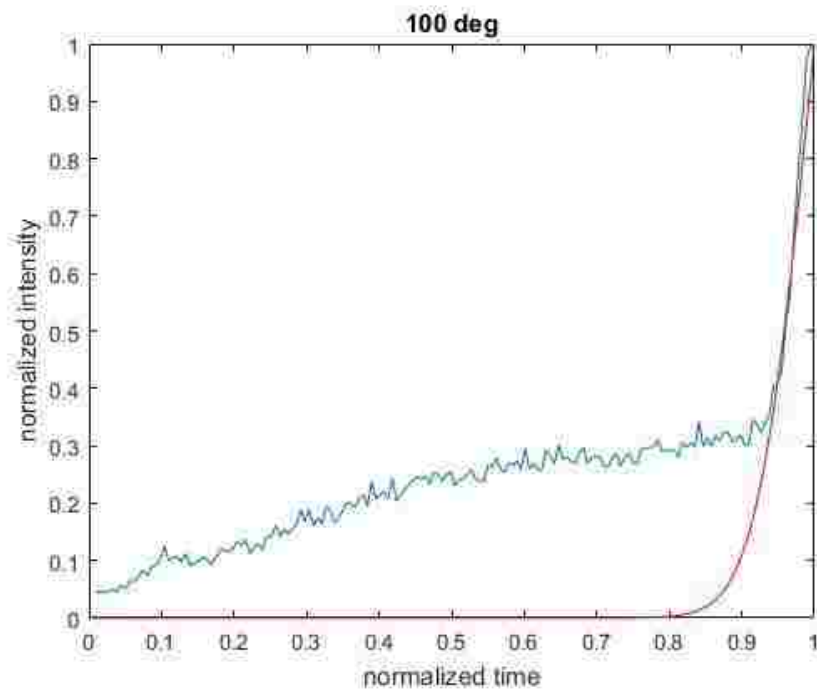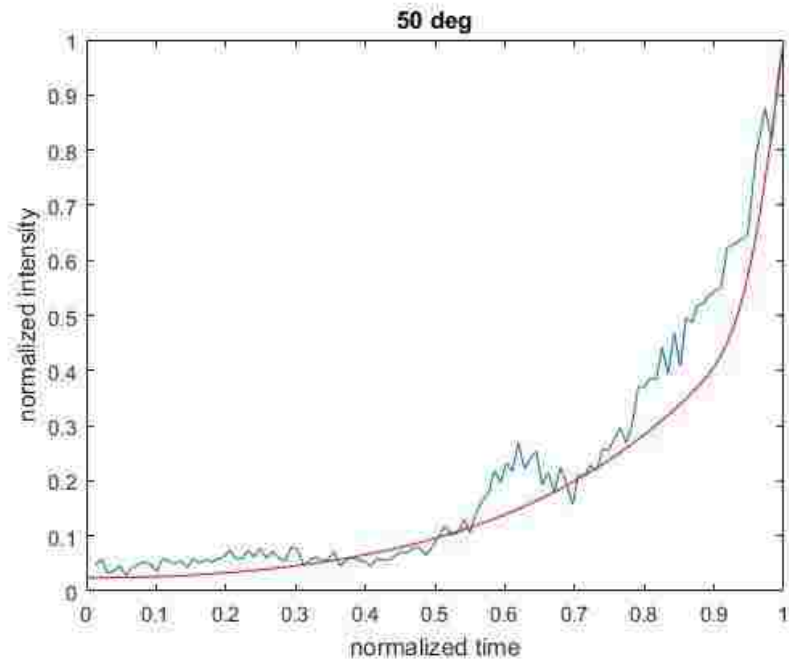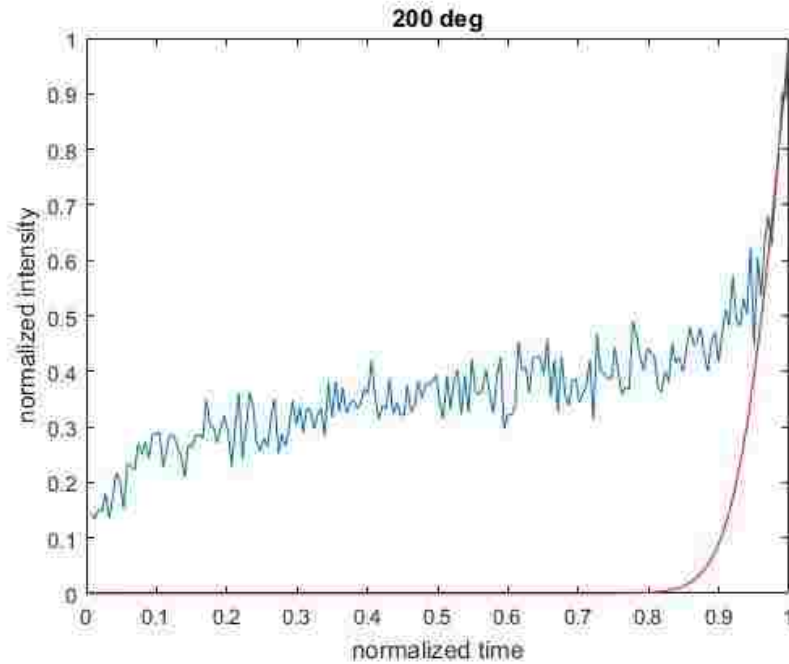
Figure 4.16 Comparison of the experimental SIMS profile (blue line) and COMSOL polycrystalline model (red line) for potassium

We also could not obtain a good fit for the 100 and 200°C data, which might be due to saturation of sodium at 100°C. The fit for RT data was not very good as well. The diffusivity values obtained for the grain and grain boundary are given in Table 4.5. Here again, the diffusivity in the grain boundary is higher than in the grain, as expected.

Tss (^{0}C)	D$_{boundary}$ (cm^2/s)	D$_{grain}$ (cm^2/s)
23	5.0e-10	9.5e-16
50	5.0e-13	1.0e-15
100	1.0e-14	2.0e-15
200	1.0e-14	2.0e-15

Table 4.5. Diffusivity coefficients of potassium into molybdenum as a function of Tss, extracted for COMSOL polycrystalline model.

Finally, we simulated the TEM approximation model, and the plot fits obtained from this model are shown in Figure 4.17.
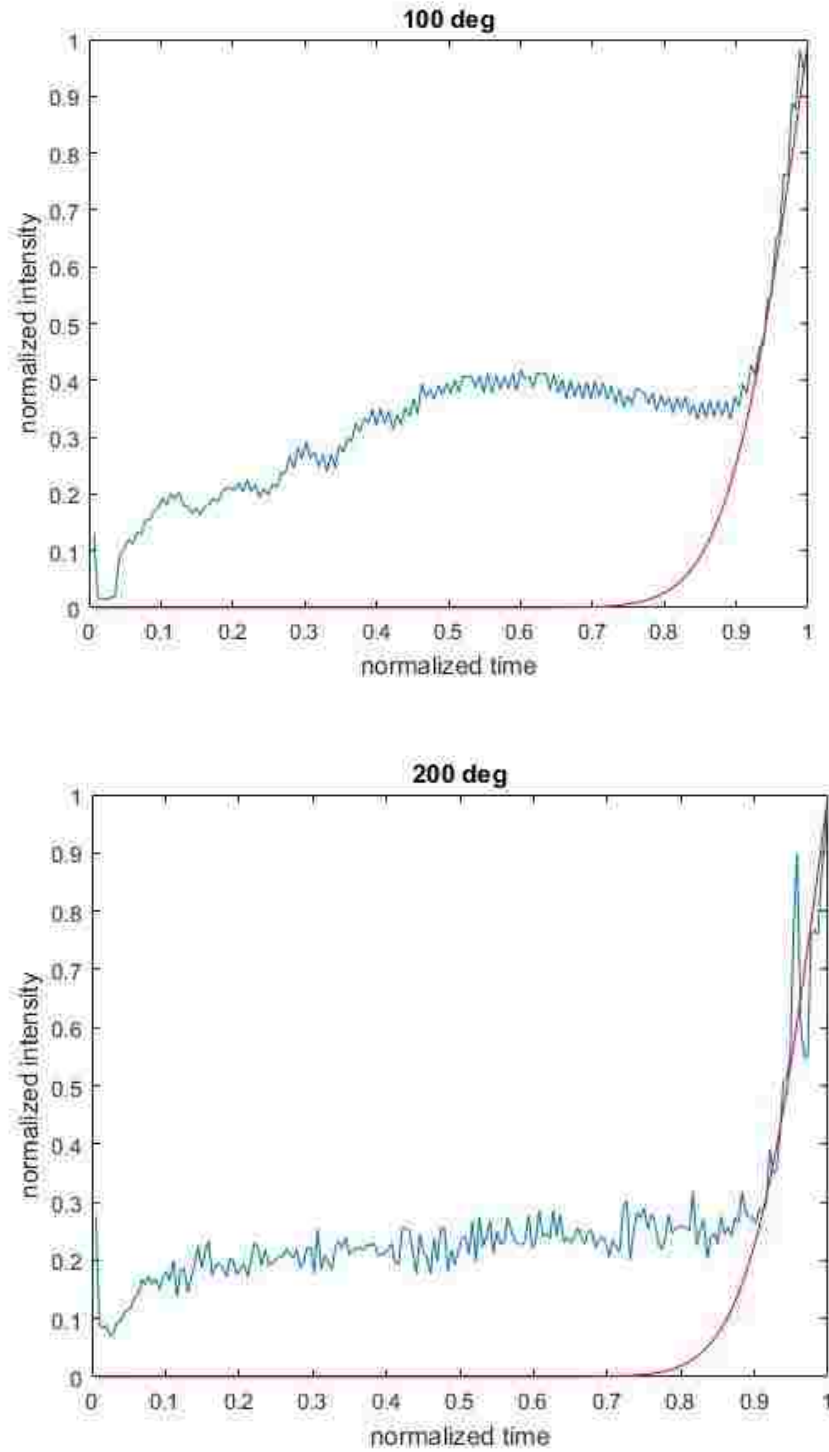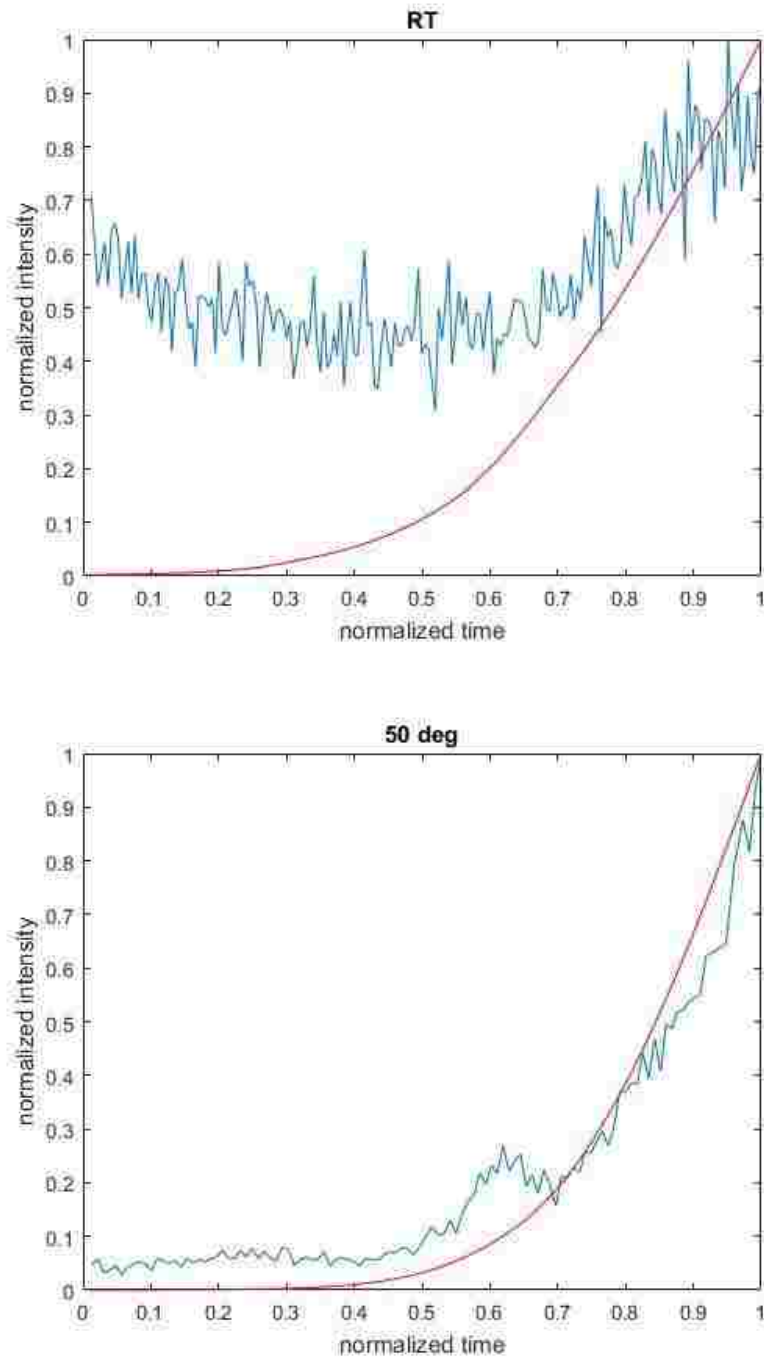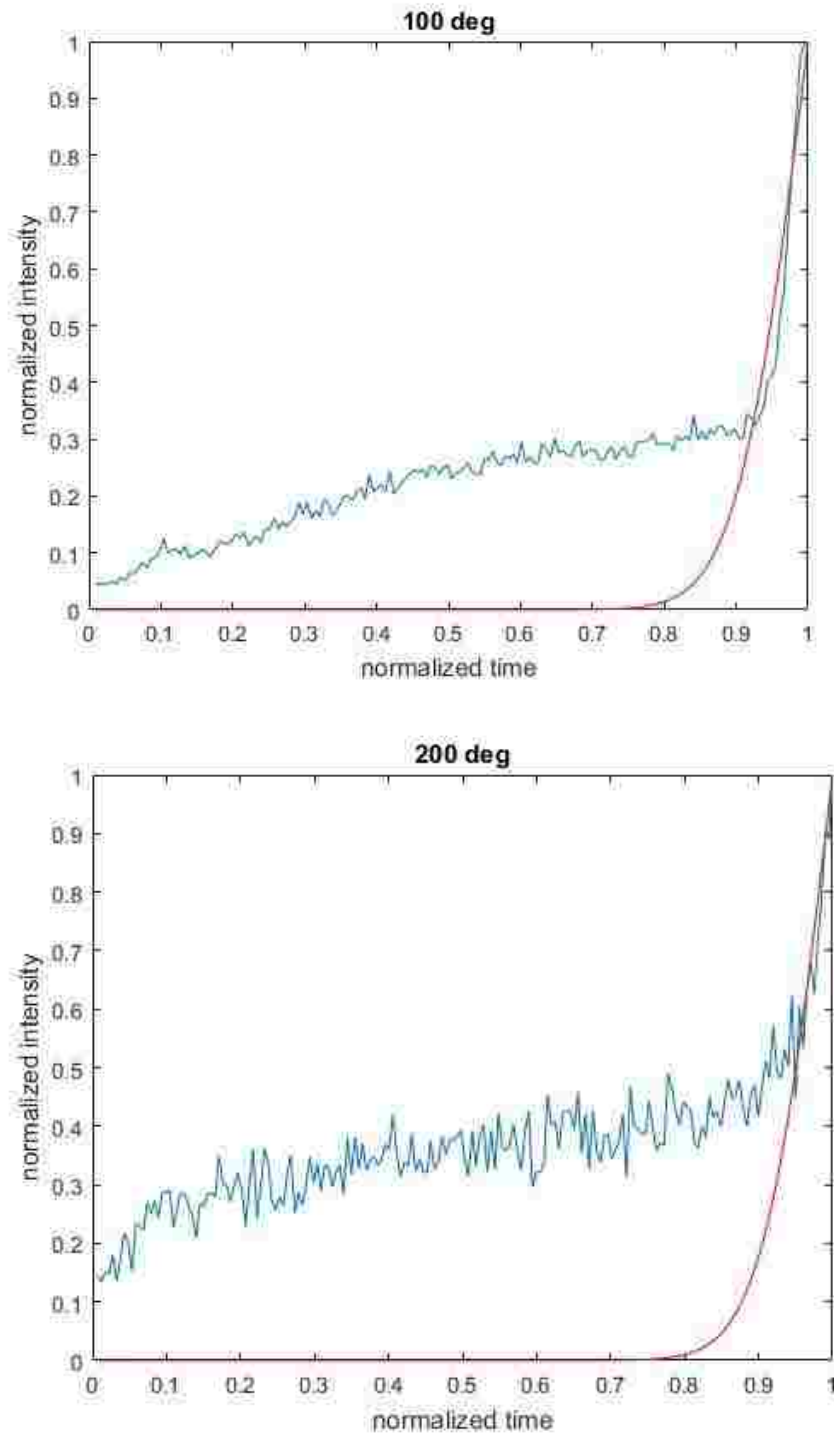
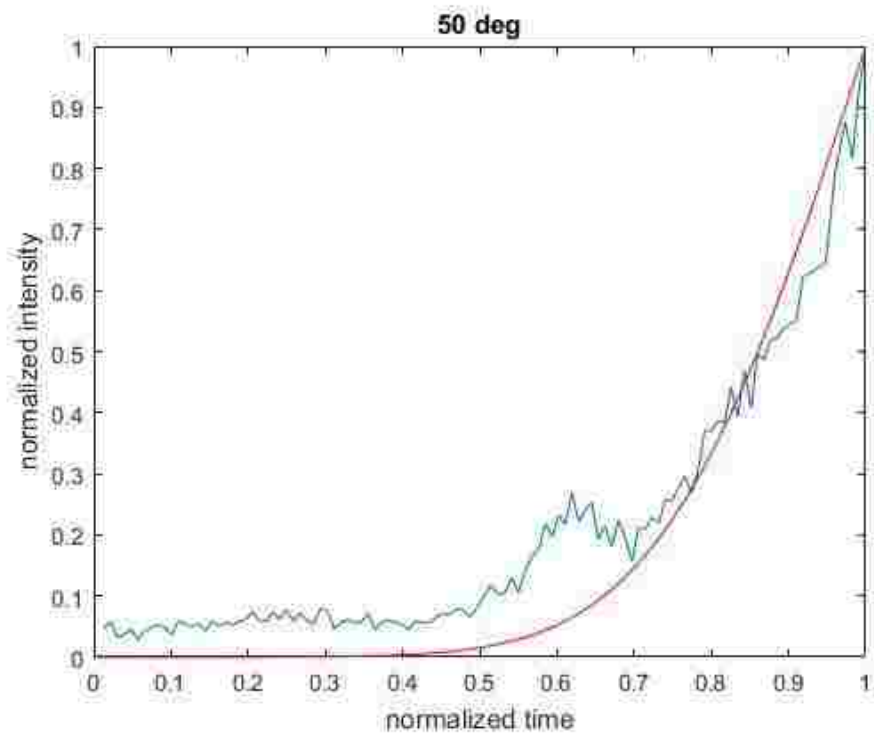Figure 4.17 Comparison of the experimental SIMS profile (blue line) and COMSOL TEM approximation model (red line) for potassium
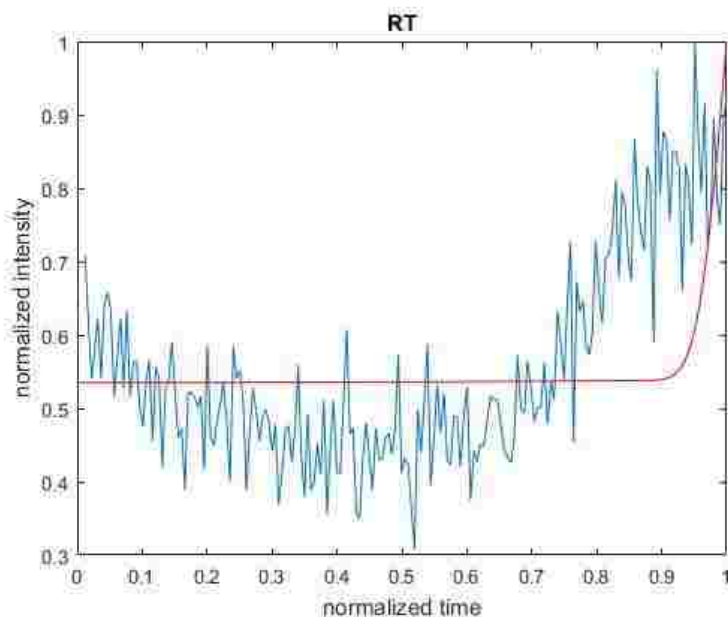
We could not obtain a good fit for the 100 and 200°C data, which might be due to saturation of sodium at 100°C. We also could not obtain a fit for the RT data. The diffusivity values obtained for the grain and grain boundary are given in Table 4.6.

Tss (°C)	$D_{boundary}$ (cm²/s)	D_{grain} (cm²/s)
23	1.0e-14	3.0e-14
50	4.0e-14	7.0e-15
100	8.0e-15	8.0e-16
200	8.0e-15	8.0e-16

Table 4.6. Diffusivity coefficients of potassium into molybdenum as a function of Tss, extracted for COMSOL TEM approximation model.

4.2.3   SUMMARY

A more advanced modeling was used for the simulation of sodium and potassium diffusion through molybdenum using COMSOL. Three types of model were developed: wafer, polycrystalline and TEM. The only parameters fitted for simulation were the grain diffusivity and the grain boundary diffusivity. The values for both parameters show consistently a higher value for the grain boundary diffusivity, which is consistent with the physical model. However, the fit to the data was not appropriate for room temperature or high temperature in most cases. This indicates that a different mechanism of diffusion might occur between the grain and the grain boundary or that a saturation of impurity occurs at some interfaces, changing locally the maximum concentration to be used in the model.

CHAPTER 5

5   SUMMARY

5.1   SUMMARY

Renewable energies are critical for the world to reduce our dependence on fossil fuels and mitigate the effects of climate change. One of the potential sources of renewable energies is photovoltaic, which directly transforms photons into electrons. CIGS is a major technology in this realm and depends heavily, as does any other PV technology, on the capacity to achieve the highest efficiency possible to compete on the market. Alkaline elements, notably sodium and potassium, play a key role in this matter as they enhance the open circuit voltage and the fill factor of the CIGS solar cells. However, this effect exists only for very specific concentrations of sodium and potassium, and the control of their concentration is therefore crucial for high efficiency generation. Because alkali are generally provided by the glass and diffuse through the molybdenum, we decided to study the diffusion process of this specific mechanism with an emphasis on substrate temperature as the process parameter.

Two main types of mathematical tools were used: one based on Excel spreadsheets, where boundary conditions were assumed, and one based on COMSOL, where Fick's diffusion equation was solved in real time. For the Excel fit, we used a combination of constant surface concentration and constant total dopant models, as well as grain and grain boundaries structures. We obtained the best fit when we used separate parameters for four values: grain boundary initial concentration and diffusivity and grain initial concentration and diffusivity. For the COMSOL fit, we used three different structures: wafer, polycrystalline and a more complex one based on a TEM image. In all cases, we obtained values for the diffusivity that were physically logical, with consistently higher values for the grain boundaries but not a very good fit for the room temperature and high

temperature profiles. Two summary tables, one each for sodium and potassium, are shown below summarizing all results obtained using Excel and COMSOL. The summary table for sodium is presented in Table 5.1 below.

	D_{grain} (cm^2/s)	$D_{boundary}$ (cm^2/s)	C_{grain} (mol/m^3)	$C_{boundary}$ (mol/m^3)
Tss (^{0}C)	Excel CSC Wafer Model			
23	1.84e-14	-	10	-
50	1.37e-14	-	10	-
100	4.91e-14	-	10	-
200	5.98e-15	-	10	-
	Excel CTD Wafer Model			
23	6.89e-15	-	10	-
50	5.24e-15	-	10	-
100	1.77e-14	-	10	-
200	1.06e-15	-	10	-
	Excel CSC Polycrystalline Model			
23	1.44e-14	1.00e-10	147.15	8.80
50	1.17e-14	2.04e-12	66.46	3.06
100	1.00e-15	3.52e-13	80.54	63.08
200	1.00e-15	1.08e-12	81.34	30.03
	Excel CTD Polycrystalline Model			
23	5.51e-15	1.75e-13	102.17	11.36
50	1.00e-15	1.53e-14	5.74	5.62

100	1.00e-15	1.34e-13	77.22	47.49
200	1.00e-15	4.26e-13	155.18	45.56
Excel CTD (GB) + CSC (G) Model				
23	4.57e-15	1.25e-13	63.93	17.84
50	2.19e-15	1.52e-14	26.23	25.25
100	1.00e-15	1.22e-13	75.26	50.10
200	1.00e-15	3.24e-12	120.45	36.44
Excel CSC (GB) + CTD (G) Model				
23	1.45e-14	1.00e-10	141.42	8.12
50	2.18e-15	1.52e-14	13.25	12.76
100	1.00e-15	1.22e-13	116.01	77.23
200	1.00e-15	2.64e-13	120.87	40.93
COMSOL Wafer Model				
23	1.5e-14	-	100	
50	1.3e-14	-	100	
100	2.0e-15	-	100	
200	2.0e-15	-	100	
COMSOL Polycrystalline Model				
23	5.0e-13	1.0e-14	100	100
50	5.0e-14	4.0e-14	100	100
100	1.0e-14	8.0e-15	100	100
200	1.0e-14	5.0e-15	100	100
COMSOL TEM Approximation Model				

23	1.5e-13	8.0e-15	100	100
50	4.0e-14	7.0e-15	100	100
100	1.0e-14	1.0e-15	100	100
200	1.0e-14	1.0e-15	100	100

Table 5.1. Sodium summary table of all diffusion theoretical Excel and COMSOL models

The summary table for potassium is shown in Table 5.2 below.

	D_{grain} (cm^2/s)	$D_{boundary}$ (cm^2/s)	C_{grain} (mol/m^3)	$C_{boundary}$ (mol/m^3)
Tss (^{0}C)	Excel CSC Wafer Model			
23	2.35e-13	-	10	-
50	1.05e-14	-	10	-
100	1.05e-14	-	10	-
200	6.68e-14	-	10	-
	Excel CTD Wafer Model			
23	8.45e-14	-	10	-
50	3.63e-15	-	10	-
100	1.00e-15	-	10	-
200	2.56e-14	-	10	-
	Excel CSC Polycrystalline Model			
23	9.41e-15	1.00e-10	99.89	98.72
50	1.95e-15	3.73e-14	107.88	95.86
100	1.00e-15	2.53e-13	144.80	69.49

200	1.00e-15	5.58e-13	101.58	26.75
Excel CTD Polycrystalline Model				
23	4.38e-15	1.00e-10	84.71	80.35
50	1.00e-15	2.29e-14	22.74	12.34
100	1.00e-15	1.14e-13	65.93	23.99
200	1.00e-15	2.49e-13	145.02	93.52
Excel CTD (GB) + CSC (G) Model				
23	9.84e-15	1.00e-10	52.40	49.01
50	2.58e-15	2.66e-14	69.88	30.94
100	1.00e-15	9.85e-14	74.08	30.22
200	1.00e-15	2.16e-13	115.04	79.94
Excel CSC (GB) + CTD (G) Model				
23	4.23e-15	1.00e-10	68.89	68.96
50	1.00e-15	3.62e-14	69.97	64.49
100	1.00e-15	9.84e-14	196.95	80.39
200	1.00e-15	2.16e-13	93.81	65.19
COMSOL Wafer Model				
23	2.0e-13	-	100	
50	8.0e-15	-	100	
100	1.1e-15	-	100	
200	1.1e-15	-	100	
COMSOL Polycrystalline Model				
23	5.0e-10	9.5e-16	100	100

50	5.0e-13	1.0e-15	100	100
100	1.0e-14	2.0e-15	100	100
200	1.0e-14	2.0e-15	100	100
COMSOL TEM Approximation Model				
23	1.0e-14	3.0e-14	100	100
50	4.0e-14	7.0e-15	100	100
100	8.0e-15	8.0e-16	100	100
200	8.0e-15	8.0e-16	100	100

Table 5.2. Potassium summary table of all diffusion theoretical Excel and COMSOL models

5.2   FUTURE WORK

Through this work, we demonstrated that it was possible to use two types of mathematical tools to model the diffusion of alkali through the molybdenum as a function of substrate temperatures. By treating the grain and the grain boundary independently, we could obtain excellent fit, and by using a direct solution to Fick's equations we were able to obtain physically meaningful data. However, we were not able to obtain both results at the same time. It is quite likely that a different issue is occurring as a function of temperature that we have not yet considered in our model. Because COMSOL is much more powerful than the simple Excel modeling, we would recommend continuing the simulation with that platform. The first step would be to use an independent concentration for the grain and grain boundary and verify that a very good fit could be obtained.

Next, a new model that considers potential chemical reaction occurring at a different temperature could be included. One leading suspect, because behaviors change at 100ºC is the

water/oxygen content into the layer. This would explain why values increase one way from room temperature to 100C and then another way once at higher temperature. Preliminary data obtained by XPS profile, seems to indicate a change in the oxygen concentration as a function of substrate temperature, which would correlate well with our hypothesis.

Finally, it is important to note that real time in-situ spectroscopic ellipsometry characterization was performed on the molybdenum samples by a PhD student in our research group. Ellipsometry is a non-destructive, non-invasive optical technique that measures the change in polarization of light as it interacts with the sample. It is a technique typically used to obtain film thickness and optical constants. 'In-situ' simply means that the characterization is performed as the film is being grown. Figure 5.1 shows the evolution of the surface roughness and the bulk layer thicknesses as a function of deposition time extracted from RTSE as for the moly film that is being grown at room temperature. From the results, we can see that there is a non-uniform molybdenum growth. Instead of the molybdenum film growing layer by layer, it first forms islands that then coalesce to form a bulk layer. Thus, the impurities diffuse very easily in and around the islands, but as soon as the islands come together and form a bulk layer, it becomes difficult for these impurities to diffuse, and they are subsequently forced to diffuse through the grain boundaries. This might explain why we needed two initial concentration values to obtain a good fit for all deposition temperature data because the non-uniform evolving growth of the molybdenum film might be causing the formation of different concentration profiles within the film.
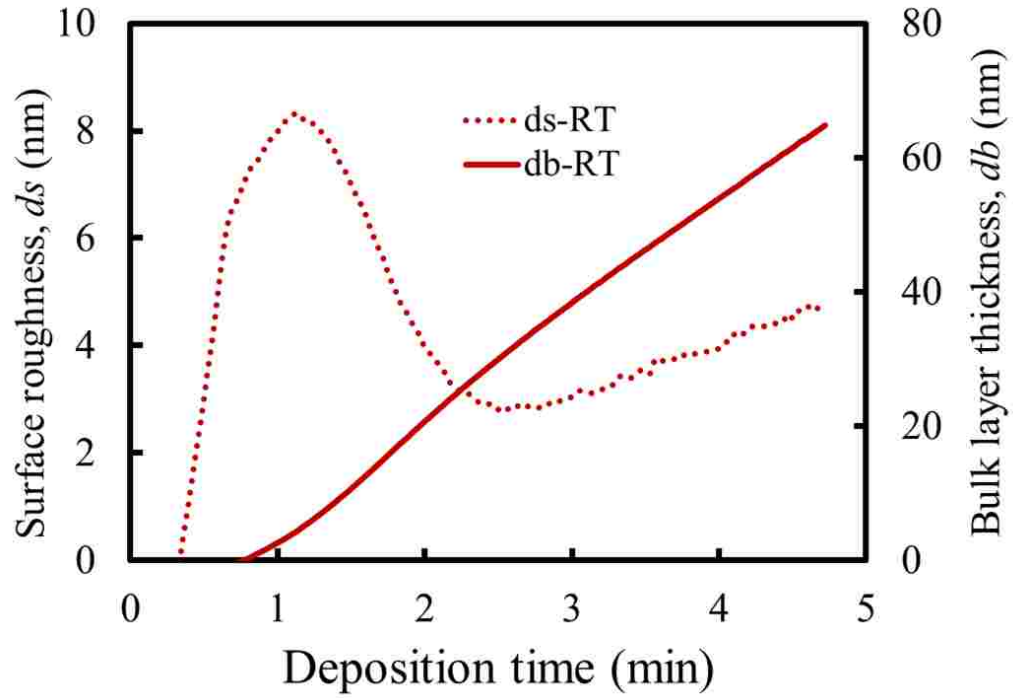
Figure 5.1 Real-time in situ SE measurements the Mo films deposited by DC magnetron sputtering at different substrate temperature

BIBLIOGRAPHY

[1]   A. Hu *et al.*, "Impact of solar panels on global climate," *Nature Climate Change,* vol. 6, no. 3, pp. 290-294, 2016.

[2]   C. A. Wolden *et al.*, "Photovoltaic manufacturing: Present status, future prospects, and research needs," *Journal of Vacuum Science & Technology A: Vacuum, Surfaces, and Films,* vol. 29, no. 3, p. 030801, 2011.

[3]   M. Grätzel, "Photovoltaic and photoelectrochemical conversion of solar energy," *Philosophical Transactions of the Royal Society of London A: Mathematical, Physical and Engineering Sciences,* vol. 365, no. 1853, pp. 993-1005, 2007.

[4]   J. Perlin, *From space to earth: the story of solar electricity*. Earthscan, 1999.

[5]   J. Ramanujam and U. P. Singh, "Copper indium gallium selenide based solar cells–a review," *Energy & Environmental Science,* 2017.

[6]   A. Laemmle, R. Wuerz, and M. Powalla, "Investigation of the effect of potassium on Cu (In, Ga) Se 2 layers and solar cells," *Thin Solid Films,* vol. 582, pp. 27-30, 2015.

[7]   D. Rudmann, G. Bilger, M. Kaelin, F.-J. Haug, H. Zogg, and A. Tiwari, "Effects of NaF coevaporation on structural properties of Cu (In, Ga) Se 2 thin films," *Thin Solid Films,* vol. 431, pp. 37-40, 2003.

[8]   J. M. Raguse, C. P. Muzzillo, J. R. Sites, and L. Mansfield, "Effects of sodium and potassium on the photovoltaic performance of CIGS solar cells," *IEEE Journal of Photovoltaics,* vol. 7, no. 1, pp. 303-306, 2017.

[9]   S. M. Sze, *Semiconductor devices: physics and technology*. John Wiley & Sons, 2008.

[10] http://cdn.comsol.com/documentation/5.2.0.220/IntroductionToCOMSOLMultiphysics.pdf.

VITA

Chinedum Akwari

231 Kaufman Hall
ECE Department
Old Dominion University
Norfolk, VA 23529

Education

| 2017 | **M.S.** | Electrical & Computer Engineering | Old Dominion University, VA |
| 2016 | **B.S**. | Electrical Engineering | Old Dominion University, VA |